Recent Progress in Understanding the Role of Monopoles in QCD

A Dissertation presented

by

Adith Ramamurti

to

The Graduate School

in Partial Fulfillment of the

Requirements

for the Degree of

Doctor of Philosophy

in

Physics

Stony Brook University

December 2018

Stony Brook University

The Graduate School

Adith Ramamurti

We, the dissertation committee for the above candidate for the

Doctor of Philosophy degree, hereby recommend

acceptance of this dissertation

Edward Shuryak - Dissertation Advisor
Distinguished Professor, Department of Physics & Astronomy

Derek Teaney - Chairperson of Defense
Associate Professor, Department of Physics & Astronomy

Matthew Dawber
Associate Professor, Department of Physics & Astronomy

Jinfeng Liao
Associate Professor, Department of Physics, Indiana University

This dissertation is accepted by the Graduate School

Dean of the Graduate School

Abstract of the Dissertation

Recent Progress in Understanding the Role of Monopoles in QCD

by

Adith Ramamurti

Doctor of Philosophy

in

Physics

Stony Brook University

2018

Chromo-magnetic monopoles are suggested to play an important role in quantum chromodynamics (QCD) near the deconfinement temperature. Previous studies have shown that monopoles can explain particular properties of quark gluon plasma and certain phenomena observed in heavy-ion collisions. In this dissertation, we discuss recent studies of QCD monopoles, with emphasis on explaining results from lattice QCD studies and heavy-ion experiments.

We begin by first tackling the question of whether monopoles exist in QCD. For theories with extended supersymmetry, the semiclassical partition functions of instanton-dyons were shown to be identical to the partition function for monopoles. We now show how the instanton-based partition function for a pure gauge theory can be Poisson-transformed into a partition function interpreted as that of moving and rotating monopoles. We then focus on reproducing the properties of quantum monopole ensembles through numerical simulations of path integrals. By matching observables of the simulated ensemble with those of monopoles found in lattice simulations, we define an effective quantum model of these objects.

The first application of the quantum model is in isolating the contribution of monopoles to the QCD equation of state. We find that the monopoles are responsible for a large proportion of the energy density of QCD near the deconfinement temperature. Next, by including the monopole contribution in the Baier-Dokshitzer-Mueller-Peigne-Schiff (BDMPS) jet energy loss model, we are able to reproduce the trends found in experimental observables for 2.76 TeV Pb-Pb collisions and 200 GeV Au-Au collisions, and make predictions for lower-energy collisions. Lastly, we use the ensembles from the path-integral simulations to investigate chiral symmetry breaking. Using fermionic zero modes of the Georgi-Glashow form, we study the spectrum of the Dirac operator and find that, in this model, a chiral condensate appears precisely at the critical temperature.

Contents

List of Figures

List of Tables

Acknowledgements

I have many people to thank for helping me through the years here at Stony Brook, providing both guidance and joy. I must first thank my advisor, Edward Shuryak, without whom this dissertation could not have been completed. His intuition and ability to pull together ideas from seemingly disparate areas of study is stunning, and made our discussions of physics truly enjoyable.

My research benefited very much from discussions with others in the nuclear theory group, especially Derek Teaney, Ismail Zahed, Dmitri Kharzeev, and Jacobus Verbaarshot. The spirited discussions at lunch certainly broadened my understanding of nuclear physics, and also taught me to question everything and anything. I thank our former post-docs Ioannis Iatrakis, for the many hours of help when I was beginning my research, and Jean-François Paquet, for his guidance in tackling problems in and out of physics. I am grateful for Sara Lutterbie, Don Sheehan, Socoro Delquaglio, and Marlene Vera-Viteri for making all administrative issues a breeze.

I also want to thank my officemates, Aleksas Mazeliauskas, Rasmus Larsen, Mark Mace, and Moshe Kellerstein, for the lively discussions we had each day.

It would be impossible to complete a Ph.D. without friends and family. I particularly want to thank my parents Ravi and Sita, and my brother Pradip, whose endless support gave me the foundation to get this far, in not only academics, but life. The ever-rotating NoCo crew always kept life away from work interesting, to say the least, and I couldn't have gotten through any of this without all of you.

Finally, and most importantly, I would not have made it through this process without the love and support from my partner and best friend Ashley Cohen.

The author thanks the Institute for Advanced Computational Science (IACS) at Stony Brook University for the use of its LI-red computational cluster. The research presented herein was supported in part by the U.S. D.O.E. Office of Science, under Contract No. DE-FG-88ER40388.

Publications

This dissertation is based on and reproduces text and figures from the following publications, to which the author of this work contributed significantly. All rights for the publishers and co-authors are reserved.

1. A. Ramamurti, E. Shuryak, and I. Zahed (2018). Are there monopoles in the quark-gluon plasma? Phys. Rev. **D97**(11), 114028. doi:10.1103/PhysRevD.97.114028 arXiv:1802.10509.

2. A. Ramamurti and E. Shuryak (2017). Effective Model of QCD Magnetic Monopoles From Numerical Study of One- and Two-Component Coulomb Quantum Bose Gases. Phys. Rev. **D95**(7), 076019. doi:10.1103/PhysRevD.95.076019 arXiv:1702.07723.

3. A. Ramamurti and E. Shuryak (2018). Role of QCD monopoles in jet quenching. Phys. Rev. **D97**(1), 016010. doi:10.1103/PhysRevD.97.016010 arXiv:1708.04254.

4. A. Ramamurti and E. Shuryak (2018). Chiral symmetry breaking and monopoles in gauge theories. Phys. Rev. **D**, under peer review. arXiv:1801.06922.

Chapter 1

Introduction

1.1 Topical Review

In this section, we will review the main phenomena found in systems that have spurred the interest in studying chromo-magnetic monopoles, and briefly overview previous research that this dissertation has built upon.

1.1.1 QCD and Heavy-Ion Collisions

The quantum field theory that describes the fundamental interactions between the constituents of nucleons – the quarks and the gluons – is quantum chromodynamics (QCD) [1]. QCD is a non-abelian gauge theory and possesses two important properties: asymptotic freedom [2–4] and color confinement [5–7].

The former, asymptotic freedom, tells us that at large momentum scales or small distances, the coupling of the theory becomes weak. High-momentum processes, which probe the small-distance limit of QCD, can therefore be described by a perturbative expansion in the coupling constant of the theory α_s. On the other hand, at small momenta or large distances, the strength of the strong interaction grows and non-perturbative phenomena appear, such as color confinement. Color confinement dictates that quarks and gluons (at our normal day-to-day energy scales) are found in *color neutral* configurations – baryons and mesons. The coupling constant for QCD as a function of the momentum scale is shown in Fig. 1.1.

The Lagrangian density of QCD is

$$\mathcal{L} = -\frac{1}{4}F_a^{\mu\nu}F^a_{\mu\nu} + \sum_f \bar{\psi}_i^{(f)}(i\not{D}^{ij} + m^{(f)}\delta^{ij})\psi_j^{(f)}\,, \tag{1.1}$$

where $\not{D} = \gamma_0 D$,

$$F^a_{\mu\nu} = \partial_\mu A^a_\nu - \partial_\nu A^a_\mu + g f^{abc} A^b_\mu A^c_\mu\,,$$
$$D^{ij}_\mu = \partial_\mu \delta^{ij} - ig(t^a)^{ij} A^a_\mu\,,$$

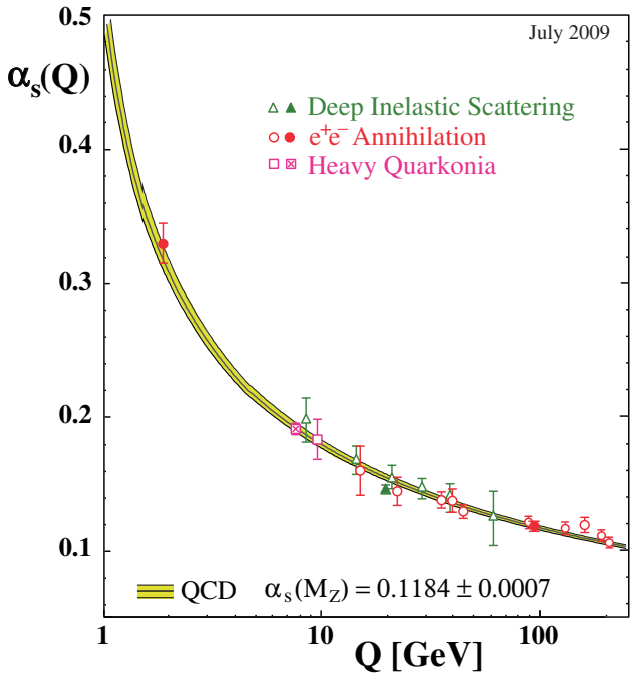

Figure 1.1: The strong coupling constant α_s as a function of the momentum scale. From Ref. [8].

and f^{abc} are the structure constants and τ^a the generators, respectively, of the SU(N_c) group for N_c colors. The coupling g is related to the strong coupling constant α_s by

$$\alpha_s = \frac{g^2}{4\pi}\,. \tag{1.2}$$

While the equations of motion of QCD are easily derived from its Lagrangian, finding solutions to these equations in regimes where perturbation theory breaks down, and subsequently deducing the physical consequences of these solutions remains an unsolved problem. One successful approach of studying strongly-interacting, nonperturbative QCD is known as lattice QCD, in which space-time is discretized [5]. With the progress of numerical methods and computational power, lattice QCD is able to reproduce and even predict some properties of the QCD, notably the observed hadron spectrum and the QCD equation of state. Another method of approaching non-perturbative physics is through use of semi-classical methods.

Phenomenology of a heavy-ion collision

To create matter where the degrees of freedom are quarks and gluons, known as a quark-gluon plasma (QGP) [9, 10], one has to reach energies and densities that overcome the binding forces of the nucleus [11–13]. In nature, such a state of matter is believed to have occurred in the moments following the Big Bang, and possibly in the core of neutron stars [14]. In the laboratory, however, the only way of creating such extreme conditions is through use of relativistic particle colliders [15]. In these machines, beams of nuclei possessing ultra-relativistic energies are collided, creating a droplet of deconfined nuclear matter, which then

thermalizes and undergoes a confinement process into a cloud of hadrons in a matter of femtoseconds. The debris of the collision are then processed by complex algorithms to reconstruct the evolution of the matter following the collision, from which we can probe the properties of that early-stage, hot droplet of matter, as well as try to understand its transition into the final-state particles that are observed in the detectors [16].

The standard theoretical model of a heavy-ion collision is broken into three stages: the initial state following the collision, bulk evolution of the dense matter, and hadronization. Understanding of the initial state, in its simplest form, comes from studying the geometry of the collision. In the rest frame of the nuclei, one can view each as a sphere with homogenous density. In the laboratory frame, due to Lorentz contraction, the nuclei, which are traveling at nearly the speed of light, are effectively projected onto a two-dimensional plane; the matter density now is variable, approaching zero at the edges.

When these two "pancakes" collide, the geometry of the collision can be described by the *impact parameter* $\vec{b}$, which connects the centers of the two nuclei. For a central collision, $\vec{b} = 0$, all (or most) constituents of the nuclei are considered *participants* in the collision, whereas in non-central collisions, $\vec{b} \neq 0$, some constituents pass by without interaction, known as *spectators*. A schematic of this type of collision is shown in Fig. 1.2. Only for the case $\vec{b} = 0$ is the collision azimuthally symmetric; in all other cases, the distribution of particles can be described by harmonics in the azimuthal angle, ϕ.

In this dissertation, we will be focusing on gold-gold (Au-Au) and lead-lead (Pb-Pb) collisions. Gold and lead nuclei are spherically symmetric, and therefore we do not need to consider their incoming orientation, as we would if we were looking at uranium-uranium collisions, for example. In experimental data, collisions are not classified directly by their impact parameter, but rather by their *centrality*, given as a percentile [18]. The centrality percentile c is defined from integrating the impact parameter distribution, $\frac{\mathrm{d}\sigma}{\mathrm{d}b}$,

$$c = \frac{1}{\sigma_{AA}} \int_0^b \frac{\mathrm{d}\sigma}{\mathrm{d}b'} \mathrm{d}b' \,. \tag{1.3}$$

For a model 2.76 TeV Pb-Pb collision, the relation between impact parameter and centrality percentile is shown in Fig. 1.3(a), while Fig. 1.3(b) shows the relation between centrality percentile and number of participants in the collision. In this dissertation, where relevant, we will focus primarily on 20-30% centrality collisions.

Nuclei, however, are not simply geometrically-defined, smooth objects. In fact, a nucleus consists mostly of empty space, as nuclear density is roughly 0.16 fm^{-3}. In addition, there is a non-zero probability that a nucleon passes through the other colliding nucleus without interaction. As a result, to have a better description of the initial state, one must include fluctuations on top of this smooth geometry that take these effects into account. Two models that do this and we will now discuss are the Glauber model and the Impact-Parameter GLASMA (IP-GLASMA) model.

The Glauber model is based on the principle that at the point of collision, the nucleons within the nuclei are a distributed set of points with probability dependent on the energy density. One defines two sets of parameters, ϵ_n, the amplitudes, and Φ_n, the phases of the

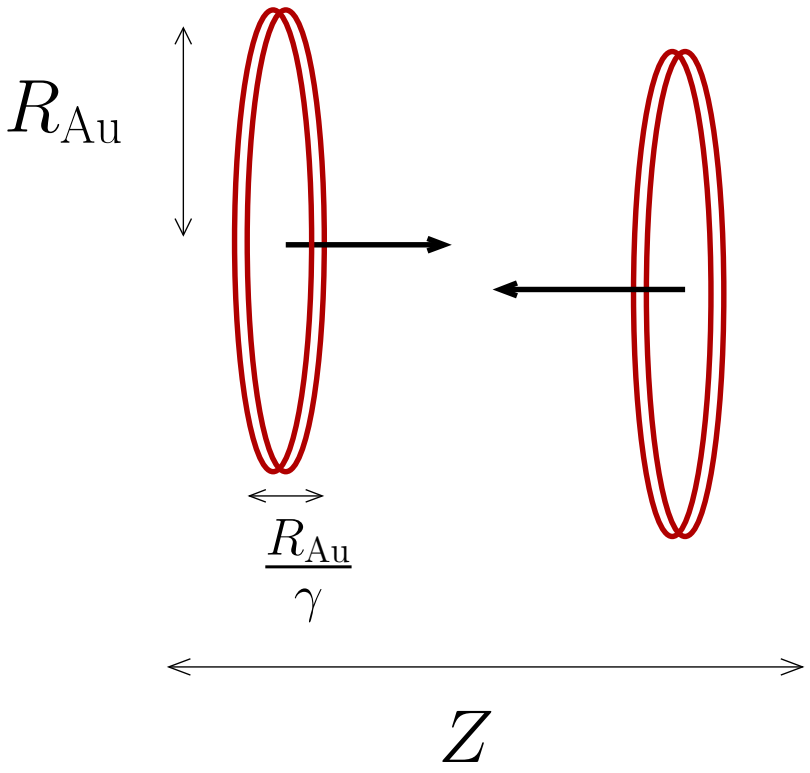

(a)

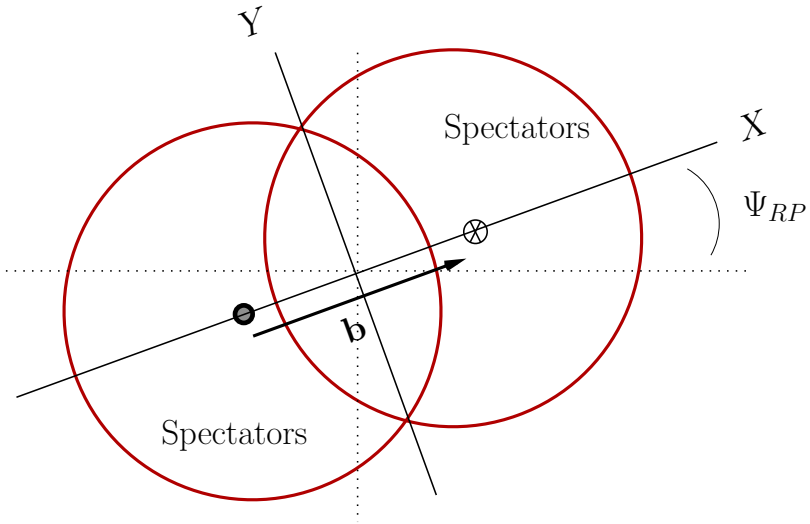

(b)

Figure 1.2: A schematic of a heavy-ion collision. (a) A "side" view of the collision, where nuclei are contracted along the beam direction. (b) A non-central collision has an elliptical overlap zone, with participant and spectator nucleons. From Ref. [17].

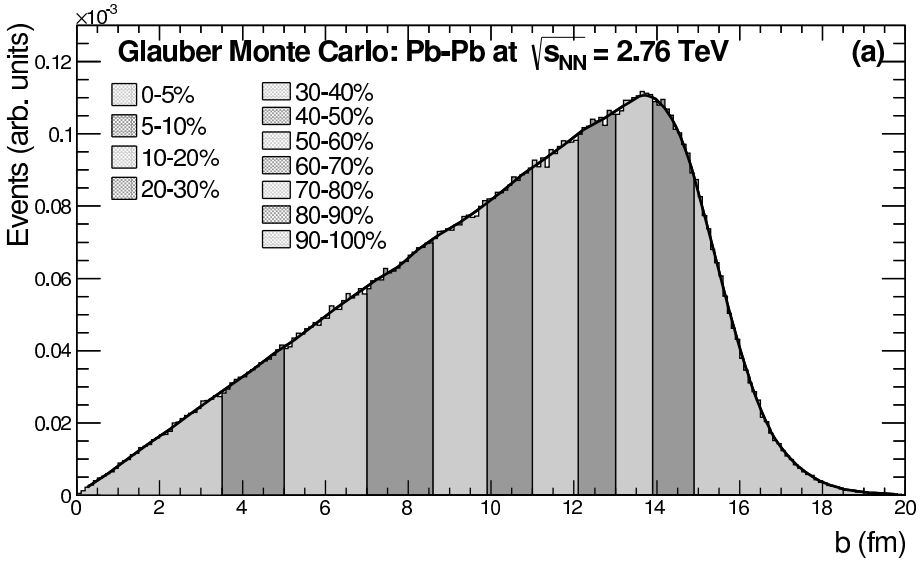

(a)

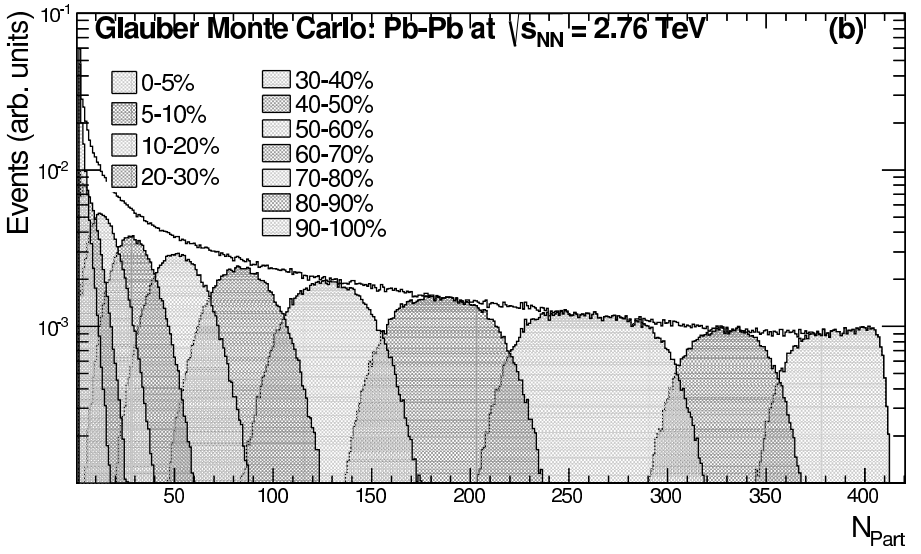

(b)

Figure 1.3: (a) The relation between impact parameter and centrality percentile, and (b) the relation between centrality percentile and number of participants in the collision. From Ref. [18].

initial state deformation, such that

$$\epsilon_n e^{in\Phi_n} = -\frac{\int \mathrm{d}r\mathrm{d}\phi r^{n+1} e^{in\phi} e(r,\phi)}{\int \mathrm{d}r\mathrm{d}\phi r^{n+1} e(r,\phi)}\,, \tag{1.4}$$

where $e(r,\phi)$ is the energy density distribution. Colliding nucleons are treated as spheres, and interact with each other if the separating transverse distance is less than $D = \sqrt{\sigma_{NN}/\pi} \sim 1.5$ fm, where σ_{NN} is the nucleon-nucleon cross section obtained from proton-proton collisions. See Ref. [19] for a thorough review of the Glauber model in nuclear collisions.

While this distribution of the initial state reproduces experimental observations well, we know that nucleons are not in fact point-like spherical particles. Nucleons have complex internal structure, made up of quarks and gluons. The GLASMA model [20–22] takes this complexity into account, describing the initial state as being comprised of randomly-distributed gluonic fields with size dependent on the saturation scale parameter, Q_s. The IP-GLASMA model [23] uses a location-dependent saturation scale, which is related to the gluon density N_g by

$$\frac{\mathrm{d}N_g}{\mathrm{d}^2\vec{x}} = Q_s^2(\vec{x})\,. \tag{1.5}$$

One may then sample the distribution on the lattice and produce an initial-state gluon configuration. Figure 1.4 shows the initial state of a heavy ion collision defined from both the Glauber model and the IP-GLASMA model. One can see that the IP-GLASMA model resolves a much finer structure of the nuclei.

Following the creation of the initial state, the matter undergoes bulk evolution. During early runs at the Relativistic Heavy Ion Collider (RHIC), it was found that there are significant momentum anisotropies in the final particle spectrum, characterized by harmonic coefficients v_n. These results, particularly the strong elliptic flow v_2 [24], suggested that there was collective behavior taking place during the evolution of the matter. Early phenomenological models based on hydrodynamics were remarkably successful in describing soft (low $p_\perp$) observables, and suggested that that the hydrodynamic "phase" lasted from $\sim .5$ fm to ~ 10 fm, dependent on the energy of the collision and size of the system.

Hydrodynamics is an effective, macroscopic theory derived from the conservation of energy and momentum,

$$D_\mu T^{\mu\nu} = 0\,, \tag{1.6}$$

where $T^{\mu\nu}$ is the stress-energy tensor and D_μ is the covariant derivative (in flat space, this is simply ∂_μ). Hydrodynamics utilizes the assumption that there are only four independent fields: the energy density, e, and the flow velocity, u^μ with time-like constraint $u^\mu u_\mu = -1$, which satisfy

$$T^{\mu\nu} u_\nu = -e u^\mu\,. \tag{1.7}$$

The stress energy tensor is then expanded in gradients of these fields,

$$T^{\mu\nu}(e,u^\mu) = T^{\mu\nu}_{(0)}(e,u^\mu) + T^{\mu\nu}_{(1)}(\partial e, \partial u^\mu) + ... \tag{1.8}$$

At zeroth order, known as ideal hydrodynamics, the stress-energy tensor is

$$T^{\mu\nu}_{(0)}(e,u^\mu) = e u^\mu u^\nu + p(g^{\mu\nu} + u^\mu u^\nu)\,. \tag{1.9}$$

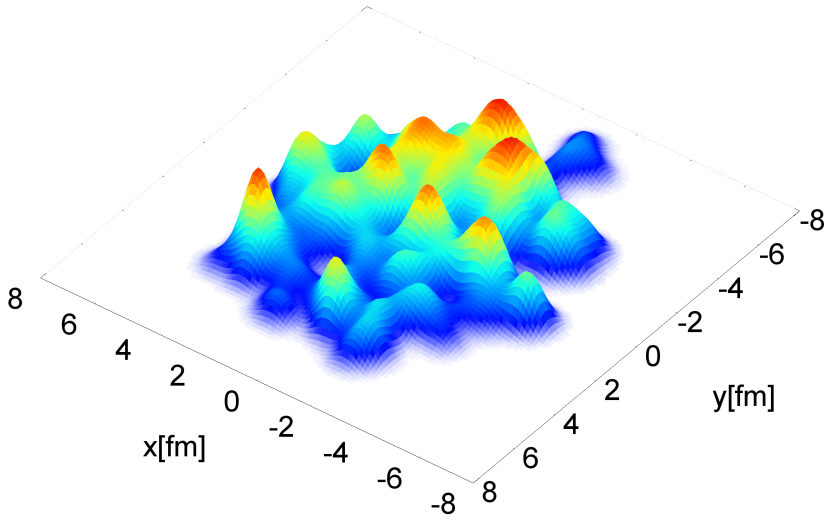

(a)

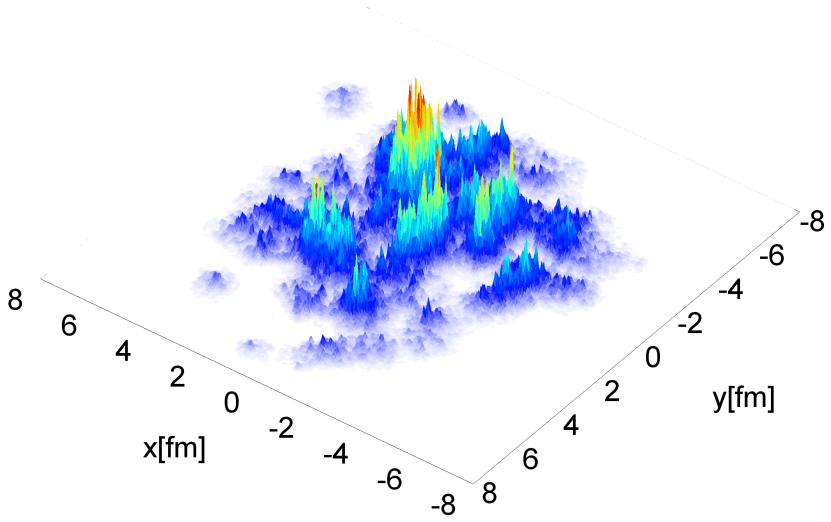

(b)

Figure 1.4: Initial conditions for a heavy-ion collision from the (a) Glauber model and (b) IP-GLASMA model. From Ref. [23].

For notational purposes, and to conform to literature, we will define $\Delta^{\mu\nu} \equiv g^{\mu\nu} + u^\mu u^\nu$. The ideal equations of motion are

$$u^\mu D_\mu e = -(e+p) D_\mu u^\mu \,, \tag{1.10}$$

$$u^\mu D_\mu u^\mu = -\frac{\Delta_\mu{}^\nu D_\nu p}{e+p} \,. \tag{1.11}$$

It was soon realized, though these ideal equations of motion could reproduce some experimental data, that it was necessary to include higher-order (viscous) terms in the hydrodynamic gradient expansion [25–27]. The first order correction, giving the classic Navier-Stokes equations of motion, is described by

$$T^{\mu\nu}_{(1)}(\partial e, \partial u^\mu) = \Pi \Delta^{\mu\nu} + \pi^{\mu\nu} \,, \tag{1.12}$$

where Π is a scalar, and $\pi^{\mu\nu}$ is a symmetric, traceless tensor satisfying $\pi^{\mu\nu} u_\mu = 0$. The resulting equations of motion and other intricacies are out of the scope of this work, but we must mention that the equations contain coefficients η, the shear viscosity, and ζ, the bulk viscosity. These transport coefficients are the subject of much work in recent years, both experimental and theoretical. The Navier-Stokes equations of motion are acausal [28], and therefore it is necessary to include higher-order terms [29, 30]. It is out of the scope of this dissertation to discuss this progress, see e.g. Ref. [17].

For hydrodynamics to accurately describe the dense QCD matter, we must have a good handle on the equation of state of QCD, particularly the relation between the pressure p and the energy density e. Simulations of QCD and QCD-like theories on the lattice have made considerable headway over the past decade. Recent equation of state calculations from Ref. [31], which we make comparisons to and use in our hydrodynamic simulations, are shown in Fig. 1.5. While these studies are limited by the sign problem to near-zero baryon chemical potential μ_B, the results are applicable to high-energy heavy-ion collisions, where the number of baryons is negligible in comparison to the total particle number.

Fig. 1.6 shows the evolution of a 2.76 TeV Pb-Pb collision, modeled with IP-GLASMA initial conditions coupled to (2+1)D viscous hydrodynamics.

After hydrodynamic evolution, the medium undergoes a *freeze-out* process, in which deconfined quarks and gluons transition into confined states, the hadronic degrees of freedom. This is described theoretically by production of particles with a distribution given by the Cooper-Frye formula at a given freeze-out surface Σ of constant temperature T_f, usually chosen to be close to the critical deconfinement temperature T_c,

$$E\frac{d^3N_s}{d^3p} = \frac{\nu_s}{(2\pi)^3}\int_\Sigma f_s(x^\mu, p^\mu) p^\nu d\Sigma_\nu \,, \tag{1.13}$$

where s denotes the particle species, ν a normalization constant, and f_s is the species' distribution function [32]. Kinetic evolution of hadrons then takes place until a *kinetic freeze-out*, when particles fly freely to the detectors.

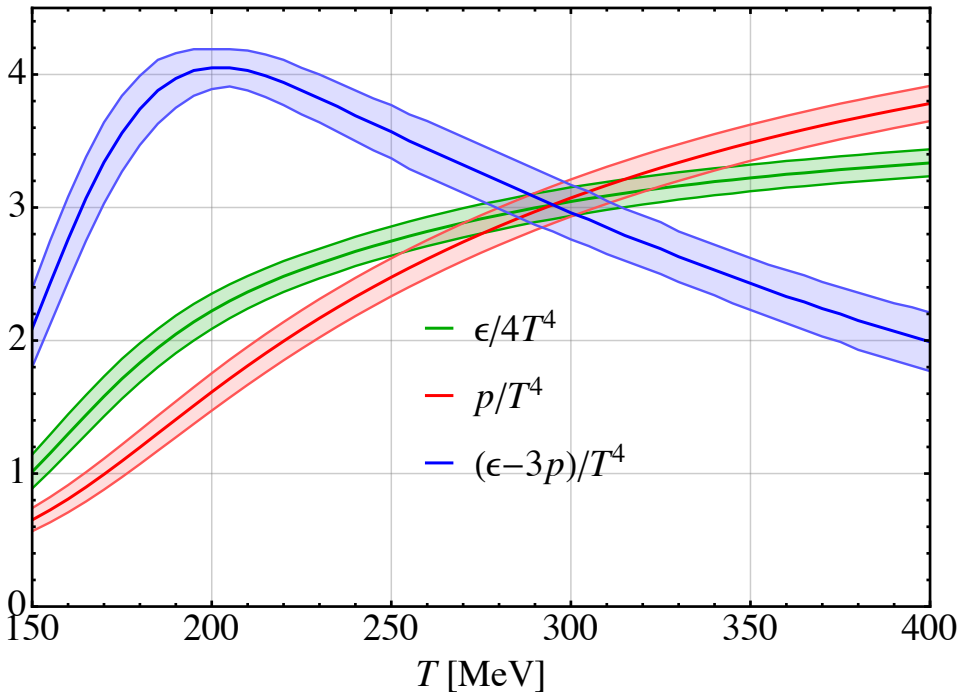

Figure 1.5: Equation of state of QCD found in (2+1) flavor lattice simulations. Figure adapted from Ref. [31]. The blue line is the trace anomaly, red is the pressure density, and the green is the (scaled by 1/4) energy density, all presented as unitless quantities.

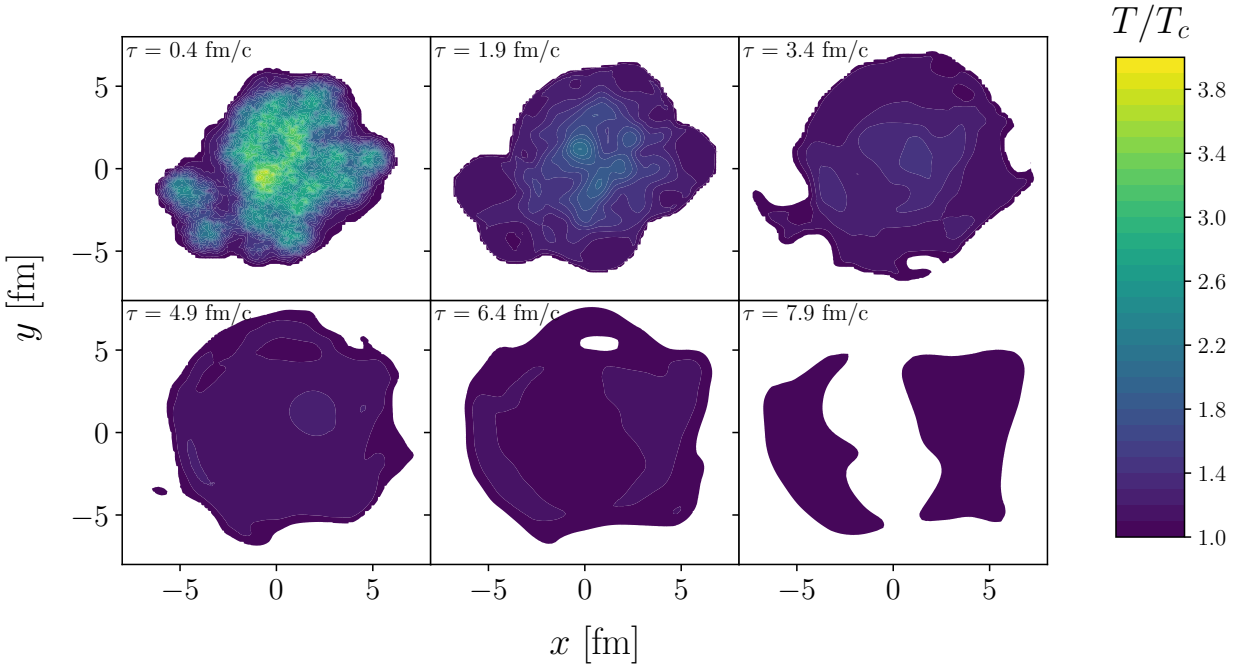

Figure 1.6: Temperature profile of a 20-30% centrality 2.76 TeV Pb-Pb collision, shown at various times of the hydrodynamic evolution. This evolution was done using IP-GLASMA initial conditions and (2+1)D hydrodynamics with bulk viscosity.

Jet quenching: Experimentally, theoretically, and the $R_{AA} \oplus v_2$ problem

To conclude this section on heavy-ion collisions, we will touch on one particular set of experimental observations from heavy-ion collisions that have motivated our studies. Recent experiments that have taken place at the Relativistic Heavy Ion Collider (RHIC) at Brookhaven National Laboratory and the Large Hadron Collider (LHC) at CERN have measured the distributions of high-energy particles, known as jets.

Jet energy loss is one of the classic signatures of QGP, proposed by Bjorken [33]. Perturbatively produced high-transverse-momentum partons subsequently traverse the QGP medium created in the heavy-ion collisions. These fast-moving partons interact with the medium and suffer collisional and radiative energy loss, leading to the phenomenon of "jet quenching."

There are three observables that will be studied in this dissertation. The first is the *nuclear modification factor*, denoted $R_{\mathrm{AA}}(p_\perp)$, describes the difference between the spectrum of hard partons that traverse a medium (particles produced in an ion-ion collision) and those that do not (particles produced in a proton-proton collision). Explicitly, the nuclear modification factor is

$$R_{\mathrm{AA}}(p_\perp, \phi) = \frac{\mathrm{d}N^{\mathrm{AA}}/\mathrm{d}p_\perp}{\langle N_{\mathrm{coll}}|N_{\mathrm{coll}}\rangle \, \mathrm{d}N^{\mathrm{pp}}/\mathrm{d}p_\perp}\,, \tag{1.14}$$

which is the ratio of particle spectrum from a heavy-ion collision ($\mathrm{d}N^{\mathrm{AA}}/\mathrm{d}p_\perp$) to a proton-proton collision ($\mathrm{d}N^{\mathrm{pp}}/\mathrm{d}p_\perp$), scaled by the number of nucleon collisions.

Its very strong deviation from one, to about 0.3 or so, was among the most dramatic RHIC discoveries. At the LHC, which produces about twice larger entropy and particle number than RHIC, the nuclear modification was expected to be further enhanced; this, however, has not happened.

Another important property of the in-medium jet energy loss is the azimuthal anisotropy, $v_2(p_\perp)$, the second Fourier component of the expansion of $R_{\rm AA}(p_\perp, \phi)$ in azimuthal angle ϕ,

$$\frac{\mathrm{d}N}{\mathrm{d}p_\perp \mathrm{d}\phi} = \frac{1}{2\pi}\frac{\mathrm{d}N}{\mathrm{d}p_\perp}\left(1 + 2\sum_n v_n \cos(n(\phi - \Psi_n))\right) . \tag{1.15}$$

Since the fireball produced in non-central collisions has an elliptical shape in the transverse plane – the lengths of medium in the direction of the impact parameter $\vec{b}$ and the orthogonal direction are different –, v_2 of jets characterizes the path-length dependence of the energy loss [34].

The last observable we consider is the dijet asymmetry, A_j. While in pp collisions, parton scattering leads to (back-to-back) dijets which are well-balanced in their transverse momenta, in the presence of matter this balance is lost, due to differences in the path length and matter fluctuations. Therefore, we can define a quantity to describe the imbalance,

$$A_j = \frac{|E_1 - E_2|}{E_1 + E_2} . \tag{1.16}$$

The history of and subsequently-produced list of literature on jet quenching is lengthy, and we do not attempt to summarize it; for recent discussion of these difficulties in modeling jet quenching and summaries of progress, see e.g., Refs. [35–39].

BDMPS jet quenching framework

In this dissertation, we will describe jets traversing the medium with the Baier-Dokshitzer-Mueller-Peigne-Schiff (BDMPS) formalism [40–44]. For the purposes of this work, we do not study other jet-quenching models, such as the Gyulassy-Levai-Vitev (GLV) [45–48] and Arnold-Moore-Yaffe (AMY) [49, 50] models, which include effects beyond gluon radiation and are built upon other theoretical underpinnings – hard-thermal loops (HTL) for AMY, for example. We now briefly review the results, and give expressions for the transport coefficients relevant to the studies we carry out.

The probability for a fast moving quark to have the transverse momentum $q_\perp$ at position z, $f(q_\perp^2, z)$ is given by,

$$\begin{aligned}\lambda(z)&\frac{\partial f(q_\perp^2, z)}{\partial z} \\ &= -f(q_\perp^2, z) + \int \frac{1}{\sigma}\frac{\mathrm{d}\sigma}{\mathrm{d}^2\vec{q}'_\perp}(\vec{q}'_\perp, z) f((\vec{q}_\perp - \vec{q}'_\perp)^2, z)\mathrm{d}^2\vec{q}'_\perp ,\end{aligned} \tag{1.17}$$

where $\lambda(z)$ is the mean free path of the jet particle and σ is the cross section. Taking the Fourier transforms of f,

$$\tilde{f}(b^2, z) = \int \mathrm{d}^2\vec{q}_\perp e^{-i\vec{b}\cdot\vec{q}_\perp} f(q_\perp^2, z) \tag{1.18}$$

and of the potential $V = \frac{1}{\sigma}\frac{\mathrm{d}\sigma}{\mathrm{d}^2\vec{q}_\perp}$,

$$\tilde{V}(b^2, z) = \int \mathrm{d}^2\vec{q}_\perp e^{-i\vec{b}\cdot\vec{q}_\perp} \frac{1}{\sigma}\frac{\mathrm{d}\sigma}{\mathrm{d}^2\vec{q}_\perp}(\vec{q}_\perp, z)\,, \tag{1.19}$$

we can diagonalize the master evolution equation by taking the Fourier transform of the RHS of Eq. 1.17,

$$\int \mathrm{d}^2\vec{q}'_\perp \int \mathrm{d}^2 b' e^{i(\vec{q}'_\perp - \vec{q}_\perp)\cdot\vec{b}'} \tilde{f}(b^2, z) \int \mathrm{d}^2 b \tilde{V}(b^2, z) e^{-i\vec{b}\cdot\vec{q}'_\perp}\,, \tag{1.20}$$

to get

$$\lambda(z)\frac{\partial \tilde{f}(b^2, z)}{\partial z} = [1 - \tilde{V}(b^2, z)]\tilde{f}(b^2, z)\,. \tag{1.21}$$

Taking as a model for the potential,

$$V(q_\perp^2) = \frac{1}{\sigma}\frac{\mathrm{d}\sigma}{\mathrm{d}^2\vec{q}_\perp}(\vec{q}_\perp) = \frac{\mu^2}{\pi(q_\perp^2 + \mu^2(z))^2}\,, \tag{1.22}$$

we find that, at small b, the evolution equation for the jet has the form,

$$\frac{\partial \tilde{f}(b^2, z)}{\partial z} = -\frac{b^2}{4}\hat{q}(z)\tilde{f}(b^2, z)\,, \tag{1.23}$$

The parameter $\hat{q}(z) \equiv \mu^2(z)/\lambda(z)$ is the main property of the matter – a kind of kinetic coefficient – that determines all features of the jet quenching. To get the explicit form for this, we take the Fourier transform of the potential,

$$\begin{aligned}\tilde{V}(b^2, z) &= \int \mathrm{d}^2\vec{q}_\perp e^{-i\vec{b}\cdot\vec{q}_\perp}\left(\frac{\mu^2(z)}{\pi}\right)\frac{1}{(q_\perp^2 + \mu^2(z))^2} \\ &= 2\mu^2(z)\left(\frac{1}{9}b^3\,{}_1F_2\left(2; \frac{5}{2}, \frac{5}{2}; \frac{b^2\mu(z)^2}{4}\right)\right. \\ &\quad \left. + \frac{\pi(I_0(b\mu(z)) - \mu(z)bI_1(b\mu(z)))}{4\mu^3(z)}\right)\,.\end{aligned} \tag{1.24}$$

Expanding around $b = 0$,

$$\tilde{V}(b^2, z) = \frac{\pi}{2\mu(z)} - \frac{1}{8}\pi\mu(z)b^2 + \mathcal{O}\left(b^3\right)\,, \tag{1.25}$$

Then,

$$\begin{aligned}&\frac{[1 - \tilde{V}(b^2, z)]}{\lambda(z)}\tilde{f}(b^2, z) \\ &\quad\approx \frac{\frac{1}{8}\left(\pi b^2\mu(z) - \frac{4\pi}{\mu(z)} + 8\right)}{\lambda(z)}\tilde{f}(b^2, z) \\ &\quad= -\frac{b^2}{4}\left(\frac{-\pi b^2\mu(z) + \frac{4\pi}{\mu(z)} - 8}{2b^2\lambda(z)}\right)\tilde{f}(b^2, z) \qquad (1.26) \\ &\quad= -\frac{b^2}{4}\hat{q}(z)\tilde{f}(b^2, z)\,, \qquad (1.27)\end{aligned}$$

where the transport coefficient $\hat{q}$,

$$\hat{q}(z) \equiv \frac{1}{\lambda(z)}\left[\frac{4}{b^2}(1-\tilde{V}(b^2,z))\right] = \frac{\langle \Delta p_\perp^2(z)|\Delta p_\perp^2(z)\rangle}{\lambda(z)}\,. \tag{1.28}$$

is defined to be the average squared transverse momentum acquired per unit length. This expression is not convergent at $b \to 0$ – see the expression in parentheses in Eq. (1.26) –, but in logarithmic approximation,

$$\begin{aligned}\hat{q}(z) &\approx \frac{1}{\lambda(z)}\int_0^{1/b^2} \mathrm{d}^2\vec{q}_\perp \vec{q}_\perp^{\,2} V(\vec{q}_\perp^{\,2}, z) \\ &= \rho(z)\int_0^{1/b^2} \mathrm{d}^2\vec{q}_\perp \vec{q}_\perp^{\,2}\frac{\mathrm{d}\sigma}{\mathrm{d}\vec{q}_\perp^{\,2}}(\vec{q}_\perp^{\,2}, z)\,,\end{aligned} \tag{1.29}$$

where $\rho(z)$ is the density of scatterers. This shows that this formalism is equivalent to the transport cross section method of finding the transverse kick; e.g. for a non-relativistic particle traveling in the z direction through the field of a single scatterer, we have that,

$$\Delta p_\perp = \int_{-\infty}^{\infty}\frac{b\,\mathrm{d}z}{(b^2+z^2)^{3/2}} = \frac{2}{b} \to \Delta p_\perp^2 = \frac{4}{b^2}\,. \tag{1.30}$$

The generic form of $\mathrm{d}\sigma/\mathrm{d}q_\perp^2$ in QCD is

$$\frac{\mathrm{d}\sigma}{\mathrm{d}q_\perp^2} = \frac{C}{(q_\perp^2+\mu^2)^2}\,, \tag{1.31}$$

The BDMPS-like energy loss of a parton as it traverses the medium is given by

$$-\,\mathrm{d}E/\mathrm{d}z \propto \hat{q}z\,. \tag{1.32}$$

The $R_{\mathbf{AA}} \oplus v_2$ "problem"

Most early models predicted v_2 to be approximately twice smaller than what was observed, even when the overall quenching rate was widely varied, and it was speculated that those models were missing some qualitative phenomenon [52]. Possible solutions include coupling the quenching of jets to the flow [38].

The solution which we consider in this dissertation is based on work by Liao and Shuryak [51], who suggested that the experimental v_2 can be replicated if the magnitude of jet quenching has a strong dependence on the matter temperature, with a near-T_c enhancement. Their general argument is purely geometric. If all jet quenching occurred at a particular shell of entropy (i.e. the R_AA was reproduced), the anisotropy of the final particle spectrum would be bounded by the shape of the shell. Breaking the medium created in a heavy-ion collision into its constituent entropy shells, one finds the distribution on the left of Fig. 1.7. One can see that the largest v_2 comes from the near-T_c region of the fireball, while the QGP portion produces a smaller effect. On the right of Fig. 1.7, the resulting v_2 from three different shells is compared to experimental data; a near-T_c shell gives approximately the correct order of magnitude of v_2.

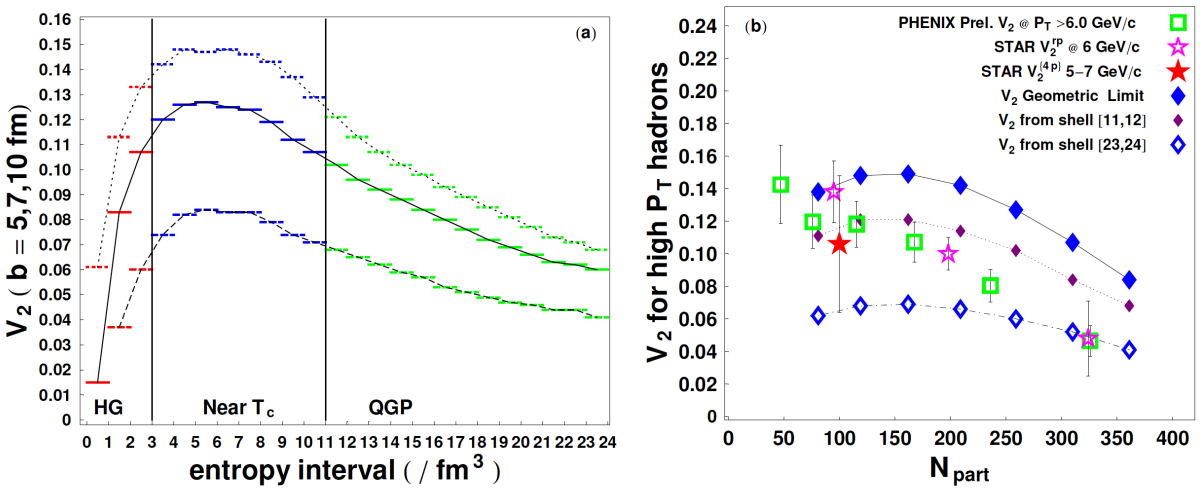

Figure 1.7: (left) Entropy shells of a the medium created in a heavy-ion collision along with their corresponding jet v_2, and (right) comparison to RHIC data. From Ref. [51].

1.1.2 Magnetic Monopoles in Field Theory

Following the observation by Liao and Shuryak, one's first instinct would be to look for some objects that are prominent near the deconfinement transition. This naturally leads to non-perturbative objects, such as magnetic monopoles. We will, in this section, review the development of the theory of magnetic monopoles in field theory. Before beginning this section, we would be remiss not to direct the reader to the book by Ya. M. Shnir [53], wherein there is a trove of knowledge on the theoretical developments, historical and modern, of magnetic monopoles.

Monopoles in electrodynamics

The possible existence of magnetic monopoles in electrodynamics fascinated leading physicists – J.J. Thompson, H. Poincaré, and especially P.A.M. Dirac – for more than a century. Dirac [54], in 1931, introduced into Maxwell's theory of electrodynamics a point particle with magnetic charge. In order to do so and maintain consistency with $\nabla \cdot \vec{B} = 0$, one must introduce to the vector potential a singular line, known as a Dirac string, which supplies magnetic flux from "outside" (i.e. infinity). The Dirac potential has the form,

$$A(r) = \frac{g}{r}\frac{\vec{r}\times\vec{n}}{r - (\vec{r}\cdot\vec{n})}\,, \tag{1.33}$$

which sources a magnetic field

$$B = g\frac{\vec{r}}{r^3}\,. \tag{1.34}$$

The ideas of Dirac enjoyed extensive investigation, but no magnetic monopole in electrodynamics was ever found.

One important idea derived from this solution was that of the *Dirac condition*. The Dirac string, which carries magnetic flux, acts as the solenoid in the Aharonov-Bohm effect [55]. A particle which completes a path around the string obtains a phase,

$$\phi = e \oint_C A \cdot ds = e \int B \cdot dS \,. \tag{1.35}$$

Substituting in the potential, one finds that the phase,

$$\phi = 4\pi e g \,. \tag{1.36}$$

For the Dirac string to remain invisible, the total phase must be a multiple of 2π, which therefore leads to the quantization condition,

$$eg = \frac{n}{2} \,. \tag{1.37}$$

Monopoles as a soliton solution to field theories

Before continuing the discussion of magnetic monopoles outside of the theory of electrodynamics, we must touch on the idea of a topological soliton. With the advent of non-Abelian gauge theories as candidates for a unification of the strong, weak, and electromagnetic interactions, the first step – before attempting to solve the full quantum theory – was to find and understand solutions to the classical equations of motion. Of particular interest were the solutions that are stable, non-dissipative, and of finite-energy, which are known as *solitons*.

A soliton, which can be found from the Euler-Lagrange equations derived from the Lagrangian of the theory, is stable if it minimizes the action, $\delta S \geq 0$. These stable solitons can be classified by the mechanism by which they "obtain" their stability: topological or non-topological. In this dissertation, we will focus on topological solitons; these maintain their stability through the fact that they possess a mapping from the internal field space to the real d-dimensional space of the theory, characterized by an integer, known as the *topological charge*. As a result, there is effectively an infinite potential barrier caused by the topology of the fields; these solitons with finite topological charge cannot simply diffuse into a vacuum with zero topological charge.

These solutions, derived from the classical equations of motion, *cannot* be found using standard perturbation theory, and are therefore fully-fledged non-perturbative objects. Upon the classical solutions of the equations of motion, one may introduce quantum fluctuations, from which we obtain a new class of quantum, non-perturbative solutions to a theory.

Of particular note to this dissertation, classical solitons with magnetic charge have been found, by 't Hooft [56] and Polyakov [57], in the 1970s. The Lagrangian considered, the Georgi-Glashow model, is

$$\mathcal{L} = -\frac{1}{4} F_a^{\mu\nu} F_{a\mu\nu} + \frac{1}{2} (D_\mu \phi)_a (D^\mu \phi)_a - \frac{1}{4} \lambda (\phi_a \phi_a - v^2) \tag{1.38}$$

where

$$F_a^{\mu\nu} = \partial^\mu A_a^\nu - \partial^\nu A_a^\mu + g \epsilon_{abc} A_b^\mu A_c^\nu \,,$$

and

$$(D^\mu\phi)_a = \partial^\mu\phi_a + g\epsilon_{abc}A^\mu_b\phi_c\,.$$

This Lagrangian has a scalar field, ϕ, which exists in the adjoint color representation. This scalar field is "Higgsed," with its vacuum expectation value (VEV) given by v.

The SU(2) 't Hooft-Polyakov monopole solution has the form

$$\begin{aligned} A^0_a &= 0\,, \\ A^i_a &= \epsilon^{aij}\hat{r}_j\frac{A(r)}{g}\,, \\ \phi_a &= \hat{r}_a\frac{\phi(r)}{g}\,. \end{aligned} \tag{1.39}$$

With this ansatz, the equations of motion from the pure-gauge Lagrangian are

$$\begin{aligned} 0 = \frac{2}{r^2}\frac{\mathrm{d}}{\mathrm{d}r}\left(r^2\frac{\mathrm{d}A}{\mathrm{d}r}\right) - \frac{2}{r}\frac{\mathrm{d}A}{\mathrm{d}r} + \frac{2}{r^2}\frac{\mathrm{d}}{\mathrm{d}r}(rA) \\ - \frac{6}{r^2}A - \frac{6g}{r}A^2 - 2g^2A^3 - \phi\left(\frac{2g}{r} + 2g^2A\right)\,, \end{aligned} \tag{1.40}$$

$$\begin{aligned} 0 = \frac{1}{r^2}\frac{\mathrm{d}}{\mathrm{d}r}\left(r^2\frac{\mathrm{d}\phi}{\mathrm{d}r}\right) - \frac{2}{r^2}\phi - \frac{4g}{r}A\phi \\ - 2g^2A^2\phi - 2U'(|\phi|^2)\phi\,, \end{aligned}$$

and boundary conditions,

$$\begin{aligned} \left(r^2\frac{\mathrm{d}A}{\mathrm{d}r} + 2rA\right)\Bigg|_{r=0} &= 0\,, \\ \left(r^2\frac{\mathrm{d}\phi}{\mathrm{d}r}\right)\Bigg|_{r=0} &= 0\,. \end{aligned} \tag{1.41}$$

This set of equations and boundary conditions, combined with single-valuedness of the fields at the origin give

$$\begin{aligned} A(0) = \phi(0) &= 0\,, \\ A(r)\Big|_{r\to\infty} &= -\frac{1}{r}\,, \\ \phi(r)\Big|_{r\to\infty} &= v\,. \end{aligned} \tag{1.42}$$

One may guess a solution that satisfies both the ansatz and the boundary conditions. An example of an asymptotic solution is the well-known "hedgehog" configuration,

$$\phi^a\Big|_{r\to\infty} = v\frac{r^a}{r}\,, \tag{1.43}$$

from which the "needles" of the field are radial in color space. The magnetic current for the field configuration is given by

$$k^\mu = \epsilon^{\mu\nu\rho\sigma}\epsilon_{abc}\partial_\nu\phi^a\partial_\rho\phi^b\partial_\sigma\phi^c\left(\frac{1}{2v^2g}\right). \tag{1.44}$$

Evaluating the magnetic charge for the asymptotic solution gives

$$g_m = \int \mathrm{d}^3x k_0 = \frac{4\pi}{g}. \tag{1.45}$$

This solution looks like a Dirac monopole at large distances. To put this in a nicer form, one similar to the Dirac condition, we can write this in terms of the square of charges,

$$g_m^2 = \frac{(4\pi)^2}{g^2} \to \frac{g_m^2}{4\pi}\frac{g^2}{4\pi} = 1, \tag{1.46}$$

from which we can define the fine structure constants, $\alpha_e \equiv g^2/4\pi$ and $\alpha_m \equiv g_m^2/4\pi$, with $\alpha_e\alpha_m = 1$.

The full solutions to the equations of motion for $A(r)$ and $\phi(r)$ are well behaved at the origin, so in practice we must use those in lieu of only considering asymptotics. We can write these full solutions in terms of two spherically-symmetric functions, H and K. In terms of these functions, our gauge fields are,

$$\begin{aligned} A_a^0 &= 0, \\ A_a^i &= \epsilon^{aij}\frac{r_j}{gr^2}(1-K(\xi)), \\ \phi_a &= \frac{r_a}{gr^2}H(\xi), \end{aligned} \tag{1.47}$$

where $\xi = gvr$. This leads to the identification with our earlier notation,

$$\begin{aligned} A(r) &= \frac{1-K(gvr)}{r}, \\ \phi(r) &= \frac{H(gvr)}{r}. \end{aligned} \tag{1.48}$$

The only analytic solution to the equations of motion is in the case where $\lambda = 0$; this solution is known as the Bogomolnyi-Prasad-Sommerfeld (BPS) monopole [58, 59]. In this case,

$$\begin{aligned} H(\xi) &= \xi\coth(\xi) - 1, \\ K(\xi) &= \frac{\xi}{\sinh(\xi)}. \end{aligned} \tag{1.49}$$

All other solutions are only obtained numerically. Figure 1.8 shows the BPS solution ($\lambda = 0$) and the numerical solution for $\lambda = 0.1$, 1.

The extension of the SU(2) 't Hooft-Polyakov monopole solution to SU(3) – with the same Georgi-Glashow-like Lagrangian – is discussed by A. Sinha [60]. In this case, there are *two* diagonal generators, which lead to two types of monopoles. We will only study the SU(2) case in this dissertation, and make qualitative arguments on extending to a larger color group.

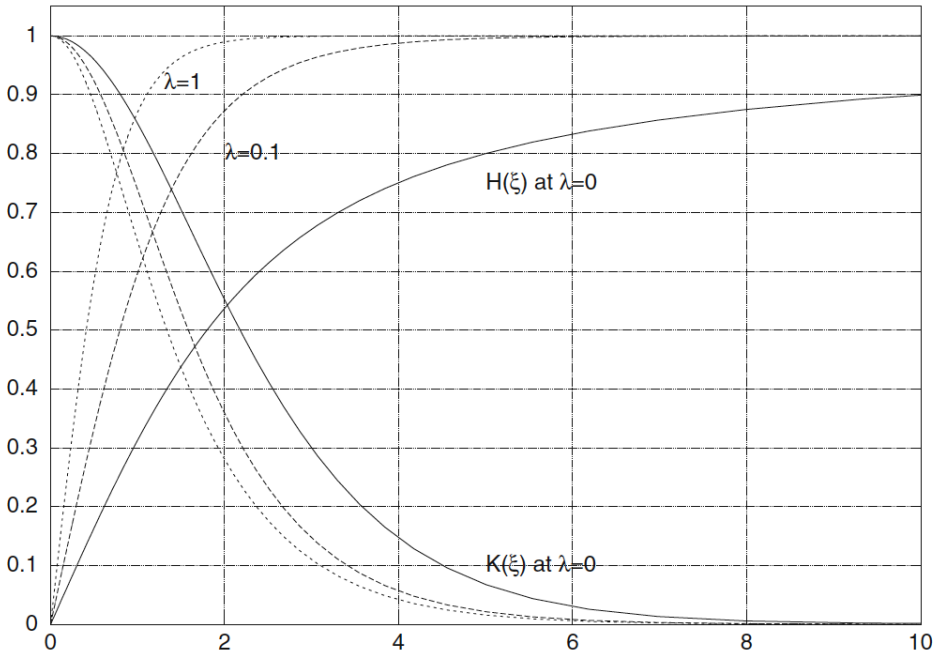

Figure 1.8: Solutions for the 't Hooft-Polyakov monopole for various values of the parameter λ. From Ref. [53].

The magnetic scenario of QCD

These solutions motivated the *dual superconductor* model of the confinement, proposed by Nambu [61], 't Hooft [62], and Mandelstam [6]. In this scenario, one considers the dual to the standard Landau-Ginzburg model for a superconductor, and monopoles play the role of Cooper pairs. Their Bose-Einstein condensation (BEC) at $T < T_c$ expels electric field from the vacuum into confining flux tubes. We will give a more rigorous definition of BEC, in a form relevant to this dissertation, in the section on path integrals. For a thorough review of this model, see Ref. [63].

A justification of this scenario has been obtained by the lattice gauge theory community. Importantly, researchers were able to identify the gauge field monopoles and even follow their correlations and motion [64, 65]. The density of monopoles found in SU(2) and SU(3) gauge theories is shown in Fig. 1.9. In the SU(3) case, as one would assume from studying monopole solutions to the SU(3) Georgi-Glashow model [60], there are *two* types of monopoles. We see that, in both cases, the (unitless) monopole density *peaks* at T_c, oppositely to the quarks and gluons; the latter is due to the Polyakov line going to zero as $T \to T_c$, as argued in Ref. [66].

Radial correlations are shown in Fig. 1.10. We define the pair correlation $g(r)$ to satisfy

$$n(r) = 4\pi\rho \int_0^r g(r')r'^2 dr' \,, \tag{1.50}$$

where $n(r)$ is the number of particles found between 0 and r, and $\rho = N/V$ is the overall density of particles in the volume; $g(r)$ is, by definition, normalized to distribution of an

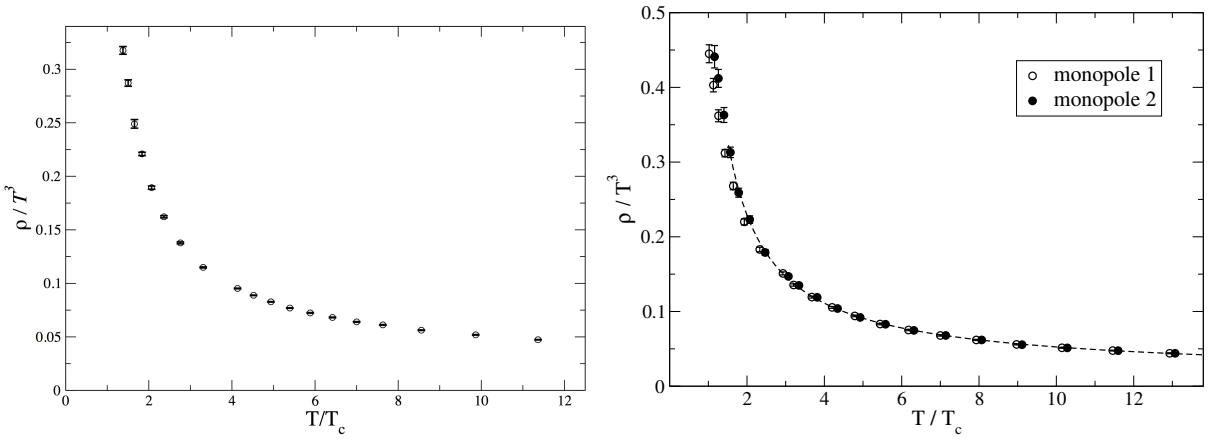

(a) (b)

Figure 1.9: Monopole density found in pure-gauge SU(2) [64] and SU(3) [65] lattice simulations.

ideal gas. General arguments based on the renormalization group flow tell us that, moving from hard (UV) to soft (IR) momenta, one should see growth of electric coupling and, due to the Dirac condition ($g_m g_e = 2\pi n$, for some integer n assumed to be 1), the *decrease* of the magnetic. We see this through the decrease in the deviation from 1 for the monopole-anti-monopole as $T \to T_c$ from above. In addition, we note that the shape of the radial distributions indicate that the monopoles form a two-component Coulomb gas.

In a regime where both couplings are comparable one should expect a comparable density of electric and magnetic quasiparticles. It has been argued that such regime occurs *above* the phase transition, at $T = (1-2)T_c$. This *magnetic scenario* was further used for explaining unusual properties of QGP by Liao and Shuryak [67–69]. In this scenario, the uncondensed magnetic monopoles play a dominant role near the QCD critical temperature, T_c, where their density peaks. Scattering between electric and magnetic quasiparticles dominate the transport cross section [70].

The phase diagram of such a scenario is shown in Fig. 1.11. The blue-shaded region is the region of confinement, called *m-dominated* because the color-electric field is expelled into flux tubes. Classical molecular-dynamics simulations of a Coulomb electromagnetic plasma were carried out to reproduce the correlations seen on the lattice; the results are shown in Fig. 1.12. We see that the coupling of the plasma (Fig. 1.12(b)) runs exactly as expected by the Dirac condition.

1.1.3 Path-Integrals and Many-Body Simulations

In order to study the proposed properties of magnetic monopoles stated in the previous section, one must be able to study, quantum mechanically, ensembles of monopoles. We do this, as is done in lattice gauge theory simulations, by studying the path-integral of the system.

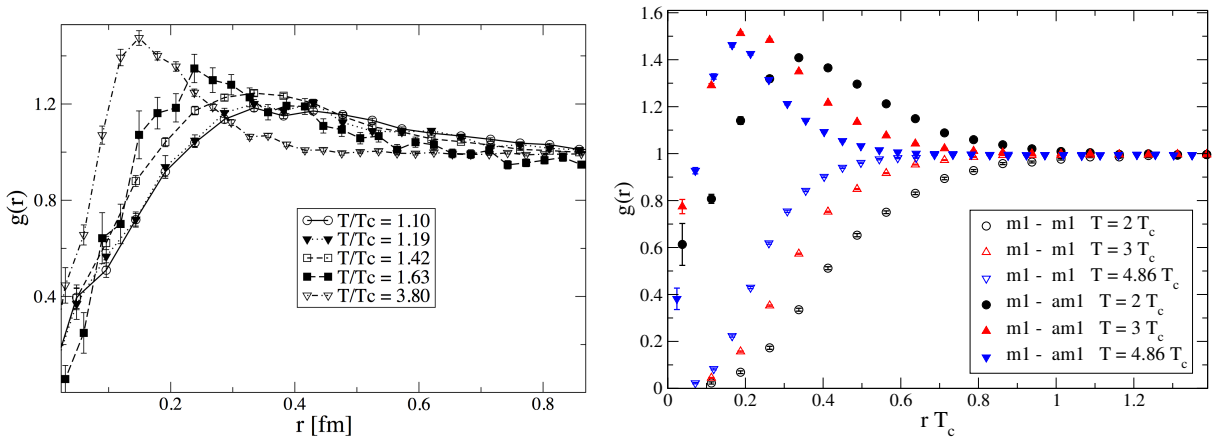

(a) (b)

Figure 1.10: Monopole (antimonopole) radial correlations found in pure-gauge SU(2) [64] and SU(3) [65] lattice simulations.

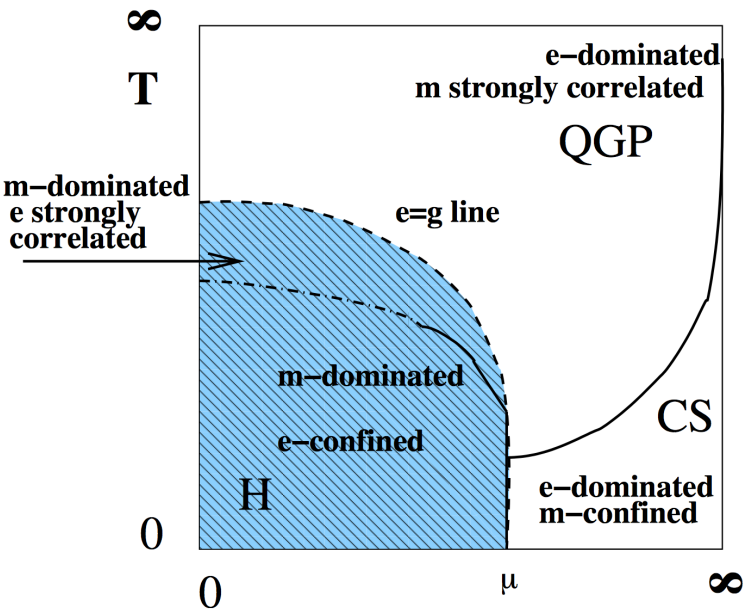

Figure 1.11: The phase-diagram of the magnetic scenario of QCD. From Ref. [67].

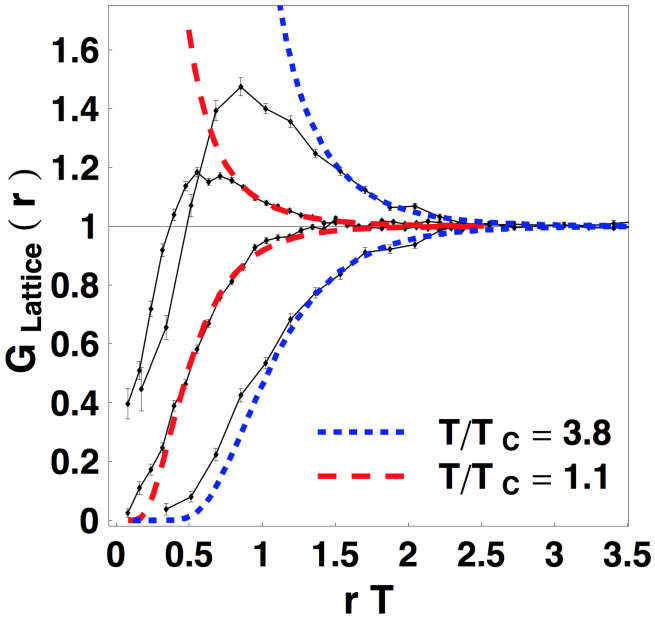

(a)

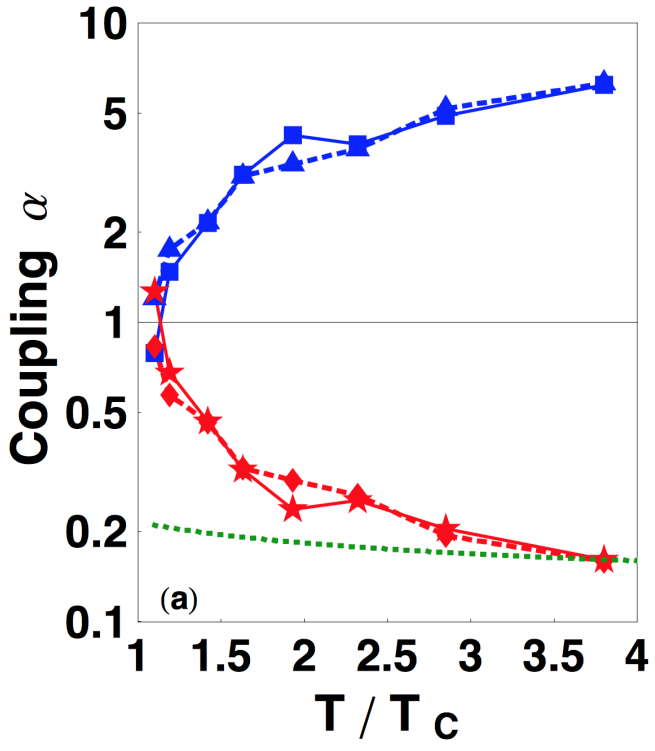

(b)

Figure 1.12: (a) Lattice correlations reproduced using classical molecular dynamics of an electric-magnetic plasma. (b) The electric and magnetic couplings needed to reproduce lattice correlations using classical molecular dynamics. Figures from Ref. [69].

Path-integral formulation of quantum mechanics

The path-integral formulation of quantum mechanics was developed by Feynman [71], who also extended this formalism to describe statistical mechanics, using periodic path integrals in Euclidean time. For many years this formalism has been used for perturbation theory, the derivation of Feynman diagrams at zero- and finite-temperature, and analytic semiclassical methods.

In quantum mechanics, the density matrix is related to the path integral by

$$\rho(x_i, x_f, t) = \int \mathcal{D}x(t) \exp\left\{\frac{i}{\hbar} S[x]\right\} , \tag{1.51}$$

where $S[x]$ is the functional action of the particular path x. For the purposes of this dissertation, we will use natural units, where $\hbar$ is set to unity. This path through time corresponds to the usual quantum mechanical evolution operator, $\exp\{i\hat{H}t\}$, where $\hat{H}$ is the Hamiltonian of the system.

To find the density matrix in finite temperature statistical mechanics, we transform to Euclidean time, $\tau = it$, with periodicity $\beta = T^{-1}$, setting the Boltzmann constant k_B to unity. Then, the thermal density matrix is given by

$$\rho(x_i, x_j, \beta) = \int \mathcal{D}x(t) \exp\left\{-S_{\mathrm{E}}[x]\right\} , \tag{1.52}$$

where S_{E} is the Euclidean action. The density matrix can also be decomposed in terms of its energy eigenstates

$$\begin{aligned} \rho(x_i, x_j, \beta) &= \sum_n \psi_n^*(x_i)\psi_n(x_j) \exp\left\{-E_n\beta\right\} \\ &= \langle\psi_n|\hat{\rho}|\psi_n|\psi_n|\hat{\rho}|\psi_n\rangle , \end{aligned} \tag{1.53}$$

where $\hat{\rho} = \exp\{-\beta\hat{H}\}$.

If we consider periodic paths, such that $x_i = x_j$, we define the *partition function*,

$$Z = \sum_n e^{-\beta E_n} = \mathrm{Tr}\left[e^{-\beta\hat{H}}\right] = \mathrm{Tr}[\hat{\rho}] , \tag{1.54}$$

from which the expectation value of the operator $\mathcal{O}$ is

$$\langle\mathcal{O}|\mathcal{O}\rangle = \frac{\mathrm{Tr}[\mathcal{O}\hat{\rho}]}{\mathrm{Tr}[\hat{\rho}]} = \frac{\mathrm{Tr}[\mathcal{O}\hat{\rho}]}{Z} . \tag{1.55}$$

For a many body system of N particles, we generalize the density matrix as $\rho(R_i, R_j, \beta)$, where $R_i = \{x_1, ..., x_N\}$ and $R_j = \{x'_1, ..., x'_N\}$.

Approximating the density matrix

The density matrix has the property of *squaring*,

$$\rho(x_i, x_j, \beta) = \int \mathrm{d}x_n \rho(x_i, x_n, \beta/2)\rho(x_n, x_j, \beta/2) , \tag{1.56}$$

which then allows the decomposition of the density matrix,

$$\rho(x_0, x_M, \beta) = \int \mathrm{d}x_1 ... \mathrm{d}x_{M-1} \times \rho(x_0, x_1, \tau) ... \rho(x_{M-1}, x_M, \tau) \,, \tag{1.57}$$

where $\tau = \beta/M$.

In general, the Hamiltonian operator of a system is the sum of the kinetic and potential energy operators, $\hat{H} = \hat{T} + \hat{U}$, and therefore we have that

$$e^{-\tau \hat{H}} = e^{-\tau(\hat{T}+\hat{V})} = e^{-\tau \hat{T}} e^{-\tau \hat{V}} e^{-\frac{\tau^2}{2}[\hat{T},\hat{V}]} \,. \tag{1.58}$$

If τ is small, then we have the *primitive approximation*,

$$e^{-\tau(\hat{T}+\hat{V})} \approx e^{-\tau \hat{T}} e^{-\tau \hat{V}} \,. \tag{1.59}$$

The Trotter formula tells us that this approximation becomes exact in the limit $\tau \to 0$. Using the fact that $\beta = M\tau$, we have that

$$e^{-\beta(\hat{T}+\hat{V})} = \lim_{M\to\infty} \left[e^{-\tau \hat{T}} e^{-\tau \hat{V}} \right]^M \,, \tag{1.60}$$

such that the kinetic and potential actions can be separated and treated individually. Provided M, the number of time steps per period of the Matsubara circle, is large enough, we can use this approximation in our numerical simulation to good accuracy. Therefore, in the primitive approximation, the density matrix is given by

$$\begin{aligned} \rho(R_i, R_{i+1}, \tau) &= \left\langle R_i | e^{-\tau \hat{T}} e^{-\tau \hat{V}} | R_{i+1} \right| \left. R_i | e^{-\tau \hat{T}} e^{-\tau \hat{V}} | R_{i+1} \right\rangle \\ &= \left\langle R_i | e^{-\tau \hat{T}} | R_{i+1} \right| \left. R_i | e^{-\tau \hat{T}} | R_{i+1} \right\rangle e^{-\tau V} \,. \end{aligned} \tag{1.61}$$

This quantity describes the degrees of freedom between time slice i and $i+1$. The kinetic matrix element for N particles can be computed using the eigenfunction expansion of the kinetic operator,

$$\left\langle R_i | e^{-\tau \hat{T}} | R_{i+1} \right| \left. R_i | e^{-\tau \hat{T}} | R_{i+1} \right\rangle = \frac{1}{(4\pi\lambda\tau)^{3N/2}} \exp\left\{ \left\{ -\frac{(R_i - R_{i+1})^2}{4\lambda\tau} \right\} \right\} , \tag{1.62}$$

where $\lambda = (2m)^{-1}$.

In the case of N identical bosons, we must also account for permutations of the particles,

$$\rho(R_i, R_j, \beta) = \frac{1}{N!} \sum_P \left\langle R_i | e^{-\beta \hat{H}} | P R_j \right| \left. R_i | e^{-\beta \hat{H}} | P R_j \right\rangle \,, \tag{1.63}$$

where P is the permutation operator. The partition function in the primitive approximation is then

$$
\begin{aligned}
Z =& \frac{1}{N!(4\pi\lambda\tau)^{3N/2}} \\
& \times \prod_{i=1}^{M-1} \prod_{n=1}^{N} \sum_{P} \int dx_{i,n} \\
& \times \exp\left\{ \left\{ -\frac{(x_{i,n} - x_{P,i+1,n})^2}{4\lambda\tau} - \tau V(x_{i,n}) \right\} \right\} .
\end{aligned}
\tag{1.64}
$$

From the partition function, one can calculate thermodynamic quantities. An example is the energy,

$$
\langle E \rangle = -\frac{1}{Z} \frac{\partial Z}{\partial \beta} .
\tag{1.65}
$$

In the primitive approximation,

$$
\langle E \rangle = \frac{3N}{2\tau} - \frac{1}{4\lambda M} \sum_{i=1}^{M-1} \sum_{n=1}^{N} \left(\left(\frac{x_{i,n} - x_{i+1,n}}{\tau} \right)^2 + 4\lambda V(x_{i,n}) \right) .
\tag{1.66}
$$

Path-integral Monte Carlo

Numerical evaluation of path integrals became feasible in late 1970s. Particularly, after pioneering work by Creutz on confinement in lattice gauge theory [72], Creutz and Freedman numerically computed path integrals for quantum-mechanical motion in quartic potential [73]. Some further examples of simulations with a few particles, such as two electrons in the the He atom and the four nucleons in a ^{4}He nucleus, are found in Ref. [74]. Starting in the early 1980s, supercomputers allowed numerical simulations of quantum many-body systems, such as liquid ^{4}He.

The basis for the path-integral Monte Carlo (PIMC) algorithm, as well as all the aforementioned simulations, is Metropolis Monte Carlo (MMC) [75]. In MMC, the state of a system is sampled by proposing a random change of state and accepting or rejecting this change based on a probability distribution that is a function of the state. In the case of PIMC, the probability distribution is given in terms of the Euclidean action associated with the state

$$
\pi(R) = e^{-S_E(R)} .
\tag{1.67}
$$

If we propose to move to a new state R', we can compute the acceptance probability of the move

$$
A(R \to R') = \min \left[1, \frac{\pi(R')T(R' \to R)}{\pi(R)T(R' \to R)} \right] ,
\tag{1.68}
$$

where $T(x \to x')$ is the transition probability from state x to state x'.

Each particle is represented by a Markov chain, with a *bead*, i.e. physical location, in each of the M time-slices in Matsubara time; the kinetic action is in the "links" between the beads of the same particle, and the potential action is between the beads in the same time-slice. One then samples changes in locations of these beads, accepting moves using

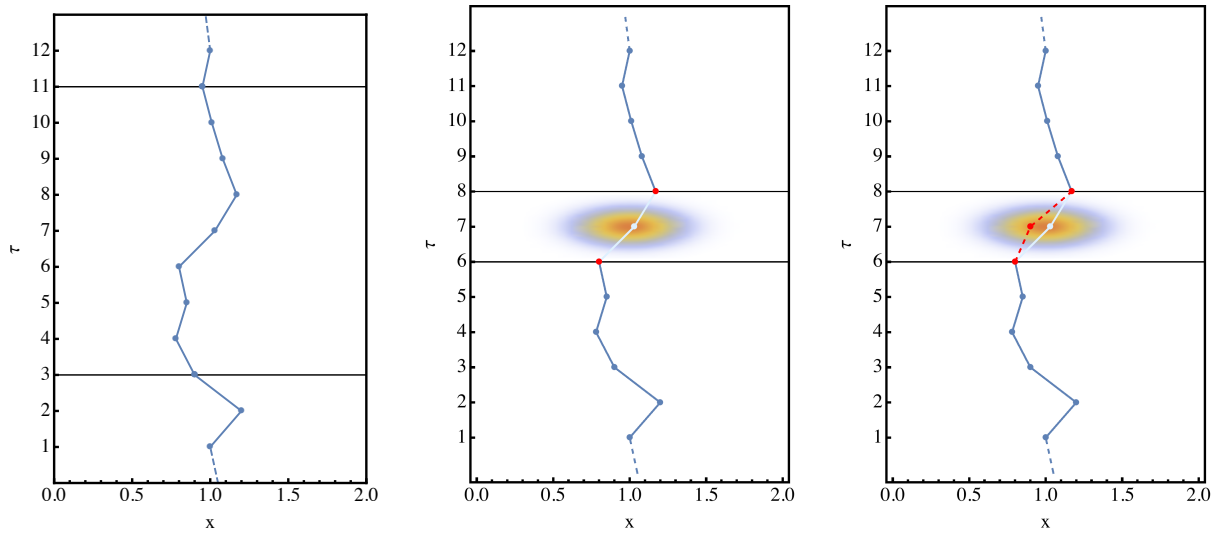

Figure 1.13: (a) The original path, (b) end points chosen on time slices $\tau = 6$ and 8, along with the free-particle gaussian distribution for $\tau = 7$, and (c) the new path (dashed, red).

the above probabilities based on the action, and records configurations from which one can calculate the partition function and other related thermodynamical quantities.

In the simulations described in this dissertation, we utilize *free-particle* and *bisection-method sampling* [76]. The sampling distribution for a bead on a path, without inter-particle interaction, is given by

$$T^*(R) \propto \rho(R_1, R)\rho(R, R_2)\,, \tag{1.69}$$

where we are sampling at point R, with the beads fixed in the previous and next time-slices. Evaluating this quantity, we have that

$$T^* \propto \exp\left[\frac{R - \left(\frac{R_1+R_2}{2}\right)}{2\lambda\tau}\right]\,, \tag{1.70}$$

which is a Gaussian distribution centered at $R_m = (R_1 + R_2)/2$, with width $\sqrt{\sigma} = \sqrt{\lambda\tau}$. In the absence of any potential interaction, samples taken from this distribution would have an acceptance rate of 100%. Thus, only the potential action would cause rejections, effectively "cutting holes" in this sampling distribution. A schematic of free-particle sampling is seen in Fig. 1.13.

In order to have a more computationally-feasible algorithm, it is necessary to perform multi-slice moves. The method used, known as the bisection method, starts from taking two time slices a certain distance apart in Matsubara time and interpolating, via a *bisection bridge*, the intermediate steps, using the free-particle sampling. A schematic of bisection-method sampling is seen in Fig. 1.14. In conventional PIMC, for bosons, the necessary permutations are sampled by swapping the endpoints of these bisection moves for two (or more) particles and reconstructing the intermediate time-slices for the new endpoints; this

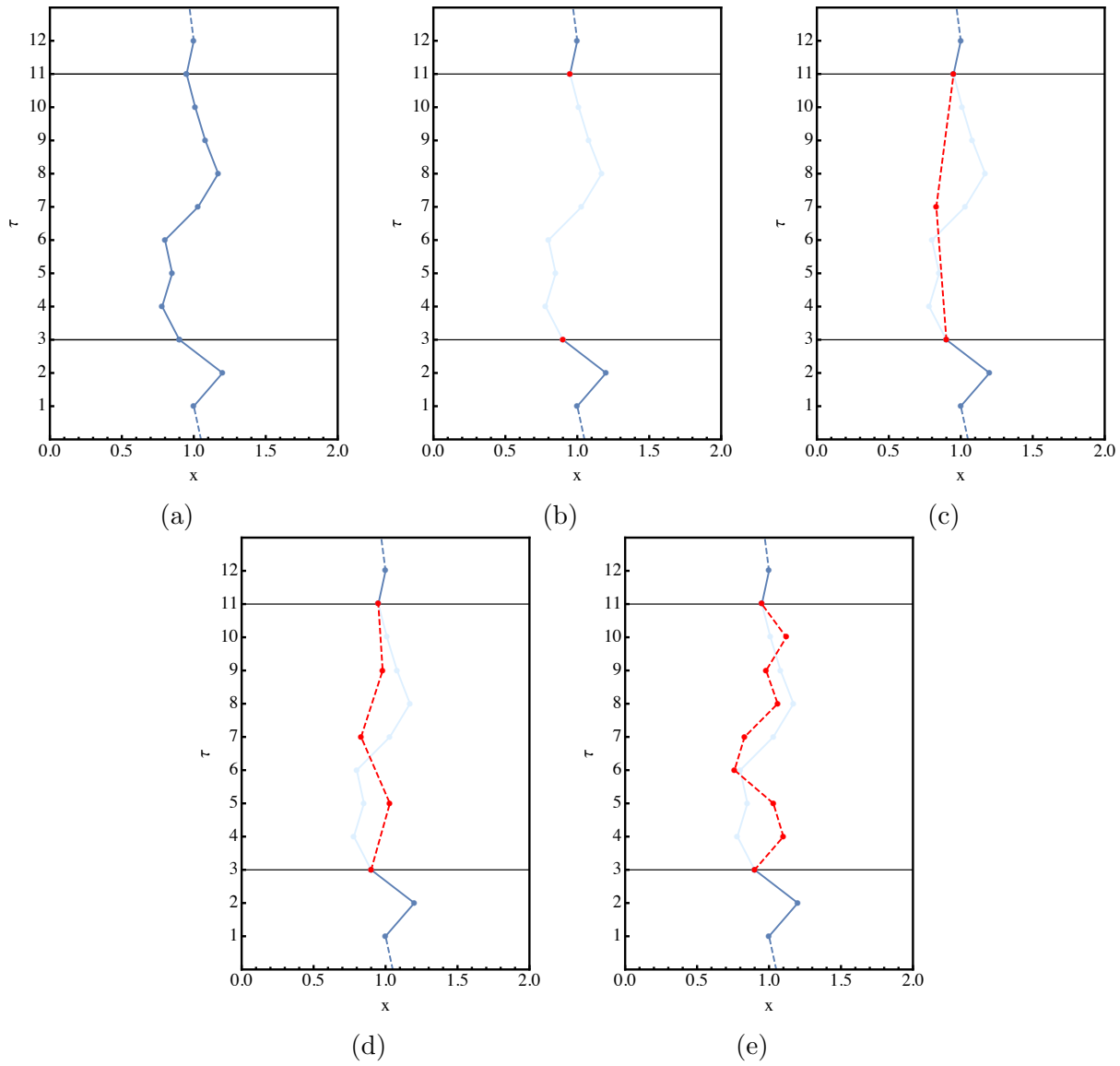

Figure 1.14: (a) The original path, (b) end points chosen on time slices $\tau = 3$ and 11, and (c), (d), (e) the construction of the new path (dashed, red).

is shown in Fig. 1.15. Further details on the PIMC method, including details on the update moves of the paths, can be found in the all-encompassing review by Ceperley [76] and in the thesis of Graves [77].

These permutation swaps, however, are very computationally intensive and significantly limit the size of the system that can be studied. An additional improvement to the path-integral Monte Carlo method was proposed by Boninsegni, et al. [78], called the *worm algorithm*.

The algorithm works by elevating the system to the grand canonical ensemble, introducing a single open world-line, known as a *worm*. The system of closed world lines, in the *diagonal* configuration, is treated just as in conventional PIMC. The dynamics of *off-diagonal* worm

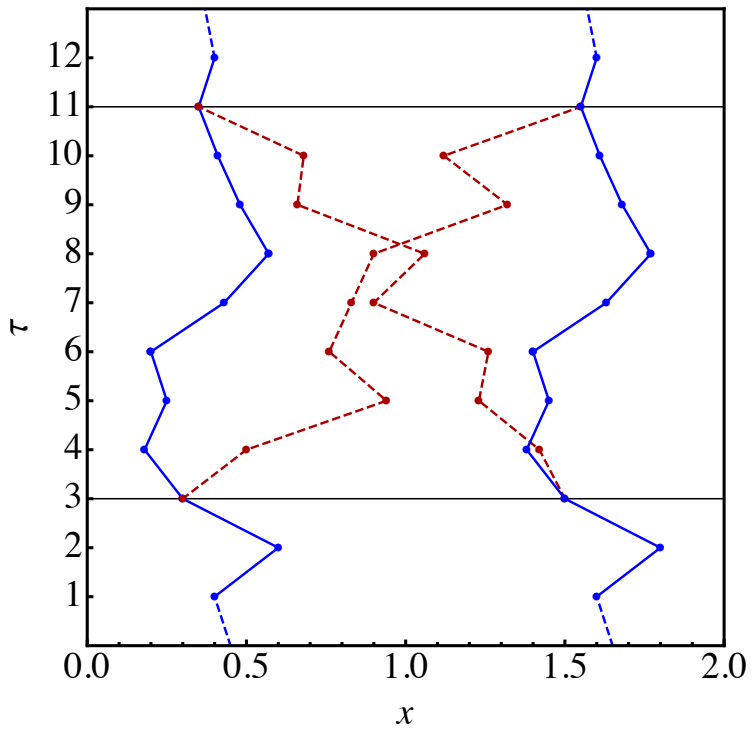

Figure 1.15: The original paths of two particles (blue) and the constructed new paths (red, dashed) after permutation.

is governed by the Matsubara Green function.

In each Monte Carlo step, in addition to the traditional bisection moves, world-lines can be opened and closed, and a worm can be introduced, advanced, receded, swapped, and removed. These moves are detailed in Ref. [78], and provide a natural way of introducing permutations to the system in a much less computationally-intensive fashion. Measurements are only made, identically in method to conventional PIMC, when the final result of a Monte Carlo step is a diagonal configuration (all world-lines closed). The introduction of this method has allowed one to study systems with hundreds of particles, an order of magnitude greater than the traditional PIMC pioneered by Ceperley.

The potential action for particle n in time-slice i, $V(x_{i,n})$, consists of external and inter-particle parts,

$$V(x_{i,n}) = V_{\text{ext}}(x_{i,n}) + \sum_{m \neq n} V_{\text{int}}(x_{i,n} - x_{i,m})\,. \tag{1.71}$$

In computing the potential action for the studies in this dissertation, we use the primitive approximation described above and compute the pair-potential for each pair of particle in the simulation. Computing this quantity in position space for periodic boundary conditions is feasible and accurate for short-range potentials, such as that for ^{4}He.

Numerical simulations of Coulomb systems are notoriously difficult to carry out, due to the long range nature of the forces. The electrostatic potential for a Coulomb interaction is

$$\Phi_{\text{Coulomb}}(x_{i,n}) = \sum_{\mathbf{l}} \sum_{m} \frac{q_m}{|x_{i,n} - x_{i,m} + \mathbf{l}|}\,, \tag{1.72}$$

where q_m and $x_{i,m}$ are the charge and location of the mth particle in the ith time-slice, respectively, and $\mathbf{l}$ is the vector that corresponds to the periodic image of each particle in space; the $m = n$ case is excluded only for $\mathbf{l} = 0$. Coulomb interactions, however, such as those of magnetic monopoles, are long-range, and therefore need, in the case of periodic boundary conditions, many images to be accurate. These sums therefore converge slowly and are not good for computational purposes.

Instead of summing solely in position space, we break up the sum into two rapidly converging pieces, one in position space and the other in reciprocal space, via a technique called Ewald summation [79, 80]. Written in this form, and making the conventional choice of the complementary error function for the real sum, the Coulomb potential is

$$\begin{aligned}\Phi_{\text{Coulomb}}(x_{i,n}) = &\sum_{\mathbf{l}} \sum_{m} \frac{q_m \text{erfc}(\alpha_{\text{cut}} |x_{i,n} - x_{i,m} + \mathbf{l}|)}{|x_i - x_j + \mathbf{l}|} \\ &+ \frac{4\pi}{V} \sum_{\mathbf{k} \neq 0} \sum_{j} \frac{q_m \exp\left\{\left[\frac{-\mathbf{k}^2}{4\alpha_{\text{cut}}}\right]\right\}}{\mathbf{k}^2} \exp\{[i\mathbf{k}(x_{i,n} - x_{i,m})]\} \\ &+ \frac{2\alpha_{\text{cut}}}{\sqrt{\pi}} q_n\,,\end{aligned} \tag{1.73}$$

where $\mathbf{k}$ is the wave vector in reciprocal space and V is the volume of the box. The parameter α_{cut} is known as the splitting parameter; it determines the cutoffs for the position and reciprocal space sums.

Bose-Einstein Condensation

One of Feynman's early applications of the path integral formalism was to the Bose-Einstein condensation phenomenon, which he connected to the appearance of Bose-clusters of particles; as the temperature drops from above T_c to below, the suppression of these clusters disappears. He qualitatively explained why an interacting quantum system may have a lower Bose-Einstein condensation critical temperature than in the case of free particles, famously applying this method to study liquid ^{4}He at near-zero temperatures, [81, 82].

A Bose-Einstein condensate occurs because bosons are allowed to possess the same quantum numbers; a BEC is a thermodynamic phase transition driven purely by statistics. In a BEC, a certain subset of particles in the system condense into a zero-momentum state; these particles are not separated in position space, but rather in Fourier space [83, 84].

We start by considering the density matrix for one particle (where r is used in place of $\vec{r}$, p is used in place of $\vec{p}$, and $\hbar = 1$ for simplicity) [77],

$$\rho_1(r - r') = \langle a^\dagger(r) a(r') \rangle \,, \tag{1.74}$$

where the $a^\dagger$ and a are creation and annihilation operators, respectively. These operators satisfy bosonic commutation relations,

$$[a^\dagger(r), a^\dagger(r')] = 0, \; [a(r), a^\dagger(r')] = \delta(r - r') \,. \tag{1.75}$$

For a many-body quantum system, the one-body density matrix is

$$\rho_1(r - r') = N \int \mathrm{d}r_2 ... \mathrm{d}r_N \Psi^\dagger(r, r_2, ..., r_N) \Psi(r', r_2, ..., r_N) \,. \tag{1.76}$$

This density matrix tells us about the correlation between the two many-body quantum states, Ψ, at $r, r_2, ..., r_N$ and $r', r_2, ..., r_N$. Due to being Hermitian, the density matrix can be expressed in terms of a sum of single-particle wave functions ψ,

$$\rho_1(r - r') = \sum_n N_n \psi_n^*(r) \psi_n(r') \,, \tag{1.77}$$

with the condition that the sum of occupation numbers gives the total number of particles in the system, $\sum N_n = N$. Inserting plane wave states, one gets

$$\rho_1(r - r') = \frac{N_0}{V} + \frac{1}{V} \sum_{p \neq 0} N_p e^{ip(r - r')} \,. \tag{1.78}$$

To find the number of bosons in a condensate, one must find the occupancy of the state with $n = 0$. Expressing the one-body density matrix in momentum space,

$$n(p) = \langle \Psi^\dagger(p) \Psi(p) \rangle = \frac{1}{(2\pi)^3} \int \mathrm{d}r \mathrm{d}r' e^{ip(r - r')} \langle \Psi^\dagger(r) \Psi(r) \rangle \,. \tag{1.79}$$

These last two expressions give a physical intuition for BEC. Eq. (1.78) tells us that a BEC presents itself as *long-range order*. When $r - r'$ becomes large, the non-zero momentum terms go to zero, and the zero-momentum term is all that is left as a contribution to the

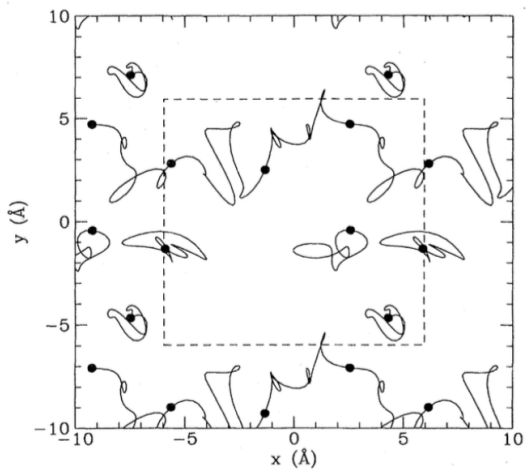

Figure 1.16: A path configuration of 2D liquid ^{4}He atoms in a periodic box. Black dots indicate the $\tau = 0$ time-slice, and are used for orientation. The dotted line denotes the periodic box. From Ref. [76].

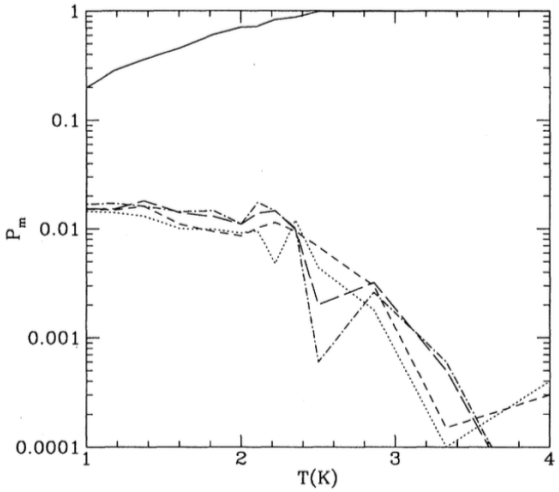

Figure 1.17: Fraction of particles in permutation cycles in a 3D simulation of 64 ^{4}He atoms. From Ref. [76].

density matrix. The momentum distribution occupancy Eq. (1.79) tends to zero at large separation distance, except for the zero-momentum state.

As a result, one of the signatures of a BEC are long-range correlations and de-localization of a particle path (the density matrix is *not* zero for $r - r' \gg 1$). Due to the fact that bosons are indistinguishable, their paths may permute, as stated above, which leads to long, winding permuted paths when $T \leq T_c$. Fig. 1.16 shows a path configuration taken from a simulation of 2D liquid ^{4}He in a periodic box. One can see that the paths of many of the helium atoms have permuted, which is the sign of a Bose-Einstein condensate. Fig. 1.17 shows the fraction of particles in *permutation cycles*, taken from a 3D simulation of 64 ^{4}He atoms. As the temperature is decreased and passes the critical temperature, larger and larger permutation cycles appear.

1.2 Outline of Dissertation

Chapter 2 attempts to answer the question of whether monopoles exist in QCD as they do in field theories such as the Georgi-Glashow model and those with extended supersymmetry. We focus on studying the semiclassical partition functions of objects known as instanton-dyons, which, in theories with scalars, are explicitly "Poisson dual" to the partition function of monopoles. We perform this transformation on the partition function of instanton-dyons in a pure gauge theory and interpret the resulting partition function as that of rotating monopoles.

In Chapter 3, we discuss the derivation of an effective model for quantum monopoles in SU(2) gauge theories from path-integral simulations. We perform path-integral simulations of Coulomb gases to identify the Bose-Einstein Condensation (BEC) critical temperature and radial correlation functions. Comparing the resulting ensembles with those found in pure-gauge lattice simulations, we are able to select parameters for a two-component Coulomb gas that accurately reflects the properties of monopoles found on the lattice. From the ensembles with appropriate parameters, we extract information about the monopole contribution to the QCD equation of state at and above the critical deconfinement temperature.

Next, in Chapter 4, we study the impact of monopoles on jet quenching observables, with focus on the nuclear modification factor R_{AA}, azimuthal anisotropy v_2, and dijet asymmetry A_j. We add a term corresponding to the monopoles to the Baier-Dokshitzer-Mueller-Peigne-Schiff (BDMPS) jet energy loss model and calculate the experimental observables for high-energy partons traversing the medium created in heavy-ion collisions at the LHC and RHIC.

Finally, in Chapter 5, we investigate whether monopoles can play a role in chiral symmetry breaking in QCD. We study properties of fermionic zero modes in the Georgi-Glashow model with fermions, and calculate the eigenvalue spectra of the Dirac operator for various temperatures above T_c using the monopole ensembles found earlier. From the eigenvalue spectra, we can find the magnitude of the chiral condensate, a signature of chiral symmetry breaking.

Chapter 2

Are There Monopoles in QCD?

This chapter is based on:

- A. Ramamurti, E. Shuryak, and I. Zahed (2018). Are there monopoles in the quark-gluon plasma? Phys. Rev. **D97**(11), 114028. doi:10.1103/PhysRevD.97.114028 arXiv:1802.10509.

We begin this dissertation with an argument for why we are studying monopoles in the context of QCD. The semiclassical description of the vacuum of gauge theories is based on the instanton solution [85]. At finite temperatures, however, the instanton solution has been shown to dissolve into instanton constituents, known as instanton-dyons [86–88]. For a review of these concepts, we direct the reader to Ref. [89]. Studies of the ensembles of instanton-dyons have explained the deconfinement and chiral symmetry restoration transitions both numerically [90, 91] and using a mean-field analysis [92, 93]. For a short review of these recent results, see Ref. [94].

The construction of the instanton-dyons in QCD starts from the 't Hooft-Polyakov monopole, but since there is no scalar field, the fourth component of the gauge field A_4 acts as the scalar adjoint "Higgs" field. These objects are *pseudo*-particles and not particles, existing only in the Euclidean formulation of the theory for which A_4 is real. Therefore, while instanton-dyons do lead to successful semiclassical applications, their use in phenomenological applications is severely limited. Another obstacle to the development of the theory if instanton-dyons is that their physical meaning remains rather obscure. We argue, in this chapter, that the explicitly-derived instanton-dyon gauge field configurations are nothing else but quantum paths of moving and rotating monopoles.

The first setting in which this idea was fleshed out was in the case of gauge theories with extended supersymmetry. In this setting, one can derive reliably *both* partition functions – in terms of monopoles and instanton-dyons – and show them to be equal [95–97]. The partition functions were, however, not summed up to an analytic answer, but shown instead to be related by the *Poisson duality*.

We begin first with a much simpler toy model of a rotator – a particle on a circle – at finite temperature, which we will treat as a pedagogical section that overviews the methodology we use later on. We will obtain two expressions for its partition function, one based on its excited states and one based on "winding paths" in Euclidean time. In this model, one can derive the analytic solution for both and see explicitly that they yield the same result.

Following this, we turn to theories with extended supersymmetry and review previous work in this area. We show how the Poisson duality works in this case – almost identically to the rotator model.

Finally, we turn to pure gauge theories at finite temperature, using the simplest version with two colors. We will derive the winding gauge configurations, periodic on the Matsubara circle, and the corresponding semi-classical partition function, that of the instanton-dyons. We then Poisson-transform it into another form, which we argue is counting occupations of the excited states of moving/rotating monopoles.

2.1 Quantum Rotator at Finite Temperature

A quantum rotator is a particle moving on a circle. Its location is defined by the angle $\alpha \in [0, 2\pi]$ and its action is defined by kinetic and topological parts

$$S = \oint \mathrm{d}t \, \frac{\Lambda}{2} \, \dot{\alpha}^2 + S_{\rm top}(\omega) \, , \tag{2.1}$$

where $\dot{\alpha} = \mathrm{d}\alpha/\mathrm{d}t$, and $\Lambda = mR^2$ is the corresponding moment of inertia for rotation.

The topological part $S_{\rm top} \sim \int \mathrm{d}t \dot{\alpha}(t)$ does not lead to any "force" – there is no contribution to the classical equation of motion – but it provides an extra phase factor in the quantum partition function. The phenomenon was introduced by Aharonov and Bohm [55]. We remind the reader that this phase is an external parameter which can be induced by a solenoid in extra dimensions, provided the rotating particle is charged and the time derivative is generalized to the long gauge-invariant derivative including the A_4 field.

The quantum mechanical spectrum of states is obtained via quantization of the angular momentum l and the partition function at temperature T is

$$Z_1 = \sum_{l=-\infty}^{\infty} \exp\left(- \frac{l^2}{2\Lambda T} + il\omega \right) , \tag{2.2}$$

where, for convenience, we normalized the Aharonov-Bohm contribution to a phase ω, to conform with literature [98]. Since the angular momentum l is integer-valued, each term in Z_1 is a periodic function of this phase, with a natural 2π period. Note also that positive and negative l cancel the imaginary part, so Z_1 is real. Finally, this sum is best convergent at small temperature T, where only a few states close to the ground state with $l = 0$ dominate.

In the dual approach, finite temperature is introduced via the Euclidean Matsubara time defined on *another* circle $\tau \in [0, \beta \equiv 1/T]$. The path integral that leads to the partition function needs to be done over the periodic paths, $x(0) = x(\beta)$, so one may say that the Euclidean theory is a particle on a double torus.

Classes of paths which make a different number n of rotations around the original circle can be defined as "straight" classical periodic paths

$$x_n(\tau) = 2\pi n \frac{\tau}{\beta} \, , \tag{2.3}$$

plus small fluctuations around them. Carrying out a Gaussian integral over them leads to the following partition function,

$$Z_2 = \sum_{n=-\infty}^{\infty} \sqrt{2\pi\Lambda T}\, \exp\left(-\frac{T\Lambda}{2}(2\pi n - \omega)^2 \right). \tag{2.4}$$

The key point here is that these quantum numbers, l used for Z_1 and n for Z_2, are very different in nature. In Z_1, each term of the sum is periodic in ω, while in Z_2, this property is recovered only after summation over n. The temperature T in Z_2 is in the numerator of the exponent, so this sum converges best at *high* temperature, unlike the sum in Z_1. Indeed, at high T the Matsubara circle becomes small and the path integral is dominated by paths with small number of windings.

Despite such differences, both expressions are in fact the same! In this toy model, it is not difficult to do the sums numerically and plot the results. Furthermore, one can also derive the analytic expressions, expressible in terms of the elliptic theta function of the third kind,

$$Z_1 = Z_2 = \theta_3\left(-\frac{\omega}{2}, \exp\left(-\frac{1}{2\Lambda T} \right) \right), \tag{2.5}$$

which is plotted in Fig. 2.1 for few values of the temperature T.

Mathematically, the identity of the two sums can be traced to the fact that our path integral is defined on two circles, or, equivalently, a 2d torus, and the circles can be interchanged. In string theory, such relations are known as T-duality [99]. In practice, these are the low-temperature and the high-temperature approximations, often used without noticing the exact summation and duality.

Even if one is not able to identify the sums as the same elliptic function, the equality can be seen from the observation that the sum Z_1 is the discrete Fourier transform of the Gaussian, which is known to be the "periodic Gaussian" appearing in Z_2. One can further recognize that the identity of the two sums is just a particular case of a more general relation known in mathematics as the *Poisson summation formula*, valid not only for a Gaussian but for arbitrary functions. For reference, we mention here one particular version [100],

$$\sum_{n=-\infty}^{\infty} f(\omega + nP) = \sum_{l=-\infty}^{\infty} \frac{1}{P} \tilde{f}\left(\frac{l}{P}\right) e^{i2\pi l\omega/P}, \tag{2.6}$$

where $f(x)$ is some function, $\tilde{f}$ is its Fourier transform, and P is the period of both sums as a function of the "phase" ω.

2.2 Semiclassical Theory and Monopoles

2.2.1 Theories with Extended Supersymmetry

All of the following discussion concerns a Euclidean theory defined on $R^3 \times S^1$. In this section, unlike in the following one, all of the fields, including the fermions, have periodic boundary conditions on S^1, and therefore supersymmetry is *not* broken.

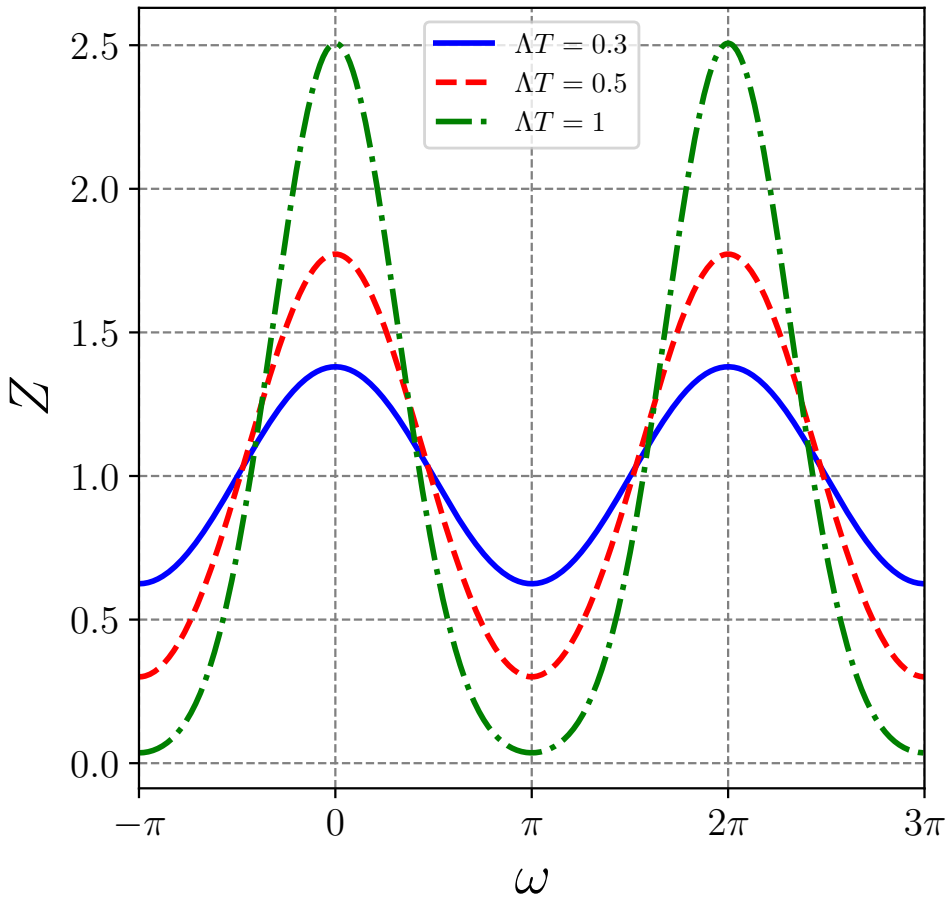

Figure 2.1: The partition function Z of the rotator as a function of the external Aharonov-Bohm phase ω (two periods are shown to emphasize its periodicity). The (blue) solid, (red) dashed and (green) dash-dotted curves are for $\Lambda T = 0.3, 0.5, 1$.

We study the weak coupling $g \ll 1$ scenario, which makes the instantons and their constituents – as well as the monopoles with actions/masses $O(1/g^2)$ – heavy enough to trust the dilute gas approximation. This lets us focus on a single object and avoid finite-density (many-body) complications. In the $\mathcal{N} = 4$ theory, the charge does not run and the coupling g is simply an input parameter. In the $\mathcal{N} = 2$ theory, however, the coupling does run, and one needs to select the circumference of the circle β to be small enough such that the corresponding frequencies $\sim 2\pi/\beta$ are large enough to ensure weak coupling.

Compactification of one coordinate to the circle is needed to introduce "holonomies," gauge invariant integrals over the circle $\oint \mathrm{d}x_\mu A^\mu$, $\oint \mathrm{d}x_\mu C^\mu$ of the electric and magnetic potentials, respectively. Their values can have non-zero expectation values, which can be viewed as external parameters given by Aharonov-Bohm fluxes through the circle induced by a solenoid in extra dimensions. These holonomies will play important role in what follows. Dorey et al. [98] call these external parameters ω and σ, respectively.

The theories with extended supersymmetry $\mathcal{N} = 2, 4$ have one and six adjoint scalar fields, respectively. These two theories also have, respectively, 2 and 4 fermions, so that

there is balance between bosonic and fermionic degrees of freedom.

In order to make the discussion simpler, one assumes the minimal non-Abelian color group $SU(N_c)$ with the number of colors $N_c = 2$. This group has only one diagonal generator τ^3, breaking the color group $SU(2) \to U(1)$. For simplicity, all vacuum expectation values (VEV) of the scalars, as well as both holonomies are assumed to be in the diagonal direction, so the scalar VEVs and ω and σ are single-valued parameters without indices. In the general group $SU(N_c)$, the number of diagonal directions is the Abelian subgroup, and thus the number of parameters is $N_c - 1$.

Considering the theories on the Coulomb branches, with nonzero VEVs of the scalars $\phi_A, A = 1 \dots 6$, one can naturally use the original BPS version of the 't Hooft-Polyakov monopole, with a mass

$$M = \left(\frac{4\pi}{g^2}\right)\phi\,. \tag{2.7}$$

We will only discuss the $\mathcal{N} = 4$ case, following Dorey and collaborators [98]. Six scalars and two holonomies can be combined to vacua parameterized by 8 scalars, extended by supersymmetry to 8 chiral supermultiplets. These 8 fermions have zero modes, describing their binding to monopoles.

The SU(2) monopole has four collective coordinates, three of which are related with translational symmetry and location in space, while the fourth is rotation around the τ^3 color direction,

$$\hat{\Omega} = \exp(i\alpha\hat{\tau}^3/2)\,. \tag{2.8}$$

Note that such a rotation leaves unchanged the VEVs of the Higgses and holonomies, as well as the long-distance Abelian $A^3_\mu \sim 1/r$ tails of the monopole solution. Nevertheless, these rotations are meaningful because they do rotate the monopole core – made up of non-Abelian A^1_μ, A^2_μ fields – nontrivially. It is this rotation in the angle α that makes the monopole problem similar to a quantum rotator. As was explained by Julia and Zee [101], the corresponding integer angular momentum is nothing but the electric charge of the rotating monopole, denoted by q.

One can derive the partition function at certain temperature, which (anticipating the next sections) we will call $T \equiv 1/\beta$,

$$\begin{aligned} Z_{\rm mono} \quad &= \sum_{k=1}^{\infty}\sum_{q=-\infty}^{\infty}\left(\frac{\beta}{g^2}\right)^8 \frac{k^{11/2}}{\beta^{3/2}M^{5/2}} \\ &\times \exp\left(ik\sigma - iq\omega - \beta kM - \frac{\beta\phi^2 q^2}{2kM}\right), \end{aligned} \tag{2.9}$$

where k is the magnetic charge of the monopole. The derivation can be found in Ref. [98]; we only comment that the temperature in the exponent only appears twice, in the denominators of the mass and the rotation terms, as expected. The two other terms in the exponent, $\exp(ik\sigma - iq\omega)$, are the only places where holonomies appear, as the phases picked up by magnetic and electric charges over the circle.

Now we derive an alternative 4d version of the theory, in which we will look at gauge field configurations in all coordinates including the compactified "time coordinate" τ. These

objects are versions of instantons, split by a nonzero holonomy into instanton constituents. Since these gauge field configurations need to be periodic on the circle, and this condition can be satisfied by paths adding arbitrary number n of rotations, their actions are

$$S^n = \left(\frac{4\pi}{g^2}\right)\left(\beta^2|\phi|^2 + |\omega - 2\pi n|^2\right)^{\frac{1}{2}}, \tag{2.10}$$

including the contribution from the scalar VEV ϕ, the electric holonomy ω, and the winding number of the path n. In the absence of the holonomies, the first term would be M/T as one would expect.

The partition function then takes the form [98]

$$\begin{aligned} Z_{\rm inst} &= \sum_{k=1}^{\infty}\sum_{n=-\infty}^{\infty}\left(\frac{\beta}{g^2}\right)^9 \frac{k^6}{(\beta M)^3} \\ &\times \exp\left(ik\sigma - \beta k M - \frac{kM}{2\phi^2\beta}(\omega - 2\pi n)^2\right), \end{aligned} \tag{2.11}$$

where $M = (4\pi\phi/g^2)$, the BPS monopole mass without holonomies; thus the second term in the exponent is interpreted as just the Boltzmann factor. The "temperature" appears in the unusual place in the last term (like for the rotator toy model). The actions of the instantons are large at high-T (small circumference β); the semiclassical instanton theory works best at high-T.

The Poisson duality relation between these two partition functions, Eqs. (2.9) and (2.11), was originally pointed out by Dorey and collaborators [98]. In this chapter, it was explained earlier for the simpler toy model of a quantum rotator. Its mathematical origins were presumably clarified enough by our toy model, and it is perhaps enough to remind the reader that the two circles (or the double torus) at play are the angle $\alpha \in [0, 2\pi]$ related with the rotation of the monopole in ordinary/color space and the compactified coordinate $\tau \in [0, \beta]$.

2.2.2 Pure Gauge Theories

Now consider theories without adjoint scalars, which do not have an obvious 't Hooft-Polyakov monopole solution. One example of such a theory discussed in Ref. [98] is the $\mathcal{N} = 1^*$ theory obtained from the $\mathcal{N} = 4$ theory by giving a mass to the three chiral multiplets, which, in the IR, eliminates 3 out of 4 fermions and all 6 scalars. We will not discuss this particular case, but proceed directly to pure gauge theory, starting from the instantons.

At zero temperature, the Euclidean space R^4 is symmetric in all four coordinates, and thus the corresponding saddle points of the integral over fields – the instantons – are 4d spherically symmetric. At finite temperatures, Euclidean time is defined on the circle $\tau \in [0, \beta]$. The corresponding solitons – the calorons – are deformed periodic instantons.

In order to keep the weak coupling and the small density approximation valid, we need to consider sufficiently high T. What this means practically will be discussed at the end of the chapter. For simplicity, for now we will also ignore the issue of a dynamically generated

potential and mean value of the electric holonomy on the time circle, and continue to consider it to be an external parameter; we are therefore considering a "deformed" gauge theory.

The presence of the holonomy is known to split the calorons into N_c constituents [86–88] known as instanton-dyons (or instanton-monopoles). The holonomy eigenvalues $\mu_i, i = 1 \dots N_c$ enter the gluon and instanton-dyon masses via their differences $\nu_i = \mu_{i+1} - \mu_i$. We will consider only the simplest case of the number of colors $N_c = 2$, in which case there is a single holonomy parameter. The caloron is composed of two types of the self-dual dyons, known as the time-independent M dyon and the time-twisted L dyon [102].

Following the discussion above, we need to consider a larger set of saddle-point configurations with all possible periodic paths. To be explicit, let us derive the corresponding semiclassical configurations. One starts with the static BPS monopole, with the A_4 component of the gauge field now as the adjoint scalar. In the simplest "hedgehog" gauge, the gauge fields are

$$\begin{aligned} A_4^a &= n_a v\left(\coth(vr) - \frac{1}{vr}\right), \\ A_i^a &= \epsilon_{aij}\frac{n_j}{r}\left(1 - \frac{vr}{\sinh(vr)}\right), \end{aligned} \tag{2.12}$$

where $n_a = x_a/r$ is the spatial unit vector and v is the VEV of A_4 at large distances $r \to \infty$.

The twisted solution is obtained in two steps. The first is the substitution

$$v \to n(2\pi/\beta) - v\,, \tag{2.13}$$

and the second is the gauge transformation with the gauge matrix

$$\hat{\Omega} = \exp\left(-\frac{i}{\beta} n\pi\tau\hat{\sigma}^3\right), \tag{2.14}$$

where we recall that $\tau = x^4 \in [0, \beta]$ is the Matsubara time. The derivative term in the gauge transformation adds a constant to A_4 which cancels out the unwanted $n(2\pi/\beta)$ term, leaving v, the same as for the original static monopole. After "gauge combing" of v into the same direction, this configuration – we will call L_n – can be combined with any other one. The solutions are all self-dual, but the magnetic and (the Euclidean) electric charges are negative for positive n, opposite to the original BPS monopole M for which both are positive. The neutral combination $M + L_1$ is the finite-T instanton. Their non-linear exact superposition was derived in Refs. [86, 87].

The action corresponding to this solution is

$$S_n = (4\pi/g^2)|2\pi n/\beta - v|\,. \tag{2.15}$$

The contribution to the partition function requires the calculation of the pre-exponent, due to quantum fluctuations around the L_n solution, which has not been calculated explicitly as of yet.

In the particular case of the $L = L_1$ dyon, the contribution to the partition function can be obtained from the explicit calculation of the moduli for the caloron (finite temperature

instanton, the M+L system) in Ref. [102]. For the color SU(2) group, taking the limit of large separation between the dyons, the L-dyon contribution has the form

$$\mathrm{d}Z_L \sim \mathrm{d}^3x_L \left(\frac{8\pi^2}{g^2}\right)^2 e^{-\left(\frac{8\pi^2}{g^2}\right)\bar{\nu}} \left(2\pi\bar{\nu}\right)^{8\bar{\nu}/3}, \tag{2.16}$$

with $\bar{\nu} = 1 - \nu$ and $\nu = vT/2\pi$. Here the exponent corresponds to the classical action, the power 2 of the first semiclassical factor stems from zero modes $N_{\text{zero modes}}/2$, and the last factor is from the large distance limit of the volume of moduli space according to Ref. [102]. See also Appendix C of Ref. [90].

Unlike in the theories with extended supersymmetry, in QCD-like theories there are no (partial) cancellations in the determinant of the nonzero modes between bosons and fermions, and the normalization constant require tedious calculation of the nonzero mode part which was not yet done. The renormalizability however requires that it appends the bare charge in the action to the correct running coupling at the relevant scale is reproduced. This means that one expects the exponent to read

$$\mathrm{d}Z_{L_n} \sim \mathrm{d}^3x_L \exp\left[-|2\pi Tn - v|\left(\frac{8\pi^2}{g_0^2} + \frac{22}{3}\log\left(\frac{p_0}{|2\pi Tn - v|}\right)\right)\right], \tag{2.17}$$

where the coupling g_0 is the defined at the normalization scale p_0. Similarly, the power of the action in numerator must be appended by the two-loop corrections to the two-loop beta function, and so on.

For our subsequent discussion, we will ignore the running and only keep the first term, taking the mean coupling to be just a constant at a characteristic $p_0 = 2\pi T\langle\bar{\nu}\rangle$, say

$$S_0 \equiv S_L + S_M = \frac{8\pi^2}{g_0^2} = 10\,. \tag{2.18}$$

Simulations of instanton-dyon ensembles [90] were done for S_0 ranging from 5 to 13, and thus defining a rather large range of dyon densities. Higher-twist instantons L_n for $n > 1$ or $n < 0$ are all strongly suppressed and in practice can be ignored; the instanton-dyon ensemble calculations performed in Ref. [90] only included the $n = 0$ time independent dyon M and the first twisted dyons L_1 because, in this range of temperatures, the holonomy phase ω changes from a small value to π at the confining phase transition, where ω and $2\pi - \omega$ are comparable.

In the present calculation, we will keep all of them, preserving exact periodicity, and write the semiclassical partition function as

$$Z_{\text{inst}} = \sum_n e^{-\left(\frac{4\pi}{g_0^2}\right)|2\pi n - \omega|} \tag{2.19}$$

It is periodic in the holonomy, but note that, unlike in Eq. (2.11), it has a modulus rather than a square of the corresponding expression in the exponent. This is due to the fact that the sizes of L_n and their masses are all defined by the same combination $|2\pi n - \omega|T$ and therefore the moment of inertia $\Lambda \sim 1/|2\pi n\beta - v|$.

According to the general Poisson relation, Eq. (2.6), the Fourier transform of the corresponding function appearing in the sum in Eq. (2.19) reads

$$\begin{aligned} F\left(e^{-A|x|}\right) \equiv & \int_{-\infty}^{\infty} \mathrm{d}x\, e^{i2\pi\nu x - A|x|} \\ = & \frac{2A}{A^2+(2\pi\nu)^2}\,, \end{aligned} \tag{2.20}$$

and therefore the dual partition function, which we propose is that of the monopole, is

$$Z_{\rm mono} \sim \sum_{q=-\infty}^{\infty} e^{iq\omega - S(q)}\,, \tag{2.21}$$

where

$$\begin{aligned} S(q) \quad & = \log\left(\left(\frac{4\pi^2}{g_0^2}\right)^2 + q^2\right) \\ & \approx 2\log\left(\frac{4\pi^2}{g_0^2}\right) + q^2\left(\frac{g_0^2}{4\pi}\right)^2 + \dots\,, \end{aligned} \tag{2.22}$$

where the approximation is for $q \ll 4\pi^2/g_0^2$.

The action of a monopole, although still formally large in weak coupling, is only a *logarithm* of the semiclassical parameter; these monopoles are therefore lighter than instanton-dyons. While the specific value of the monopole action

$$S_{\rm mono} = 2\log\left(\frac{4\pi^2}{g^2}\right) \approx 2\log(4) \approx 2.8$$

can still be considered larger than 1, one may ask whether it can be even parametrically modified by the powers of logs in the instanton partition function. In summary, it is not yet clear whether those monopoles are or are not truly semiclassical.

The very presence of an object that admits rotational states implies that the monopole core is not spherically symmetric. The Poisson-rewritten partition function has demonstrated that the rotating monopoles are *not* the rigid rotators, because their action, Eq. (2.22), depends on the angular momentum q and is quadratic only for small values of q. The slow (logarithmic) increase of the action with q implies that the dyons are in fact shrinking with increased rotation. In the moment of inertia, this shrinkage is more important than the growth in the mass, as the size appears quadratically. As strange as it sounds, it reflects on the corresponding behavior of the instanton-dyons L_n with the increasing n.

2.2.3 Monopoles in QCD

Let us first recall the setting and conclusions of the preceding section. The coupling is presumed to be small, so the action at the relevant scale is large $4\pi/g^2 \gg 1$ and the semiclassical calculation is well controlled. This implies that the corresponding temperature is "high enough." The holonomies ω, σ, treated as external Aharonov-Bohm phases imposed

on the system, create a certain "Higgsing" of the gluons, with only the diagonal ones remaining massless. Calorons are split into the instanton-dyons, and the semiclassical partition function, appended by all L_n contributions, can be calculated.

What we would actually like to study is QCD with quarks, at temperatures around the deconfinement transition $T \sim T_c$. Indeed, heavy-ion collisions create matter with T between roughly $2T_c \approx 300$ MeV and $0.5T_c$. Most finite-T lattice studies are devoted to this temperature range as well. In this regime the action of the L_1 instanton-dyon is numerically

$$S_{L_1} = \frac{4\pi^2}{g^2} \sim 4$$

with L_n having larger actions respectively. So, the semiclassical suppression $\exp(-S_{L_1}) \approx e^{-4}$ seems to be robust enough to keep only L_1 and M dyons. But, including the pre-exponents, one finds that the ensemble is not really dilute, and in order to perform the integration over the collective variables, one needs to solve a nontrivial many-body problem of a dense instanton-dyon plasma. The instanton-dyon ensemble of M, L_1 dyons does shift the potential for the electric holonomy dynamically to its "confining" value, for $T < T_c$. Semiclassical ensembles of instanton-dyons also explain chiral symmetry breaking, and their changes with flavor-dependent quark periodicity phases. Further development of the semiclassical theory is, therefore, well justified.

2.3 Summary

The main point of this work is that *any* semiclassical partition function, once derived, can be Poisson-rewritten into an identical "Hamiltonian" form, with the sum over certain excited states. We have shown how one can do so for pure gauge theory, without scalars, using relatively schematic form of the semiclassical partition function, for which we calculated its Poisson dual. We proposed that the resulting partition function can be interpreted as being generated by *moving and rotating monopoles*.

Although such rotations are well known in principle as Julia-Zee dyons with *real* electric charge (unlike that of the instanton-dyons, which only exist in the Euclidean world) and studied in theories with extended supersymmetries, to our knowledge the existence of multiple rotational states of monopoles has not yet been explored in monopole-based phenomenology. In particular, one may wonder how the existence of multiple rotational states affects their Bose-condensation at $T < T_c$, the basic mechanism behind the deconfinement transition. The electric charges of the rotating monopoles should, therefore, also contribute to the jet quenching parameter $\hat{q}$ and the viscosity, which was not included before.

We note that perhaps a useful "middle ground" connecting the two regimes – the idealized semiclassical dilute gas and the real-life finite-T QCD – would be lattice studies of the gauge theory with an *induced holonomy* at high T. To our knowledge, this has not been done in detail.

The first steps in this direction were semiclassical studies by introduction of certain masses, by Dorey et al. using $\mathcal{N} = 4 \to \mathcal{N} = 1$ [98] and by Unsal et al. for $\mathcal{N} = 2$ deformed toward pure gauge theory [96]. The conjectured continuity of both the confined and deconfined phases, from dilute to dense regimes, was never studied nor confirmed.

Lattice measurements of the holonomy potential for the SU(2) and SU(3) gauge theories with fixed external holonomy have been performed in Ref. [103]. The perturbative renormalized potential was derived and compared to these data in Ref. [104]. Such a subtraction opens the door to studies of the monopole contribution, which have not been attempted as of yet. Other lattice studies, of the "deformed QCD" with an extra holonomy-dependent term in the action, were carried out in Ref. [105]. Finally, the introduction of light quarks would allow study of fermionic zero modes of both semiclassical instanton-dyons and monopoles, giving another way to test their mutual correspondence.

Chapter 3

Simulating Ensembles of Monopoles

This chapter is based on:

- A. Ramamurti and E. Shuryak (2017). Effective Model of QCD Magnetic Monopoles From Numerical Study of One- and Two-Component Coulomb Quantum Bose Gases. Phys. Rev. **D95**(7), 076019. doi:10.1103/PhysRevD.95.076019 arXiv:1702.07723.

We now focus on the properties of a quantum ensemble of monopoles. The purpose of this work is to elevate the classical dual Coulomb plasma picture [69] to an effective quantum many-body theory of monopole ensembles. The need for a quantum model is clear: without one, it would not be possible to study the Bose-Einstein condensation transition that is essential to the dual superconductor model of confinement.

Lattice simulation of gauge theories include magnetic monopoles as certain solitons made of glue. These simulations are based on first principles, namely the QCD Lagrangian. However, they also include many more degrees of freedom – such as quark and gluon quasiparticles at $T > T_c$ – and are therefore very expensive. Our aim is to create an effective model of the monopoles and quantify their contributions to various observables. In doing so, we realize that one can only separate the monopoles from other degrees of freedom to a certain degree.

To simulate these quantum Coulomb Bose systems, we will use Path-Integral Monte Carlo (PIMC). This method has been widely used since the 1980s; for a quick review, see Sec. 1.1.3, and for thorough reviews, see Refs. [76, 77].

We will first investigate how the Coulomb interaction between the magnetic quasiparticles affects the critical temperature T_c of their BEC phase transition, through numerical simulations of one- and two-component (plus and minus charged) Bose gases at different coupling strengths. We will map the results of our simulations for the two-component Bose gas to those found on the lattice in order to find the parameters for our model that yield the same effective behavior of the magnetic monopoles, and make estimates of the monopole contribution to QCD thermodynamics.

3.1 Finding the Critical Temperature for BEC

Here, we will briefly describe three methods of finding the critical condensation temperature to be used below. These are more feasible than the brute force approach, based on a calcu-

lation of the free energy of the ensemble with subsequent determination of specific heat and its peak.

The first is the method outlined by Pollock and Ceperley [106], and Pollock and Runge [107], based on supercurrent and its finite-size scaling. The second method, developed by Cristoforetti and Shuryak [108], uses the permutation-cycle statistics of the system to find T_c. This method has not been used in analysis of PIMC simulations, so this work also seeks to test the accuracy of this method. It has been used in Refs. [64, 65] for lattice monopoles, confirming that deconfinement T_c is indeed the BEC transition of the monopoles. Finally, we will attempt to use a machine learning algorithm to classify which path configurations are condensed, and use the classifications to determine T_c.

3.1.1 Method 1: Finite-Size Scaling

Following the discussion in Refs. [106, 107], we can identify the winding number of the system with the superfluid fraction, and then using finite-size scaling, determine T_c. In experimental settings, the normal and superfluid components of a system are determined from boundary behavior. If we introduce a velocity v to the boundaries of our system, we have a new density matrix

$$\rho_v = \exp\{\beta H_v\}\,, \tag{3.1}$$

with

$$H_v = \sum_j \frac{(\mathbf{p}_j - m\mathbf{v})^2}{2m} + V\,. \tag{3.2}$$

The normal component of the fluid is the portion that responds to this boundary motion, so we can write for the total momentum,

$$\frac{\rho_N}{\rho} N m \mathbf{v} = \langle \mathbf{P}|\mathbf{P}\rangle_v\,. \tag{3.3}$$

We have for the free energy of this system,

$$\exp\{-\beta F_v\} = \mathrm{Tr}\{\rho_v\}\,, \tag{3.4}$$

so we can write

$$\frac{\rho_N}{\rho} N m \mathbf{v} = -\frac{\partial F_v}{\partial \mathbf{v}} + N m \mathbf{v}\,, \tag{3.5}$$

or, equivalently,

$$\frac{\rho_s}{\rho} = \frac{\partial(F_v/N)}{\partial(\frac{1}{2}mv^2)} \to \frac{\Delta F_v}{N} = \frac{1}{2} m v^2 \frac{\rho_s}{\rho} + \ldots \tag{3.6}$$

In the path integral formalism, the density matrix with a velocity obeys the Bloch equation with moving walls, with periodic boundary conditions such that it is identical with a translation by a lattice vector. We can define a transformed density matrix, ρ', by

$$\rho_v(R, R'; \beta) = \exp\left\{ i \frac{m}{\hbar} \mathbf{v} \cdot \sum_j (\mathbf{r}_j - \mathbf{r}'_j) \right\} \rho'(R, R'; \beta)\,. \tag{3.7}$$

This new density matrix obeys the Bloch equation in the case of *stationary walls*, but obtains a factor of $\exp\left\{i\frac{m}{\hbar}\mathbf{v}\cdot\mathbf{L}\right\}$ in periodic translations. Keeping track of the number of times the periodic boundary conditions are applied can be done with the definition of a *winding number*, which counts the number of times a particle winds around the spatial directions of periodic box before returning to its "original" location.

The free energy change induced from a velocity v can be written as

$$\exp\left\{\beta\Delta F_v\right\} = \exp\left\{i\frac{m}{\hbar}\mathbf{v}\cdot\mathbf{W}L\right\}\,, \tag{3.8}$$

$$\beta\Delta F_v = \frac{m^2v^2}{2\hbar^2}\frac{\langle W^2|W^2\rangle\, L^2}{3} + ... \tag{3.9}$$

We can thus identify, with use of Eq. (3.6),

$$\frac{\rho_s}{\rho} = \frac{m}{\hbar}\frac{\langle W^2|W^2\rangle\, L^2}{3\beta N}\,. \tag{3.10}$$

From assumptions of finite-size scaling, we have that, near T_c,

$$\frac{\rho_s}{\rho}(T,L) = L^{-1}Q(L^{-1/\nu}t)\,, \tag{3.11}$$

with $t = (T-T_\mathrm{c})/T_\mathrm{c}$. As a result, the functions $L\rho_s/\rho(T,L)$, for different values of L, should all cross at T_c, barring some minor corrections, expanded upon in Ref. [107].

3.1.2 Method 2: Permutation Cycles

Following the example of Ref. [64], the partition function of a *non-interacting* ideal gas of bosons can be broken up into a product of contributions of k-cycles – where, for example, the permutation $(1,2,3)\to(2,3,1)$ is considered a 3-cycle – as

$$Z = \frac{1}{N!}\sum_P\prod_k z_k^{n_k}\,, \tag{3.12}$$

where n_k is the number of k-cycles present in the system. Feynman's idea was that the sum over Bose-cluster size k of the density of k-cycles should diverge at T_c, which in turn implies that some critical action S^* required to permute two particles should be reached. He justified this idea for an ideal gas, and in Ref. [108], it was extended to interacting systems such as liquid ^{4}He.

Expanding these contributions,

$$\begin{aligned} z_k(T) &= \int \mathrm{d}y_1..\mathrm{d}y_k \left\langle y_2,y_3,...,y_k,y_1|e^{-\beta\hat{H}}|y_1,y_2,...,y_k\right|\left.y_2,y_3,...,y_k,y_1|e^{-\beta\hat{H}}|y_1,y_2,...,y_k\right\rangle \\ &= \int \mathrm{d}y_1 \left\langle y_1|e^{-k\beta\hat{H}}|y_1\right|\left.y_1|e^{-k\beta\hat{H}}|y_1\right\rangle \equiv z_1(T/k)\,. \end{aligned} \tag{3.13}$$

The partition function for a non-relativistic free particle in a box is well known, so we can get the full contribution

$$z_k(T) = \frac{V}{\lambda_B^3 k^{3/2}}\,, \tag{3.14}$$

where λ_B is the thermal de Broglie wavelength and V is the volume of the box. Then the partition function is

$$Z = \frac{1}{N!} \sum_P \sum_k \left(\frac{V}{\lambda_B^3 k^{3/2}} \right)^{n_k} . \tag{3.15}$$

This quantity is not easily computed for fixed particle number, but this problem is avoided if we go to the Grand Canonical ensemble, for which the partition function is

$$\mathcal{Z} = \prod_k \left(\frac{V e^{\mu k/T}}{\lambda_B^3 k^{5/2}} \right) . \tag{3.16}$$

From this partition function, we can extract the density of k-cycles

$$\rho_k(T) \equiv \frac{\langle n_k | n_k \rangle}{V} = \frac{e^{\mu k/T}}{\lambda_B^3 k^{5/2}} . \tag{3.17}$$

The total particle density is

$$\frac{N}{V} = \sum_k k \rho_k(T) = \sum_k \frac{e^{\mu k/T}}{\lambda_B^3 k^{5/2}} , \tag{3.18}$$

which has an upper limit of $\mu = 0$. This approach is fully valid for any non-interacting gas above T_c (i.e. with k-cycles on the microscopic scale). Therefore, by measuring numerically the densities ρ_k at various temperatures of a given system, we can fit a curve of the function above to find a temperature at which the quantity μ/T vanishes; this value will be the critical temperature, T_c, for Bose-Einstein condensation (BEC).

In this work, as was studied in Refs. [64, 65], we are *not* dealing with a non-interacting gas of particles, for which the approach above is exact. Nevertheless, we expect the densities of cycles to decrease exponentially with k

$$\rho_k(T) = e^{-\hat{\mu} k} f(k) , \tag{3.19}$$

where $\hat{\mu} = -\mu/T$ and $f(k)$ is some decreasing function of k of the form $f(k) \sim 1/k^\alpha$. To find the critical temperature, we look for the temperature the k-cycles are no longer suppressed exponentially in k, i.e. $\hat{\mu} \to 0$.

3.1.3 Method 3: Machine Learning

With recent advances in computational power, machine learning algorithms are a fantastic way to make predictions of outcomes given a set of inputs. These methods "train" the computer on datasets with known outcomes, allowing the computer to tweak its classification scheme such that a majority of input data points yield the correct output. After a classification scheme is created, one can feed "new" data to the algorithm and obtain its predicted classification.

3.2 Applications of PIMC

The numerical simulations were carried out using a PIMC code written in C++, and the analysis of the output data was done in Python and Mathematica. The algorithm for the PIMC code was the traditional algorithm, with structures and Monte Carlo moves as outlined in Ref. [76]. We implemented the worm algorithm, [78], which was used for simulations of He^4 and small values of the Coulomb coupling, but for large values of coupling, we ran into problems with the acceptances of either the removal or insertion of particles into the system, so we were forced to revert to the traditional algorithm. Internal energy – kinetic and potential – was found using the primitive and virial estimators, both summarized in Ref. [76], and worked out in detail in Ref. [77].

For the each simulation case – particle number, temperature, and coupling – we ran three trials collecting 10000 Monte Carlo configurations post-equilibration, the data from which was then binned and analyzed by a Python script. Error on the raw data was computed using the Jackknife sampling method [109]. The fits for the data and errors on the fits were computed using Mathematica's `NonlinearModelFit`.

3.2.1 Liquid He^4

The first task was to reproduce well-quantified results using the permutation-cycle critical temperature analysis, in order to ensure the validity and applicability of this method. To do so, we simulated a box of 128 ^{4}He particles interacting via the empirical Aziz potential [110], and compared our results to the experimental results as well as previous computational results [76]. The experimental result for the BEC critical temperature was found to be 2.17 K, while the calculations with the binary Aziz potential, shown in in Fig. 3.1, predict a critical temperature of 2.19 K.

In order to compute the critical temperature using the permutation-cycle method, we first determine the temperature dependence of the probability of finding a particle in a k-cycle $P_k(T)$. From these probabilities, we compute the permutation-cycle densities, $\rho_k(T)$,

$$\rho_k(T) = \frac{N P_k(T)}{kV}\,, \tag{3.20}$$

where N is the number of particles in the system, V is the volume.

The permutation-cycle densities for various temperatures are shown in Fig. 3.2. We can then fit these densities via Eq. (3.19) to extract the suppression factor, $\hat{\mu}$. A few of these fitted curves are shown in Fig. 3.2(a). At $T = 2$ K – below T_c – the exponential suppression is not present, and thus observe permutation cycles with $k > 30$. This is a sign that at this temperature in an infinite system, there will be a cluster of infinitely many particles; the Bose condensate is present. In Fig. 3.2(b), one can see explicitly how the exponential suppression appears at $T > 2.2$ K, visually portrayed by the gap between the 2.2 K and 2.3 K lines. Above T_c, the suppression factor grows larger with temperature.

Finally, after fitting all of the temperatures and finding $\hat{\mu}(T)$, we fit the $\hat{\mu}$ data with the functional form,

$$\hat{\mu}(T) = A(T - T_c)^{\nu}\,, \tag{3.21}$$

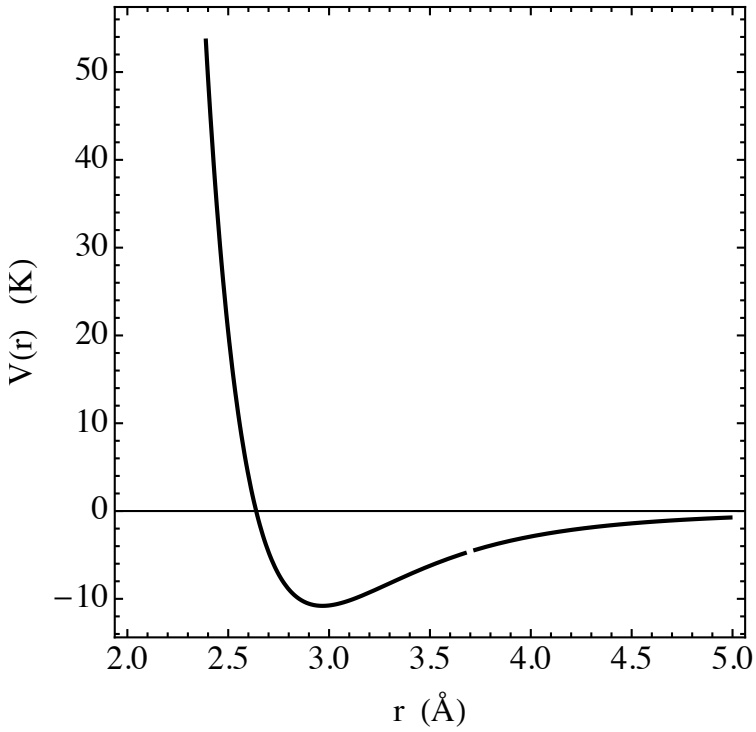

Figure 3.1: The empirical two-body potential for liquid ^{4}He, using parameters from Ref. [110].

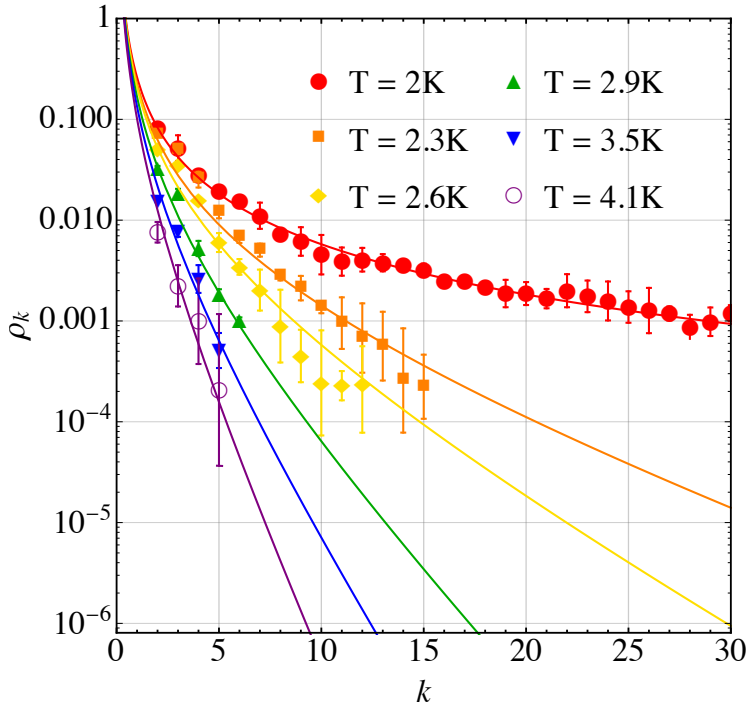

(a)

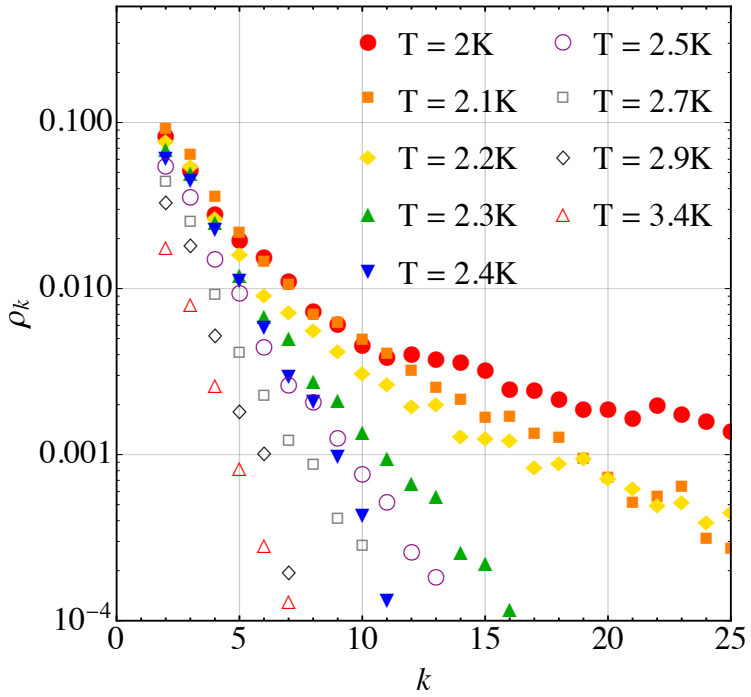

(b)

Figure 3.2: The permutation cycle densities ρ_k at various temperatures for a system of 128 ^{4}He particles. Fig. (a) shows a wider range of temperatures. The lines are rough fits to guide the eye. (b) focuses on temperatures near the critical value (neglecting error bars for clarity). Note the gap between the 2.2K and 2.3K points.

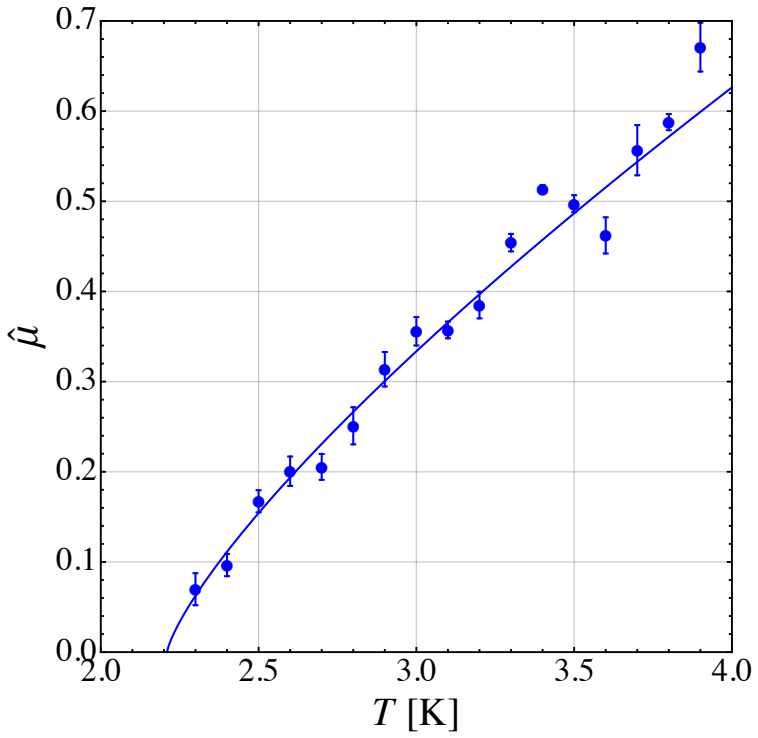

Figure 3.3: The exponential suppression of k-cycles as a function of temperature for the ^{4}He system. The vanishing of the effective chemical potential $\hat{\mu}$ indicates the BEC critical temperature T_c.

from which we find T_c. The results of our simulations are seen in Fig. 3.3. Using the permutation-cycle method, we find a critical temperature of 2.21±0.04 K. This result is within 2% of reproducing the experimental critical temperature of the ^{4}He system and within 1% of the critical temperature determined for the Aziz potential used in other numerical calculations. We conclude that this method can indeed be used in path-integral Monte Carlo to accurately find the critical temperature of interacting Bose systems.

3.2.2 One- and Two-Component Coulomb Gases

According to Einstein, the BEC of an ideal Bose gas happens at the critical temperature,

$$T_c = \left(\frac{2\pi\hbar^2}{mk_B}\right)\left(\frac{n}{\zeta\left(\frac{3}{2}\right)}\right)^{\frac{2}{3}}. \tag{3.22}$$

where n is the density and m is the particle mass.

Extension of this relation to interacting Bose gases has an interesting history. There was much debate in the literature – using Hartree-Fock, loop diagram, and renormalization group calculations, for example – about even the sign of corrections to T_c; see Ref. [111] for discussion and references.

Numerically, the dependence of BEC critical temperature on the strength of a hard sphere potential was studied by Grüter, et al. [111]. It was found that at low densities the critical temperature is increased by a repulsive interaction, while at high densities the critical temperature is decreased, eventually recovering the well known ^{4}He result. Their results are shown in Fig. 3.4. This behavior at low densities can be explained with the calculation by Holzmann, et al. [112].

As a first step in making an effective model for a quantum two-component Coulomb Bose gas, we seek to find the dependence of T_c on the Coulomb interaction strength; i.e., by varying α in

$$V_{\text{int}}(r_{ij}) = \alpha\frac{q_i q_j}{r_{ij}}. \tag{3.23}$$

In our numerical study, the magnitude of charges, q; the masses, m; $\hbar$; Boltzmann's constant, k_b; and the density, n, are all scaled to 1. This leaves as variables only the temperature, T, entering via the period of the Euclidean time $\tau \in [0, 1/T]$, the magnitude of the Coulomb coupling, α, and the signs of the charges. In these units, the critical temperature for the ideal Bose gas is

$$T_0 = 2\pi\left(\frac{1}{\zeta\left(\frac{3}{2}\right)}\right)^{\frac{2}{3}} = 3.3125\,. \tag{3.24}$$

and this value will be indicated by a horizontal dashed line in the plots to follow.

The Coulomb simulations were carried out for 8, 16, 32, and 64 particles, for both the one- and two-component cases. For each simulation, there were 32 imaginary time-slices. For the one-component simulations, we tested temperatures (in our units) from 1.6 to 5.1, in intervals of 0.1, while for the two-component cases, we looked at temperatures in the range of 0.4 to 5.1 in intervals of 0.1, and the range of 6 through 9 in intervals of 1.

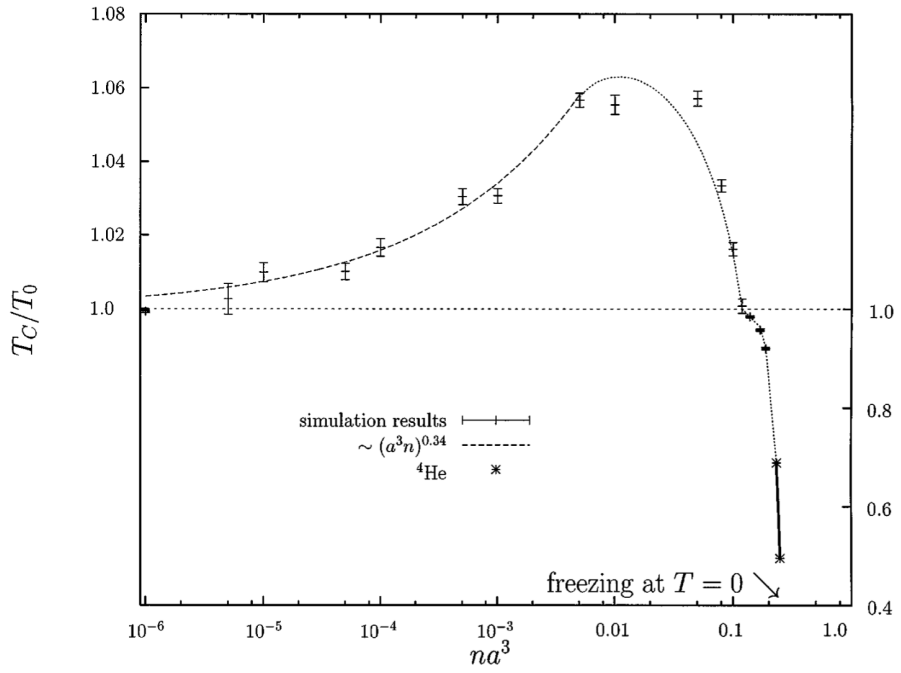

Figure 3.4: The critical temperature of a system of hard spheres as a function of their density. From Ref. [111].

For the one-component Coulomb Bose gas, with compensating distributed charge commonly known as *jellium*, we seek to investigate the dependence of T_c on the strength of the Coulomb coupling parameter, and compare, qualitatively, it to the relation in the hard-sphere case.

The results of our simulations are shown in Fig. 3.5. The first thing to note is that the two methods used produce results consistent within the statistical errors. Note further that we find the same behavior at small values of the coupling as in the case of low-density hard spheres [111]; the critical temperature for the BEC phase transition *grows*. Yet if the coupling becomes large enough, T_c rapidly drops below the critical temperature for an ideal Bose gas. Eventually, as the particles are "too repulsive," the BEC phenomenon becomes impossible since it becomes essentially "too costly" in terms of the action to permute them.

Let us also note that, while the permutation-cycle method agrees well with the older finite-size scaling method, the requirements for the system size to yield comparable results are different. The finite-size scaling method can give decent results even using two systems, of only 8 and 16 particles, while the permutation cycle method required many runs of at least 32 particles. Therefore, at least in the case of long-range forces, which take a large amount of CPU time to compute, the finite-size scaling method may be more practical. If one, however, is looking at other quantities that require larger system sizes to begin with – such as the superfluid fraction itself (and not just how it scales with system size) – the permutation cycles method is an easy way of determining T_c with data already gathered from those larger system simulations.

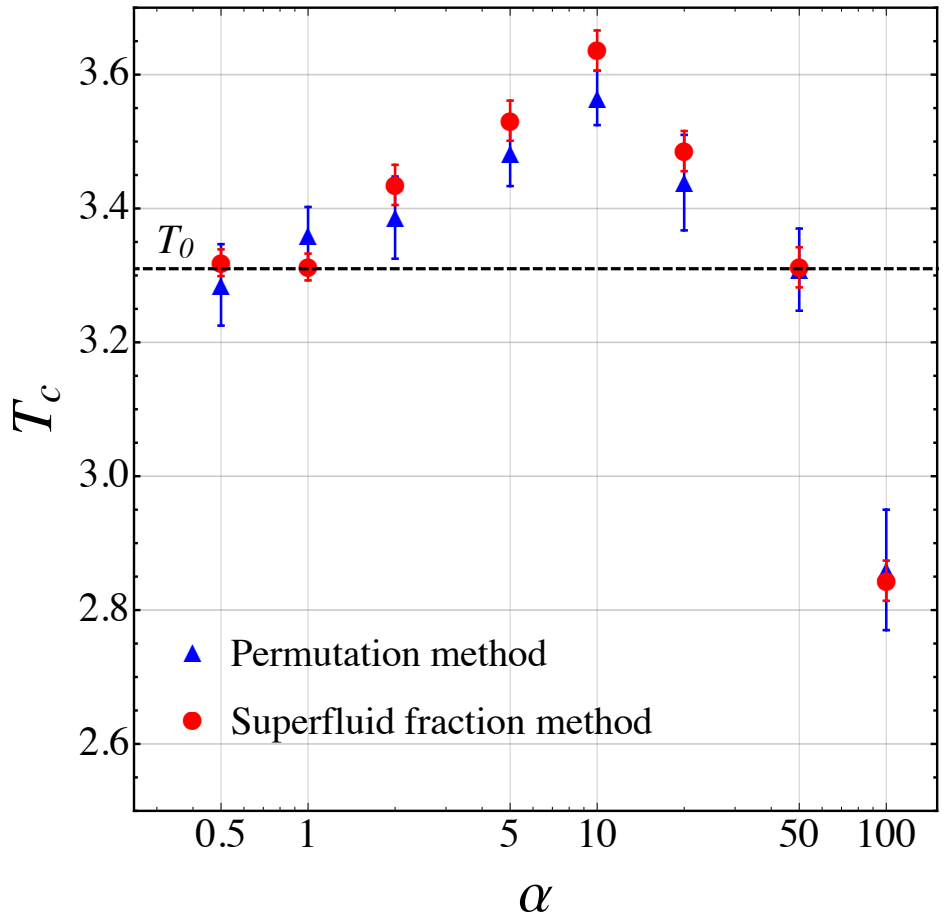

Figure 3.5: The critical temperature for the BEC phase transition as a function of the coupling, α. The red circles are the results of the finite-size scaling superfluid fraction calculation for systems of 8, 16, and 32 particles; and the blue triangles are the results of the permutation-cycle calculation for a system with 32 particles. The black dashed line denotes the Einstein ideal Bose gas critical temperature, T_0.

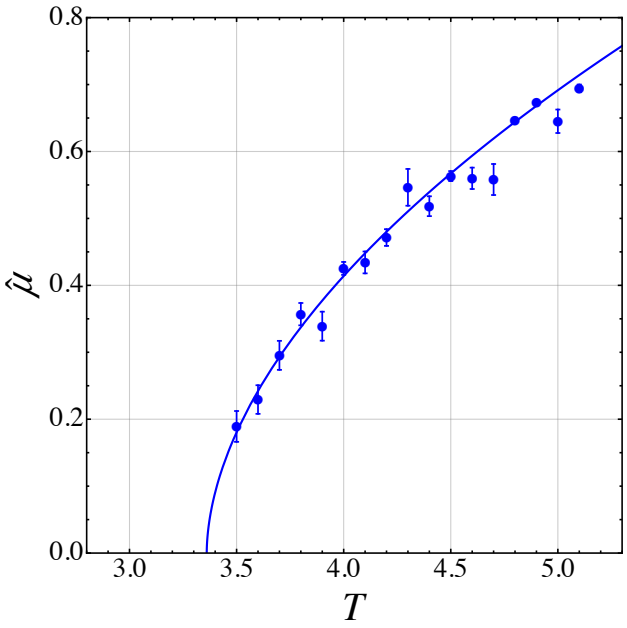

Figure 3.6: The results of the permutation-cycle calculation for a system with 32 particles at $\alpha = 1$ along with a fitted curve. The vanishing of the effective chemical potential $\hat{\mu}$ indicates the critical temperature T_c.

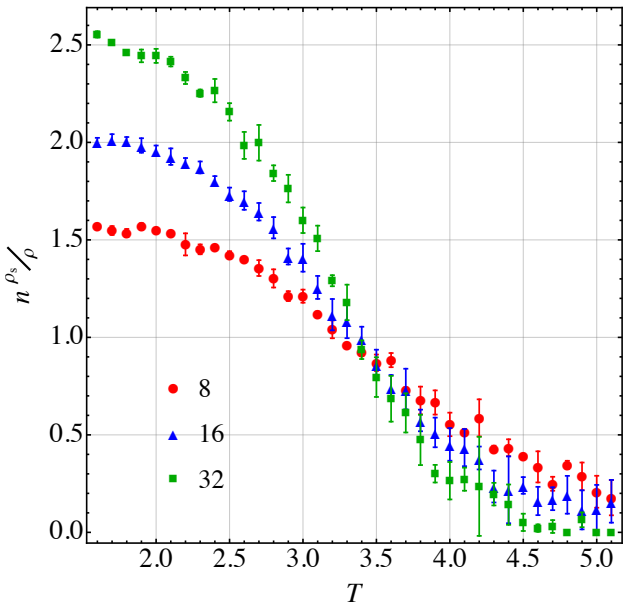

Figure 3.7: The results of the finite-size scaling of the superfluid fraction calculation for 8 (red circles), 16 (blue triangles), and 32 (green squares) particles at $\alpha = 5$. The point where the data sets intersect is the critical temperature T_c.

α	Permutation	Superfluid	Machine Learning
0	3.313	3.313	–
1	3.358	3.312	3.33
2	3.379	3.342	3.383
5	3.472	3.520	3.493
10	3.552	3.632	3.597
20	3.446	3.481	3.489
50	3.313	3.313	3.312

Table 3.1: Machine learning model results for the critical temperature compared to the permutation cycles and superfluid fraction methods, for various couplings α of a one-component Coulomb Base gas. Errors are visible in Fig. 3.5, and are .005 for the machine learning model results.

Examples of the analysis methods are shown in Figs. 3.6 and 3.7. In Fig. 3.6, we see the $\hat{\mu}$ data for the 32 particle system at $\alpha = 1$, which were obtained by fitting the permutation cycles as explained above. The $\hat{\mu}$ data is then fitted to find $T_{\rm c}$, which is where the solid fitted curve intersects the x-axis. In Fig. 3.7, we see the superfluid fraction data for three system sizes at $\alpha = 5$. The data is linearly fit around the intersection point, as described above.

For the machine learning algorithm, we will train the computer on a dataset from the free, ideal Bose gas, giving it the data on permutations and winding from path configurations. The model chosen was the Support Vector Machine (SVM) classifier [113], which effectively projects an n-dimensional dataset into an $n + m$-dimensional space, and finds a best-fit hyperplane that divides the data based on its final classification; in our case, the classification will be whether the path configuration is for a system above or below T_c.

We use a simulation of 32 free bosons, which is not computationally taxing, and for which we know the exact critical temperature ($T = 3.3125$ from the Einstein formula for $\rho = 1$ and $m = 1$). The preprocessing of the data uses the principle of Jackknife sampling [109], and takes sets of 200 path configurations, averages them, and outputs the permutation and winding statistics for each ensemble of configurations. These are the data used to train the models.

The input data given to the algorithm is shown in Fig. 3.8; this is distribution of below T_c (blue) and above T_c (red) ensemble averaged data projected onto the space of permutations cycles. For example, in the second plot in the first row, the ensembles are plotted as a function of percentage of particles in 2-cycles vs percentage of particles in 3-cycles (denoted (2,3) on the plot), with the color of the point dictating whether that particular ensemble was above or below T_c. We can see that some pairs of permutation probabilities display a sharp separation in critical temperature. The resulting SVM classifier model was cross validated to mean average error (MAE) of $\sim .005$.

We only used the algorithm for the one-component gas, for which the results as shown in Table. 3.1. We find that the algorithm falls within error of the other two methods for finding T_c.

Following the one-component Coulomb Bose gas, we carried out the PIMC simulations and analysis for a neutral system of particles with two different charges, $+1$ and -1, with

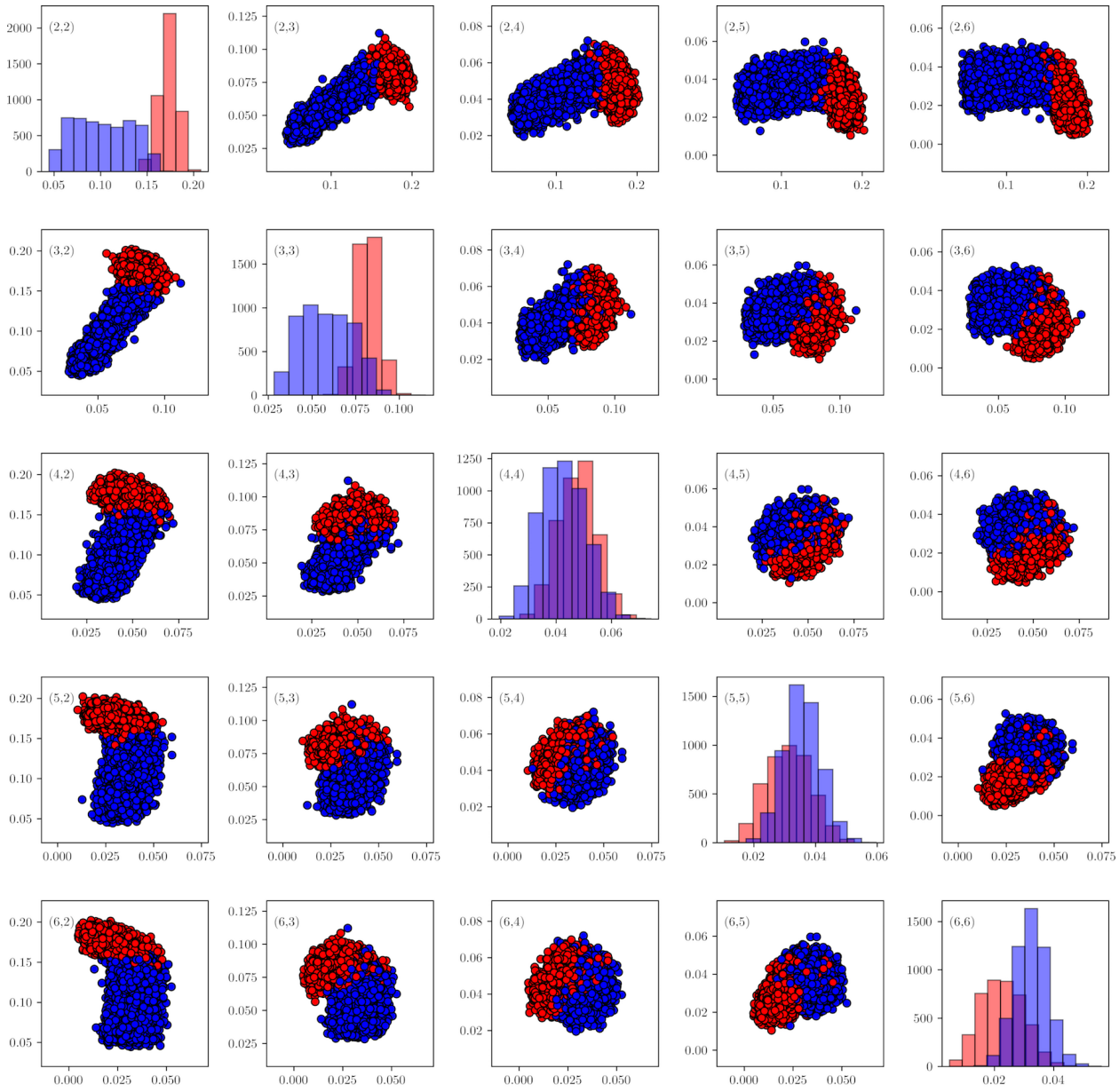

Figure 3.8: Visualization of the input data for a free Bose gas for the machine learning model. Each point represents an average of 200 configurations, the color indicates whether the configurations are from a system above (red) or below (blue) T_c, and quantities on the axes are the percentage of particles in a k-cycle. The plots on the diagonals are the distributions of configurations of the systems for each k-cycle, from 2 through 6. The off-diagonal plots show the distributions of k-cycles vs. k'-cycles.

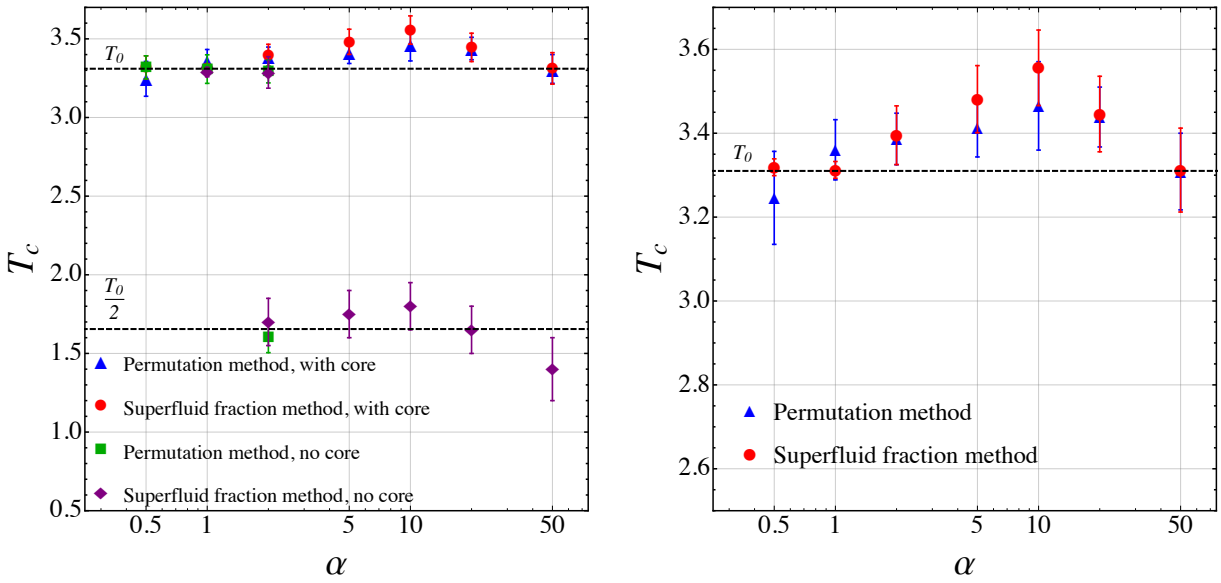

Figure 3.9: The critical temperature for the BEC phase transition for the two-component Bose gas as a function of the coupling, α. (a) The red circles and the blue triangles are the results of the finite-size scaling superfluid fraction calculation and the permutation-cycle calculation, respectively, for systems without core repulsion.. The purple diamonds and green squares are the results of the finite-size scaling superfluid fraction calculation and the permutation cycle calculation, respectively, for systems with core repulsion. The black dashed lines denote the Einstein ideal Bose gas critical temperature for a particle of mass $m = 1$, T_0, and for a particle of mass $m = 2$, $T_0/2$. (b) A zoom-in of the results in (a) for systems with core repulsion.

and without repulsive core; the results are shown in Fig. 3.9.

At very small couplings with and without core repulsion, the behavior of the critical temperature is very similar to that of the one-component case; the particles are only slightly interacting and therefore have a critical temperature very close to that of an ideal gas. When the coupling increases, however, the point-like (without core) two-component gas has a split in critical temperature, which acts like the one-component case for some particles, and drops much more quickly than that of the one-component case for others to approximately $T_0/2$, which is the ideal gas condensation temperature for particles with mass $m = 2$, i.e., a neutral molecule comprised of particles with two opposite charges.

The finite-size (with core) two-component gas, seen more clearly in Fig. 3.9(b), does not form these molecules and thus has the behavior of the one-component gas. It is important to note that even with a second component added, the finite-size particles have the *same* critical temperature behavior as a one-component gas: a 5-10% deviation upward before dropping at very strong couplings.

At extremely high couplings, the critical temperature drops for both cases. We do not have the accuracy in our data to confidently state whether the molecular phase has the same rising T_c at lower couplings that is seen in the one-component case.

The data seen in Fig. 3.9 for the case of point-like particles is from both the permutation cycle method and the finite-size scaling method for small couplings, but only finite-size scaling method for larger couplings, as there was too much statistical noise in the permutation statistics to obtain a good fit for a critical temperature. This may be remedied by a larger sample size or a larger system size, as the particles at higher coupling tend to become "stuck" if they enter the molecule phase. We do not have this problem when the particles are given a repulsive core.

One of the key observables we can use when comparing our results to the lattice monopole results is the spatial correlations of particles. In our simulations, we keep track of the Euclidean-time paths of individual particles, allowing us to observe their distributions in relative distance r as a function of coupling strength and temperature. We define the pair correlation, $g(r)$, to satisfy

$$n(r) = 4\pi\rho \int_0^r g(r')r'^2 dr' \,, \tag{3.25}$$

where $n(r)$ is the number of particles found between 0 and r, and $\rho = N/V$ is the overall density of particles in the volume; $g(r)$ is, by definition, normalized to distribution of an ideal gas. In this work, for cases in which we have two components, we denote the same charge correlation with $g_{++}(r)$ and the opposite charge correlation with $g_{+-}(r)$.

Fig. 3.10 shows a sampling the radial correlations of the one-component Bose gas at different temperatures at couplings $\alpha = 1$, 5, 10, 20, 50, and 100.

We find that at weak couplings, $\alpha < 2$, the correlation functions flattened out as the temperature increased; this is caused by the fact that the thermal energy is greater than the potential repulsion in these cases. The slight increase in the correlation function near $r = 0$ is caused mostly by statistical fluctuations, but also in part by the fact that we are observing a jellium system with a neutralizing smeared background charge. At couplings $\alpha \geq 10$, the variations of temperature – in the range we probed (0.5 T_c to 1.8 T_c) are not reflected in the correlation functions. As the coupling is increased the correlation functions show signs

of structure, particularly at $\alpha \geq 20$.

Fig. 3.11 shows the radial correlations of the for the two-component gas with no core at different temperatures at couplings $\alpha = 0.5$, 1, 2, and 5. Without any core repulsions, at couplings $\alpha \geq 5$, the particles form small bound states; the particles essentially make point-like dipoles, especially at $T > T_c$. This is seen from the same-charge correlator being equal to the opposite-charge correlator at distances $r \geq 0.1$. An interesting feature seen in Fig. 3.11 is that both the anti-charge and same-charge correlations increase – both in overall range as well as in magnitude at short range – as T approaches T_c from below and then subsequently fall as temperature is increased further. The maximum short-range correlations occur slightly under T_c for small couplings $\alpha \sim 1$, and move further above T_c for larger couplings.

Figs. 3.12 and 3.13 show the radial correlations of the for the two-component gas with a repulsive core at different temperatures at couplings $\alpha = 0.5$, 1, 5, and 10. At low temperatures, $T < T_c/3$, the probability for there to be two oppositely charged particles in a bound state is large even at small couplings $\alpha < 1$; at larger couplings, we find bound states at higher temperatures. At $\alpha \sim \mathcal{O}(10)$ and larger, at low temperatures, we see the same screening phenomenon we saw when there was no repulsive core; the molecule acts as a neutral dipole, which causes the same-charge correlator (Fig. 3.13, bottom right panel) to be *greater* than unity.

Fig. 3.14 shows the internal energy per particle of the two component gas with a core, in units of the temperature, across various temperatures and couplings. Let us remind the reader that in the 2-body Coulomb problem, the virial theorem tells us that mean potential energy is $-1/2$ times the mean kinetic energy, so the total energy is positive. Many-body strong coupling problems, on the other hand, can create crystal-like correlations between many particles, producing larger potential energy, and thus negative total energy.

The temperature dependence of the energy is similar for all couplings, and, at fixed temperature, the energy scales roughly linear with temperature. At high temperatures, the kinetic energy begins to scale at $3/2T$, as predicted by classical statistical mechanics. One can see that, at high coupling, the energy falls rapidly as temperature is decreased to near zero, which reflects the increasing binding of the oppositely charged particles.

3.3 Parameters for SU(2) Monopole Ensembles

Classical studies of the magnetic scenario in QGP proposed that the magnetic component of the plasma acts as a liquid with Coulomb-like fields [67, 114], and contemporary studies on the lattice, e.g Refs. [115, 64], furthered the study of monopoles in QCD-like theories. These studies on the lattice [115] found that the monopole density at $T > T_c$ can be well approximated by

$$\rho_m(T) \sim \frac{T^3}{\log T^2} \,. \tag{3.26}$$

Unlike the "electric" particles, quarks and gluons, the density of monopoles is not vanishing at T_c due to confinement, but instead has a *peak* there. It also follows from the correlation function analysis that the magnetic coupling becomes stronger as temperature increases [114].

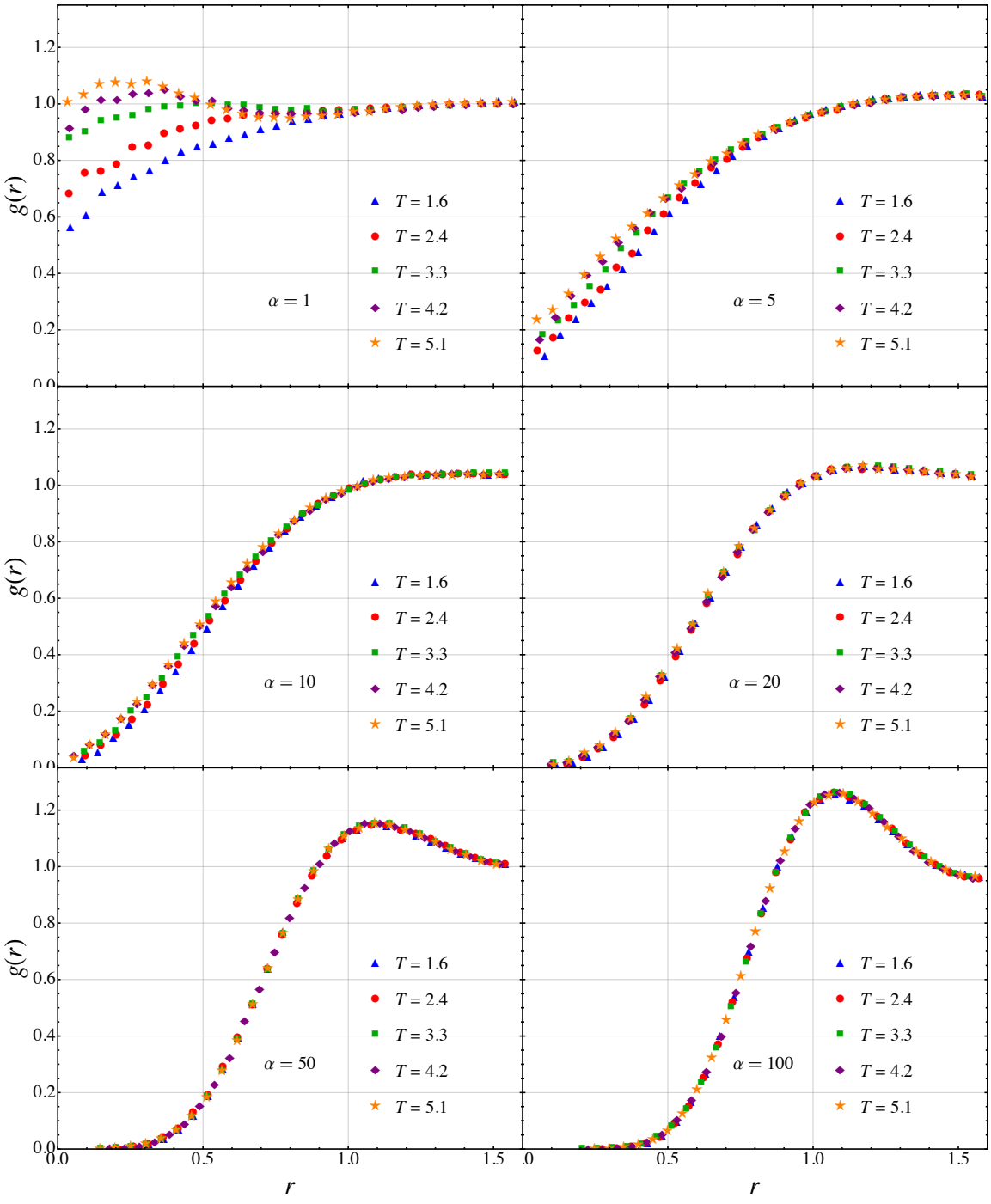

Figure 3.10: Spatial correlations of the one-component Bose gas, at different temperatures and coupling strengths.

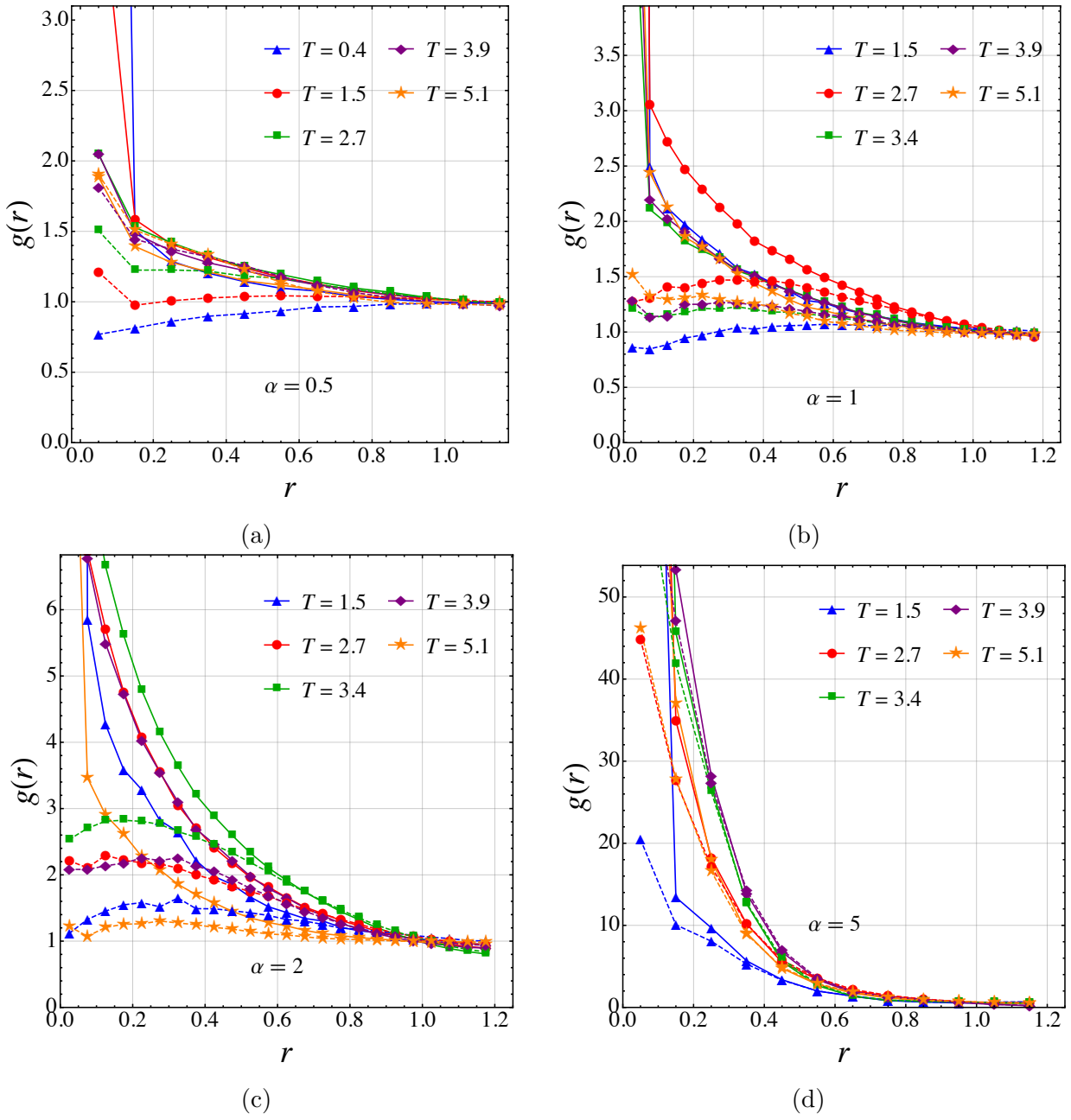

Figure 3.11: Spatial correlations of the two-component Coulomb Bose gas (without core), at different temperatures and coupling strengths. Note that most plots have *two* correlation functions for each temperature, one "attractive", for opposite sign charges $g_{+-}(r)$ (solid lines) and one "repulsive", the same sign charges $g_{++}(r)$ (dashed lines). Note that at strong coupling, $\alpha \sim 5$, these two correlators overlap significantly.

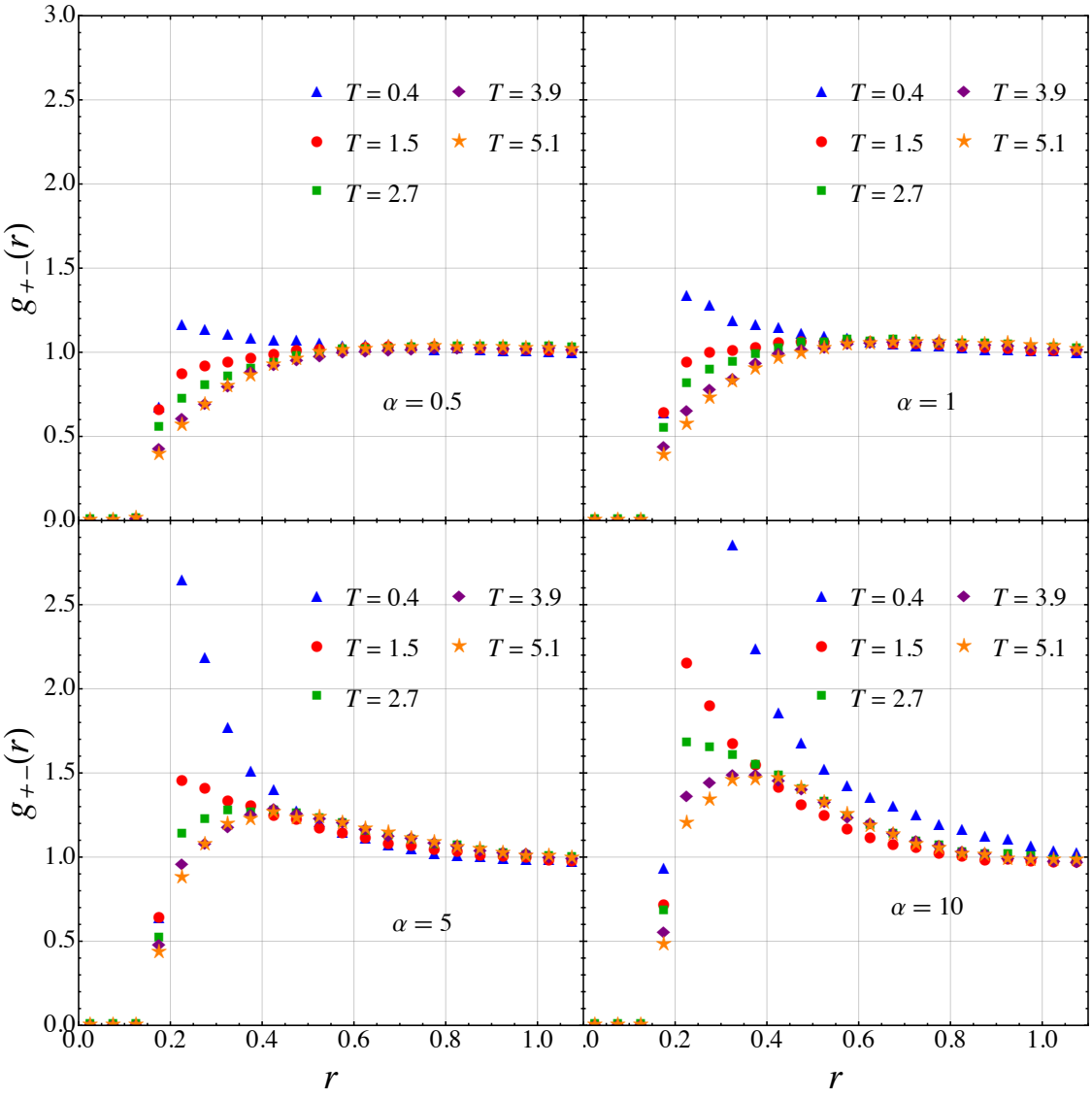

Figure 3.12: Spatial correlations of the two-component Bose gas with core repulsion for particles of opposite charge, at different temperatures and coupling strengths.

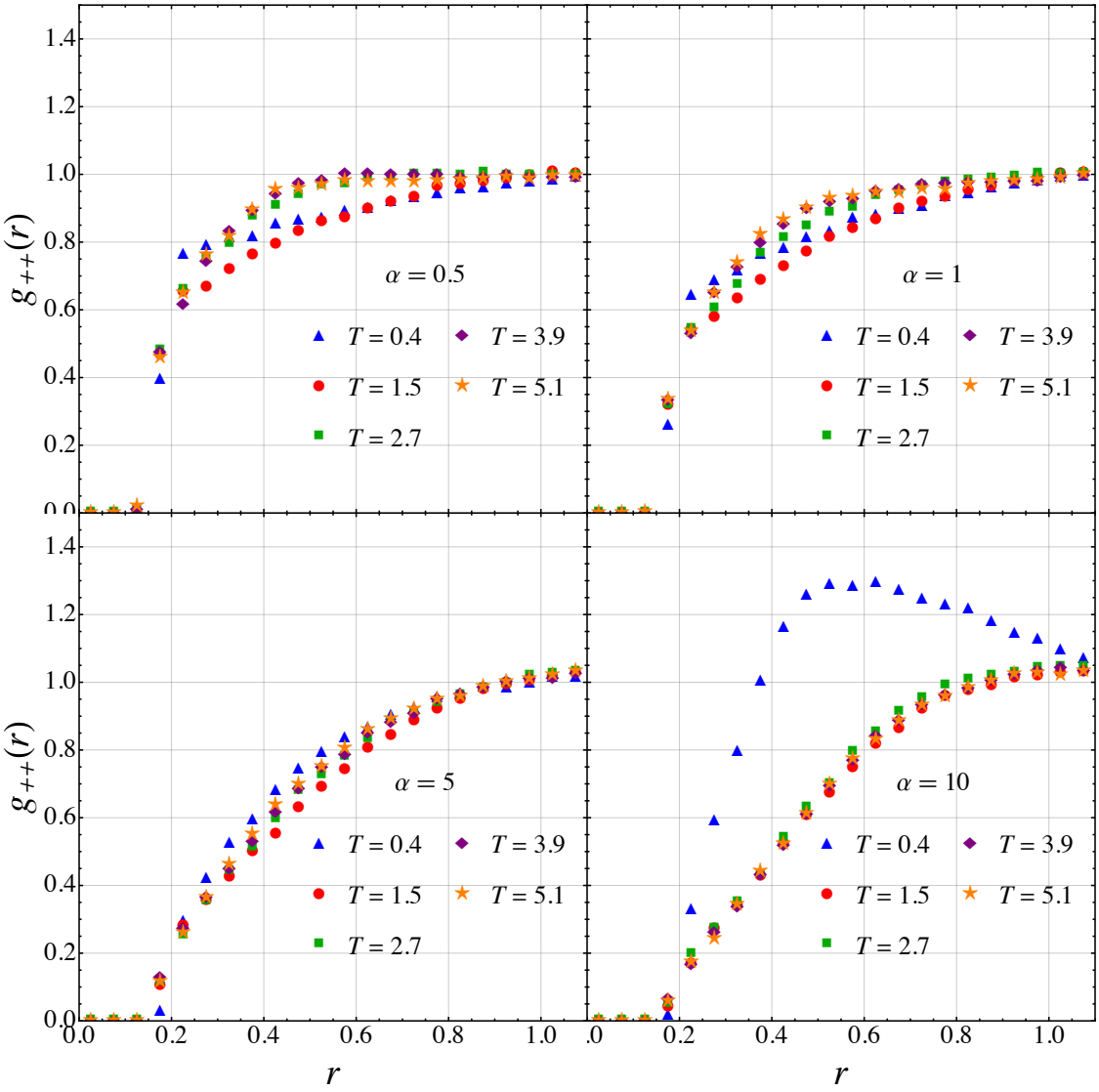

Figure 3.13: Spatial correlations of the two-component Bose gas with core repulsion for particles of the same charges, at different temperatures and coupling strengths.

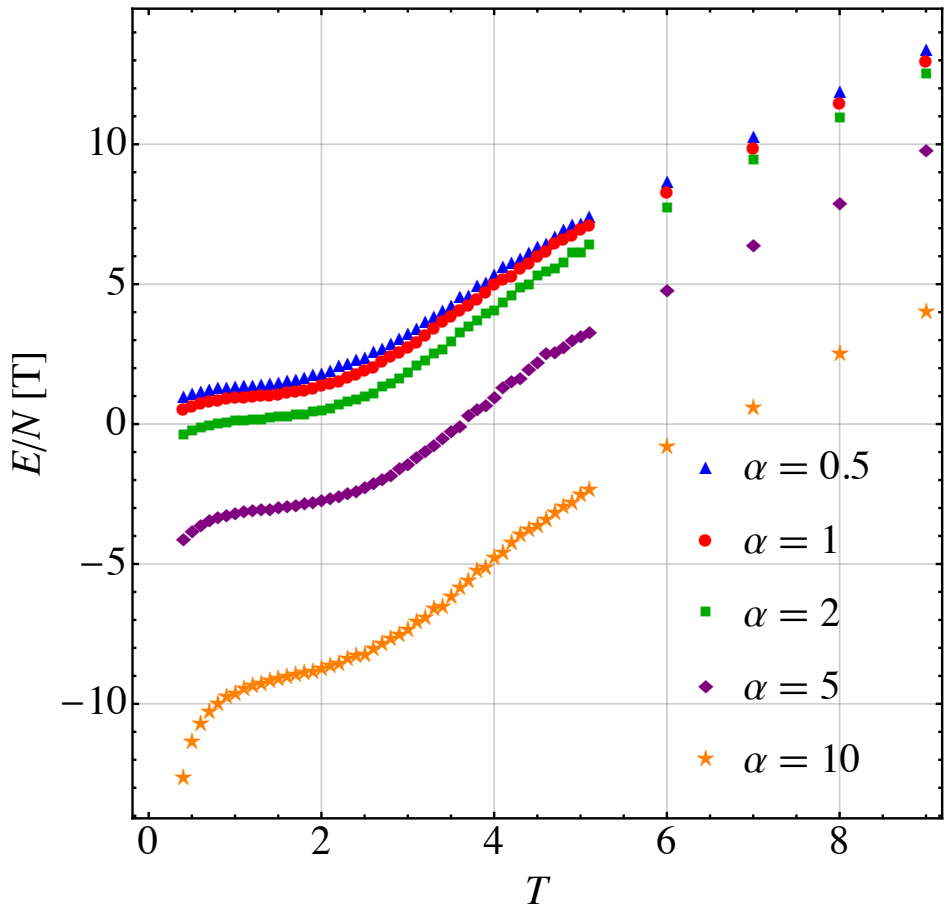

Figure 3.14: Internal energy per particle of the two-component Coulomb Bose gas with a repulsive core, for various couplings and temperatures. Error bars are smaller than the points themselves.

Based on these findings, we would like to make an effective model of quantum monopoles that reproduces the behavior of those on the lattice, without the many degrees of freedom of a full QCD-like theory.

Before we dig out into details of the matching procedure, let us outline its general meaning. The simulated Coulomb Bose gas model has several parameters, such as the density n, the temperature T, the Coulomb coupling α, and the particle mass m. The monopole ensemble corresponding to the finite temperature QCD has only one input variable, T, and thus only simulations on a particular parametric line $n(T), \alpha(T), m(T)$ in the general parameter space are directly relevant for our physics application.

Now that we have quantified the behavior and thermodynamics of an isolated two-component Coulomb Bose system, our first goal is to find the parameters for our model that are necessary to effectively model magnetic monopoles in QCD-like theories at various temperatures above the critical temperature. To fit our findings to physical results, we first compare our correlation functions with those of Ref. [115], found on the lattice. We note that this lattice calculation was done in pure-gauge SU(2), which yields one U(1) monopole species.

The lattice correlations and the matching correlation functions from our simulations are seen in Fig. 3.15. We match these two sets of correlation functions by scaling our interparticle distance to that given by the monopole density in Ref. [115], and then by finding the simulation coupling strength that produces the same magnitude and long-range correlation behavior seen on the lattice.

First and foremost, we see that a two-component Coulomb Bose system reproduces the same types of correlations seen on the lattice, as was found in Ref. [114], giving further credence that our model can effectively describe the behavior of magnetic monopoles in QCD-like theories. The mapping of our results to those on the lattice is given by

$$\alpha(T) \approx 3.4\, \rho_m^{1/3}(T)\,, \tag{3.27}$$

where $\alpha(T)$ the coupling used in our simulation, $\rho_m(T)$ the monopole density (in fm^{-3}) found in Ref. [115], and T in units of the critical temperature. One unit of length in our simulations is equivalent to $\rho_m^{-1/3}(T)$, the interparticle spacing (in fm) found on the lattice. This result was checked in and holds throughout the range 1.1-4T_c; it may be applicable at higher temperatures as well. The constant 3.4 is comes from the factor of $(T_\mathrm{c})^3$, which sets the scale of the density in dimensionless units.

If this relation holds to T_c, we can map the physical value of the critical temperature to our units: 296 MeV (T_c in the SU(2) lattice simulation [115]) is the critical temperature of the two-component gas with coupling $\alpha \approx 4.2$ – approximately 3.45 in our units. We found that a two-component Coulomb Bose gas with $\alpha \approx 4.2$ has a 5-10% higher critical temperature than the free gas; the critical temperature of a free gas of monopoles would then roughly correspond to 280 MeV. Extrapolating the monopole density from Ref. [115] to T_c, setting T_c to 280 MeV, and solving for mass in Einstein's equation, we find that

$$280\ \mathrm{MeV} = \left(\frac{2\pi}{m}\right)\left(\frac{(240\ \mathrm{MeV})^3}{\zeta\left(\frac{3}{2}\right)}\right)^{\frac{2}{3}} \rightarrow m \approx 680\ \mathrm{MeV}\,, \tag{3.28}$$

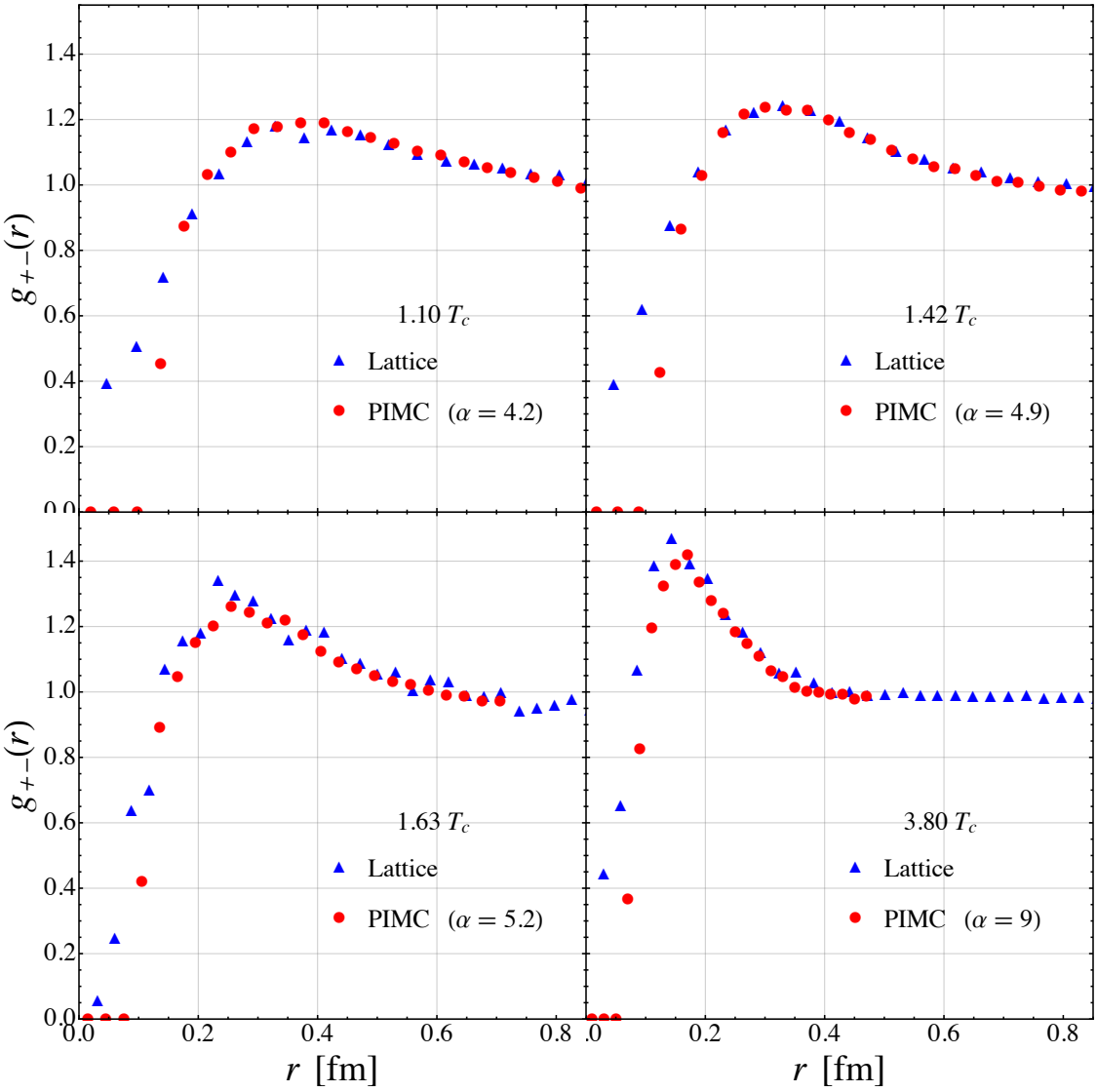

Figure 3.15: Spatial correlations from our simulations (red circles) matched via scaling to lattice correlations (blue triangles) from Ref. [115] at various temperatures.

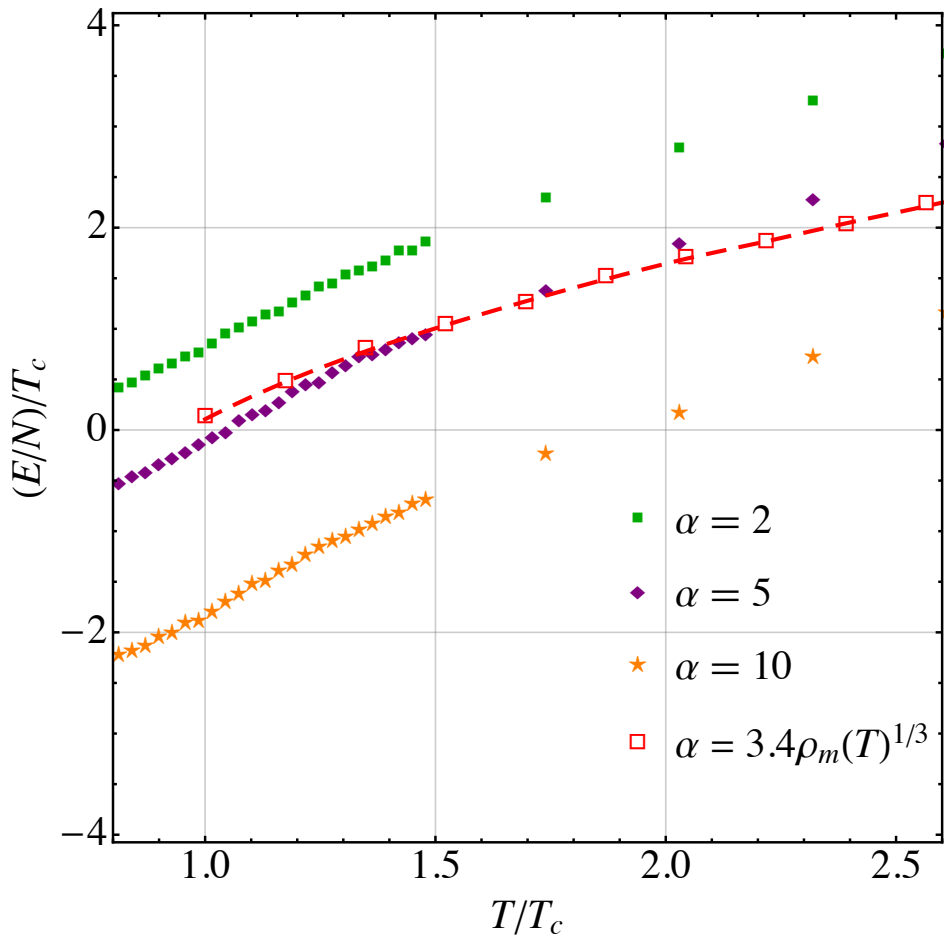

Figure 3.16: The energy per particle along the physical line defined by the parameters which match simulation correlation functions to the lattice, shown alongside previously shown two-component Coulomb simulations (Fig. 3.14) at fixed couplings. The dashed line is to guide the eye.

which is approximately the estimate of the monopole mass from Ref. [64], though it is larger than that from Ref. [108].

3.4 Thermodynamics of QCD Monopoles

After the parameters of our model were matched to those in the pure-gauge $SU(2)$ lattice simulations, we can directly evaluate the contribution of the monopoles to the thermodynamics of that theory.

The thermodynamics on the *physical line*, i.e. the trajectory in parameter space as defined above, are shown in Figs. 3.16 and 3.17. In Fig. 3.16, we see the energy per particle along the physical line. At T_c, the internal energy of a monopole goes to approximately zero, and then grows as temperature rises. This growth is less than $^3/_2T$ because the coupling is increased with T, causing monopoles at large T to have a larger negative potential energy.

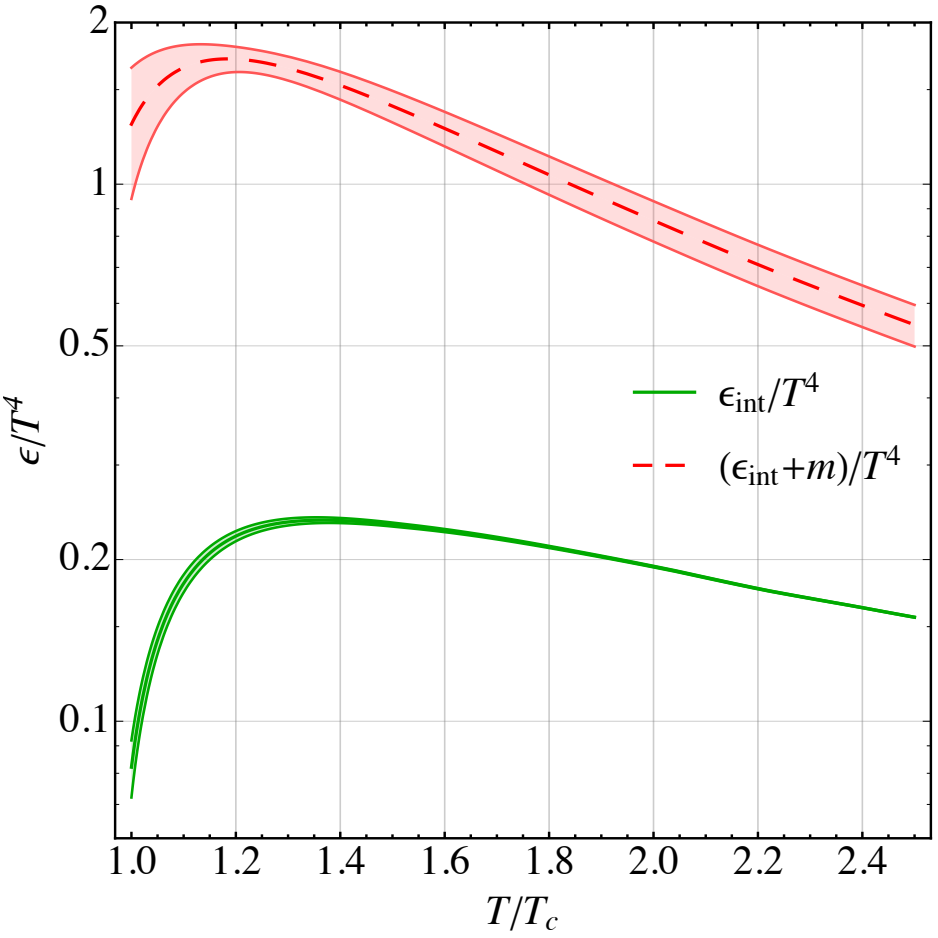

Figure 3.17: The dimensionless energy density for $SU(2)$ monopoles along the physical line defined by the parameters which match simulation correlation functions to the lattice. The lower line is the internal energy density (kinetic + potential) and the upper line includes the mass contribution.

This lower energy is, however, compensated by the $\sim T^3/(\log T)^2$ growth of the density of monopoles.

In Fig. 3.17, on the lower solid line, we see that the internal energy density of the monopoles ϵ/T^4 is maximal at approximately 1.3-1.4T_c. The contribution from the monopoles is relatively small, $\mathcal{O}(0.2)$.

In light of the fact that this contribution is close to zero, in addition to the internal energy (kinetic and potential), we must also take into account the mass of the particles, which has been extracted from the lattice in Ref. [64]. In Fig. 3.17, the upper dashed line shows the total energy density of the monopoles. The contribution from the monopoles, including the mass, is $\mathcal{O}(1.5)$.

QCD thermodynamical quantities are among the most basic properties of hadronic matter, and have been the focus of numerous lattice simulations for the last three decades. Due to growth of computational power and algorithm development, the results of these calculations have become rather accurate, and, over the last few years, have approached QCD with physical quark masses. We now know the pressure (free energy), energy, and entropy density as a function of the temperature: $p(T)$, $\epsilon(T)$, and $s(T)$, respectively.

At first glance, decomposing those functions into parts associated with certain quasiparticles – gluons, quarks, and perhaps monopoles – looks to be an impossible task, since all of them interact strongly. However, more recent studies have provided valuable insight, indicating that this task can perhaps be carried out.

The first step toward understanding of the role of monopoles in QCD is to move from the SU(2) to the SU(3) color group. This is far from trivial, since the latter has two diagonal color generators, and thus two "massless electrodynamics" surviving the breaking of the color group. Therefore, there are two distinct species of the monopoles. Including the antimonopoles, one would need to study a *four*-component Coulomb Bose gas. This system can be studied in the same way as for the one and two-component gases above, but was not done for this work. Note that two species of monopoles are not independent, as there should be attractive Coulomb forces between the monopoles of each U(1) electrodynamics, as well as repulsive forces between monopoles and anti-monopoles of different U(1) electrodynamics.

A comprehensive study of the condensation and density of lattice monopoles for the SU(3) color group has been done by Bonati and D'Elia [65]. As shown in Fig. 3 of that work, both monopole species happen to have nearly identical densities. Moreover, Fig. 2 and the corresponding text from Ref. [65] indicate that, for each of them, the density $\rho(T)$ is very close to that of the SU(2) monopoles; these densities effectively identical when taking into account the difference in T_c for the different SU(2) and SU(3) simulations. However, they have a slightly different fit from the SU(2) data at high $T > 2T_c$, namely

$$\rho_m(T) = \frac{3.66T^3}{\log(T/(0.163T_c))^3}\,. \tag{3.29}$$

This power of the logarithm matches predictions from the 1970s for finite-T QCD: the magnetic scale cubed $(g^2T)^3$.

The next step toward QCD would be to include quarks. The corresponding lattice simulations are unfortunately very expensive, especially for quarks as light as those in the real world. Only relatively recently have such lattice ensembles became available, and the anal-

ysis of their monopole content has not yet been done. Lacking simulation input, we will provide some speculation on "theoretical expectations."

Let us start from the high-T end, simply counting states. Gluons have two polarizations and N_c^2-1 colors, giving 16 bosonic states. Quarks contribute $2\cdot 2\cdot N_cN_f\cdot(7/8)$ (for $N_c=N_f=3$, $36\cdot(7/8)=31.5$) times the thermal energy of one bosonic state. Monopoles are charged spin-zero scalars, of $2(N_c-1)$ types (the number of diagonal generators multiplied by 2 to take into account the two charges), or 4 species for $N_c=3$. At high T they only exist at the so-called magnetic scale, and thus their density is additionally suppressed by a power of $\log(T)$, as discussed above. As a result, at high T, the monopole contribution is quite small as compared to that of quarks and gluons.

This is not the end of the story, however, because the light quarks can be bound to the monopoles. The corresponding Dirac equation has no coupling, and the fermionic 3d zero modes are of topological nature, thus they should be present at *any* T. While these bound states are scalars – the spin 1/2 and the color spin 1/2 add up to the grand spin 0 – the quark zero mode can be either occupied or empty, interpreted as 2 separate states, a doublet of the baryon number $B=\pm 1/2$ [116]. So, in the theory with a single light quark, $N_f=1$, the number of magnetic states doubles.

In a theory with $N_f=2$, one can get the $B=1$ *triplet* of states. Its flavor-asymmetric wave function can be, for example, viewed as the isospin-0 ud diquark, the antidiquark, and also the η isoscalar meson added to a monopole. The number of magnetically charged states is, in this case, $2\cdot 2\cdot 3=12$. While this is still smaller than the number of quark and gluon degrees of freedom, it is not a negligible contribution.

A qualitative observation made by Liao and Shuryak [117] was that, with the number of monopole-quark species growing with N_f, it becomes more and more difficult to produce Bose-Einstein condensation, since the objects become distinguishable. This tendency can only be counterbalanced by a corresponding increase of the monopole density. And indeed, lattice simulations for QCD-like theories with an increasing N_f have found that deconfinement transition corresponds to stronger coupling $g^2(T_{\rm c})$, smaller monopole mass and therefore higher monopole density.

All dimensional quantities are defined following standard lattice convention for units: the vacuum string tension for all theories is declared to be the same in MeV. With such units, the critical temperature for SU(2) and SU(3) is different, ~ 300 MeV for SU(2) and ~ 260 MeV for SU(3), but the densities of each of the SU(2) and SU(3) monopoles are about the same [65]. If $T_{\rm c}$ is lower, the overall density of monopoles grows, so the density of each separate species of monopole becomes large enough to form a Bose-Einstein condensate. Recall that, as was found in Ref. [65], we observed that the inclusion of an additional interacting component to a Bose Coulomb system did not alter the critical temperature behavior, provided the density of each component was not altered.

The spectroscopy of quark-monopole states in QCD at zero temperature would be very hard to study, because the hybrid (meson-glueball) states would be heavy and wide, mixing with many other mesonic states. But at $T\approx T_{\rm c}$, where the monopoles are relatively light, these states can perhaps be identified. Theoretically, it is also hard to predict their masses; while the Dirac equation for quark fields are indeed written exactly without any coupling present, the Yang-Mills equations for the monopole gauge field itself has only been solved in the classical approximation, in which it is assumed that the monopole action is much larger

than the (one-loop) quark correction to it. As discussed above, this is no longer so near T_c.

Going back to the thermodynamics of QCD, a historically important argument has been related with the mean value of the Polyakov line, $\langle P(T)|P(T)\rangle$. According to lattice data, $\langle P(T)|P(T)\rangle$ approaches 1 at high T very slowly: it reaches 0.8 at $T\approx 350$ MeV according to Fig. 3 of Ref. [118], or $T\approx 500$ MeV according to Fig. 1 of Ref. [119]. This quite far from $T_c\approx 155$ MeV.

While literally it should be applied to the static quarks, one can *conjecture* that the thermodynamical contributions of light quarks should also be proportional to it,

$$n_q(T)\sim\langle P(T)|P(T)\rangle\ . \tag{3.30}$$

This led to the development of the Polyakov-Nambu-Jona-Lasinio (PNJL) model [120, 121] and similar models. Direct lattice studies, e.g. Ref. [122], were able to identify the density of strange quarks, $n_s(T)$, using a certain combination of susceptibilities vanishing for mesons and baryons, but not for quarks. Their results confirm this conjecture rather well. One may further argue that the density of (color non-diagonal) gluons should then be proportional to the square of the Polyakov line, $\langle P(T)|P(T)\rangle^2$. If so, $n_g(T)$ must be even more suppressed near T_c than $n_q(T)$.

At the same time, the energy and entropy densities, ϵ/T^4 and s/T^3, respectively, rise to their approximate scale-invariant value much more rapidly, by $T-T_c\sim 50$ MeV or so, unlike 200-300 MeV for $\langle P(T)|P(T)\rangle$. See, for example, Fig. 6 of Ref. [31]. The inevitable conclusion from these arguments is that there must be some extra contribution, in addition to the quarks and gluons, in this interval of temperature.

It was suggested, e.g. in Ref. [123], that there should be *bound states* of quarks – mesons and baryons – at $T>T_c$. The presence of those are indeed well documented now on the lattice, e.g. in Ref. [122] for strange quarks and later for charmed ones.

We now turn to the following question: what is the contribution of the *monopoles* to the global thermodynamics? Since the monopoles are identified on the lattice individually, with their Euclidean-time paths and correlation functions determined from simulation, it should be possible to calculate their energy. Lamentably, this has not been done yet.

A comparison of the energy density contribution of monopoles to the overall energy density found on the lattice is seen in Fig. 3.18. The SU(2) comparison is direct from our study, as this is the same system from which we found our parameter fits. For SU(3) on the other hand, we have estimated the monopole contribution to the energy density by simply multiplying the contribution by 2, as discussed above. This, of course, does not take into account the energy coming from the interaction between the two species, which will have to be studied further in the future. Finally, for QCD, from standard counting of degrees of freedom, one finds that quarks have about twice more of those than gluons, so the QGP energy density in QCD is about 3 times larger than in the pure gauge SU(3). The number of quark-monopole states, as we argued above, for two light flavors also increase the number of species by the factor of 3.

The monopole mass, as found in Ref. [64], contributes significantly more to the overall thermodynamics than the internal energy of the monopoles (c.f. Fig. 3.17). In Fig. 3.18, we see the total energy density contribution from the monopoles to the system. When the mass is included, the monopoles contribution constitutes the *entire* energy density of the system between 1-1.3T_c.

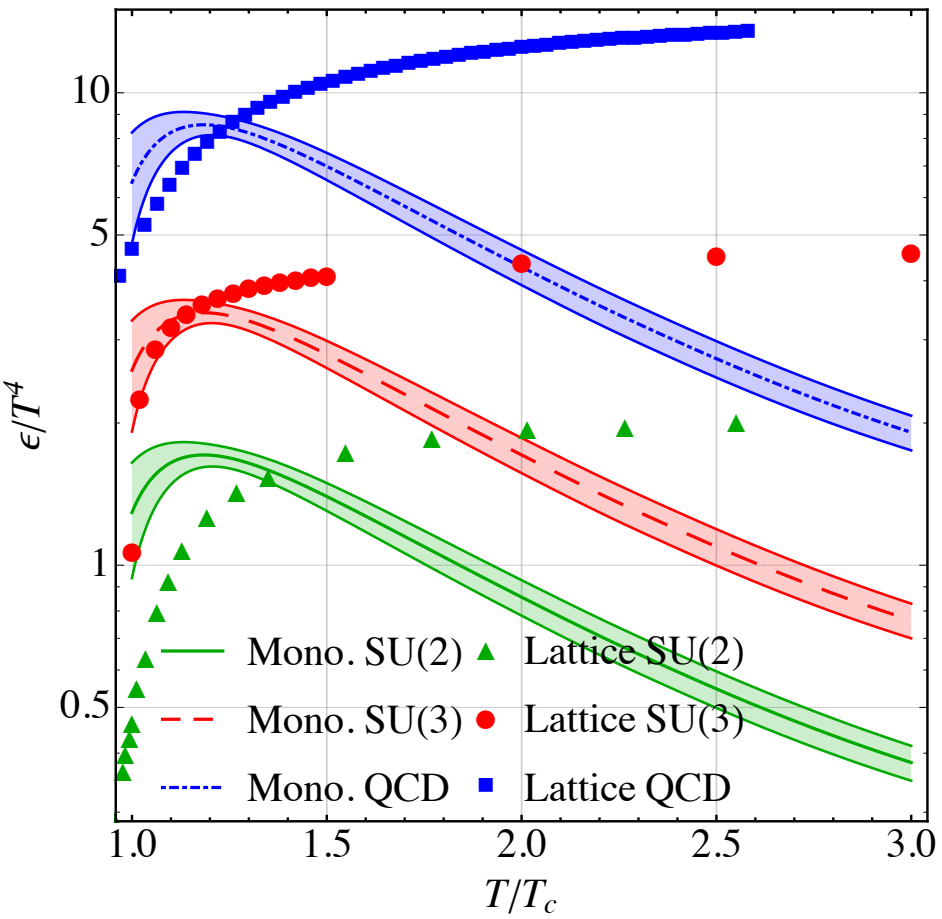

Figure 3.18: The energy density of the monopoles compared to lattice data for pure-gauge SU(2) and SU(3). The estimates for the monopole contribution to SU(3) and QCD are from a scaling argument (see text). Lattice SU(2) results are from Refs. [124, 125], SU(3) from Ref. [126], and QCD from Ref. [31].

3.5 Summary

In this chapter, we have studied the effects of Coulombic interaction on the Bose-Einstein condensation. We numerically calculated the critical temperature T_c, of one- and two-component Coulomb systems, by two different methods, as a function of the interaction strength. Qualitatively, the dependence is the similar to what has been previously observed for hard spheres: T_c moderately grows at weak coupling but strongly decreases at strong coupling.

We also studied the spatial correlations in these systems at various temperatures and coupling strengths. We then mapped the results of the two-component case to the results of lattice simulations of color magnetic monopoles in pure-gauge SU(2), and find a very good agreement. This comparison allowed us to fix the "physical line" in the parameter space of our effective model in SU(2) gauge theory, at and above T_c. As a result of simulations, we believe that a two-component Coulomb quantum Bose gas model accurately replicates monopole behavior seen on the lattice.

We have also determined the monopole contribution to the overall thermodynamics (energy density) of the thermal matter, at and above T_c in pure-gauge SU(2), and made estimates for SU(3) and QCD theories. We concluded that the monopoles possibly dominate the thermodynamics just above T_c in the case of SU(2) and SU(3). We speculate that the same is true in QCD with light quarks, although the questions related with properties of monopole-quark composites have not yet been addressed.

Now having an effective quantum model for magnetic sector of the gauge theories, one may think of its applications beyond quantities calculable in Euclidean-time framework, in particular, to the transport properties of hot hadronic matter. The impact of monopoles on QGP viscosity η have been studied in Ref. [70], but only considering the transport cross section of binary collisions, not a full many-body theory. The role of jet-monopole scattering in another transport parameter – $\hat{q}$ – has been studied phenomenologically in Refs. [37, 39], which suggested that monopoles are the main degree of freedom contributing to η and $\hat{q}$ near and above T_c. We will study monopole effects in jet quenching further in the next chapter.

Chapter 4

Jet Quenching in Heavy-Ion Collisions

This chapter is based on:

- A. Ramamurti and E. Shuryak (2018). Role of QCD monopoles in jet quenching. Phys. Rev. **D97**(1), 016010. doi:10.1103/PhysRevD.97.016010 arXiv:1708.04254.

Another unusually-behaving kinetic parameter of quark-gluon plasma is the mean squared momentum transfer per unit length for high energy partons, denoted $\hat{q}$. As mentioned in the introductory section on jet quenching, experimental observations suggest this transport coefficient needs to be enhanced as compared to naïve perturbative scattering on quarks and gluons.

The purpose of this chapter is to attempt to complement multiple phenomenological models, including scattering on quarks and gluons, as well as on monopoles [39, 37], by a direct calculation of radiative energy loss [127] from the same lowest-order cross section. We use the Baier-Dokshitzer-Mueller-Peigne-Schiff (BDMPS) framework [41, 43], which ascribes the energy loss to gluon radiation caused by transverse "kicks" from the "scatterers" in the medium.

We will study the changes in R_{AA} and v_2 caused by monopoles, including the realistic temperature-dependent monopole densities and monopole correlations. In addition, we will study the effects due to changes in the initial conditions of the medium and the background medium evolution. From our simulations, we will also calculate the dijet asymmetry, A_j. Finally, we will make jet quenching predictions for lower energy collisions to be probed in the upcoming Beam Energy Scan program at RHIC.

4.1 Parameters for Jet Quenching Model with Monopoles

From the BDMPS model of jet quenching (see Sec. 1.1.1), we have the definition of the coefficient $\hat{q}$ in terms of the density of scatterers and the transport cross section,

$$\hat{q}(z) \approx \rho(z) \int_0^{1/b^2} \mathrm{d}^2\vec{q}_\perp \vec{q}_\perp^{\,2} \frac{\mathrm{d}\sigma}{\mathrm{d}\vec{q}_\perp^{\,2}}(\vec{q}_\perp^{\,2}, z)\,. \tag{4.1}$$

The generic form of $\mathrm{d}\sigma/\mathrm{d}q_\perp^2$ in QCD is

$$\frac{\mathrm{d}\sigma}{\mathrm{d}q_\perp^2} = \frac{C}{(q_\perp^2 + \mu^2)^2}\,, \tag{4.2}$$

For quarks $C_F = 4/3$ and for gluons $C_A = 3$, so, as it is well known [127, 41], we have that

$$\frac{\mathrm{d}\sigma_{qq}}{\mathrm{d}q_\perp^2} = \frac{(4/3)^2\pi\alpha_s^2(q_\perp^2)}{(q_\perp^2+\mu_E^2)^2}\,, \tag{4.3}$$

$$\frac{\mathrm{d}\sigma_{qg}}{\mathrm{d}q_\perp^2} = \frac{4\pi\alpha_s^2(q_\perp^2)}{(q_\perp^2+\mu_E^2)^2}\,, \tag{4.4}$$

and

$$\frac{\mathrm{d}\sigma_{gg}}{\mathrm{d}q_\perp^2} = \frac{9\pi\alpha_s^2(q^2)}{(q^2+\mu_E^2)^2}\,. \tag{4.5}$$

Our task at this point is to add scattering on monopoles. Since, for a parton moving ultra-relativistically, the kick from electric and magnetic fields are similar, one expect the same form of the cross section $\mathrm{d}\sigma/\mathrm{d}q^2$, albeit with different factors in the numerator and denominator

$$\frac{\mathrm{d}\sigma_{qm}}{\mathrm{d}q_\perp^2} = \frac{(4/3)\pi F^2(q_\perp^2)}{(q_\perp^2+\mu_M^2)^2}\,, \tag{4.6}$$

$$\frac{\mathrm{d}\sigma_{gm}}{\mathrm{d}q_\perp^2} = \frac{3\pi F^2(q_\perp^2)}{(q_\perp^2+\mu_M^2)^2}\,, \tag{4.7}$$

with $F(q_\perp^2)$ the monopole form factor. For point-like monopoles, we have that $F(q_\perp) = 1$; for finite-size, we can use the standard treatment of Rutherford scattering in the Born approximation, from which we know that the form factor $F(q_\perp) = \exp\{-q_\perp^2 a^2/6\}$ where a is the radius of the scatterer. We only consider long-range Abelian part of the monopole field, and do not take into account a more complicated non-Abelian fields in the monopole core.

There are no factors of α_s in the monopole cross sections, due to the Dirac condition, which makes their magnitude larger relative to the electric-scatterer cross sections. Another aspect of the parton-monopole cross sections is that the screening mass in denominator, μ_M, is the magnetic screening mass, which, according to lattice measurements, is in QGP about twice smaller than the electric mass, μ_E [128].

Let us, as an exercise, integrate the relevant expressions,

$$\int_0^{1/b^2}\mathrm{d}q^2 q^2\frac{1}{(q^2+\mu^2)^2} = -\frac{1}{b^2\mu^2+1} + \log\left(\frac{1}{b^2}+\mu^2\right) - 2\log(\mu)\,, \tag{4.8}$$

$$\int_0^{1/b^2}\mathrm{d}q^2 q^2\frac{\exp\{-q^2a^2/3\}}{(q^2+\mu^2)^2} = \tag{4.9}$$

$$\frac{1}{3}\left(-e^{\frac{a^2\mu^2}{3}}\left(a^2\mu^2+3\right)\left(\mathrm{Ei}\left(-\frac{1}{3}a^2\mu^2\right) - \mathrm{Ei}\left(-\frac{1}{3}a^2\left(\mu^2+\frac{1}{b^2}\right)\right)\right) + \frac{3\mu^2 e^{-\frac{a^2}{3b^2}}}{\frac{1}{b^2}+\mu^2} - 3\right)\,, \tag{4.10}$$

$$\int_0^{\infty}\mathrm{d}q^2 q^2\frac{\exp\{-q^2a^2/3\}}{(q^2+\mu^2)^2} = -\frac{1}{3}e^{\frac{a^2\mu^2}{3}}\left(a^2\mu^2+3\right)\mathrm{Ei}\left(-\frac{1}{3}a^2\mu^2\right) - 1\,. \tag{4.11}$$

The important thing to note is that the $1/b^2$ cutoff has varying effect on the $\hat{q}$ of the monopoles depending on the size of the monopole: for a larger monopole, the energy of the jet does not affect $\hat{q}_m$ as much as $\hat{q}_{q,g}$, which diverge logarithmically with the energy. The lack of logarithmic divergence means that larger monopoles have far less relative effect on high energy quark and gluon jets. Point-like monopoles, on the other hand, behave just as quark and gluon scatterers across all jet energies.

Including $\alpha_s^2(q^2)$ mitigates the logarithmic divergence for the quarks and gluons at high q^2, which increases the role of monopoles when scattering high energy jets. In this work, we will only study point-like monopoles, similar to the treatment of Ref. [37].

While there remains a spread of values of the electric and magnetic screening masses in lattice literature, the general ballpark of those seems to have stabilized over the years. We will follow Ref. [128], who carried out large scale simulations with dynamical quarks with realistic masses. Their results for the magnetic screening mass is $\mu_M/T = 4.48$, and for the electric screening mass $\mu_E/T = 7.31$.

Note that these values, coming from modern lattice works, are significantly larger than the ones used before, and particularly in Ref. [37]. These values lead to a much smaller $\hat{q}$, especially for electric quasiparticle scatterers. This will certainly result in a smaller impact of quarks and gluons in comparison to models that use pQCD – or even older lattice – values for the electric screening mass, as there is a factor of μ_E^4 in the denominator of the transport cross section.

The BDMPS-like energy loss of a parton as it traverses the medium is given by,

$$-\,\mathrm{d}E/\mathrm{d}z \propto \hat{q}z\,. \tag{4.12}$$

Then, for our system, we have,

$$\begin{aligned}
-\mathrm{d}E &= z\mathrm{d}z\frac{\alpha_s N_c}{12}\hat{q}(z,E) \\
&= z\mathrm{d}z\frac{\alpha_s N_c \pi C_p}{12}\left(\rho_q(z)\int_0^{q^2_{\max}}\mathrm{d}q^2\frac{(4/3)\alpha_s^2(q^2)}{(q^2+\mu_E^2(z))^2}\right. \\
&\quad +\rho_g(z)\int_0^{q^2_{\max}}\mathrm{d}q^2\frac{3\alpha_s^2(q^2)}{(q^2+\mu_E^2(z))^2} \\
&\quad \left.+\rho_m(z)C_{\mathrm{corr}}\int_0^{q^2_{\max}}\mathrm{d}q^2\frac{1}{(q^2+\mu_M^2(z))^2}\right)\,,
\end{aligned} \tag{4.13}$$

where z is the coordinate parameterizing the line in the transverse plane along which the parton travels, C_p is the color factor of the jet parton, and C_{corr} is a correction factor due to monopole correlations, to be determined.

The parametrization of the equation of state (pressure) was given in Ref. [31] as,

$$\begin{aligned}
p/T^4 = &\left(\frac{\frac{0.3419}{T^4}+\frac{3.92}{T^2}-\frac{8.7704}{T}+\frac{19\pi^2}{36}}{2\left(-\frac{0.0475}{T^4}+\frac{0.8425}{T^2}-\frac{1.26}{T}+1\right)}\right) \\
&\times\left(\tanh(3.8706(T-0.9761))+1\right)\,,
\end{aligned} \tag{4.14}$$

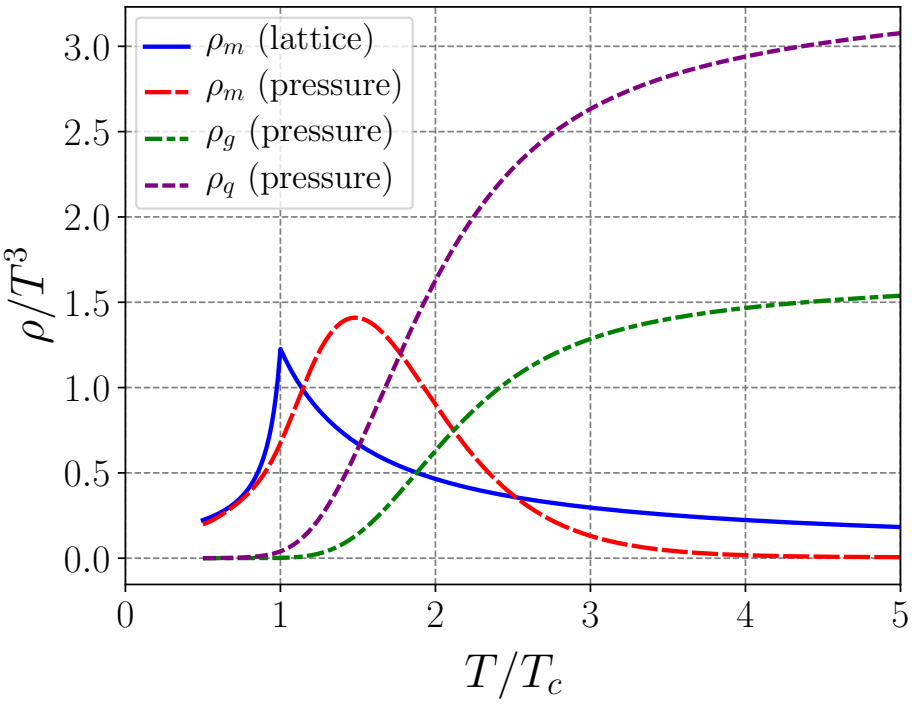

Figure 4.1: Electric and magnetic quasiparticle densities used. The (blue) solid line shows the magnetic monopole density as directly observed on the lattice. The (red) long dashed line is the monopole density extracted from the thermodynamics (pressure), along with the densities of quarks (purple, short dashed) and gluons (green, dot dashed).

and the equation of state for the energy density from Ref. [31] was fitted in Mathematica to be

$$\epsilon/T^4 = \left(\frac{20.89 + \frac{23.55}{T^4} - \frac{57.62}{T^3} + \frac{59.79}{T^2} - \frac{40.37}{T}}{2\left(\frac{0.30}{T^4} + \frac{2.17}{T^3} - \frac{3.56}{T^2} + \frac{0.57}{T} + 1\right)} \right) \times (\tanh(1.17(T - 1.25)) + 1)\,. \tag{4.15}$$

The density of magnetic monopoles is taken from Ref. [65]; the density of each type of monopole (of which there are two in $SU(3)$) is given by

$$\frac{\rho_m}{T^3} = \frac{3.66}{\log((1/0.163)T/T_c)^3}\,. \tag{4.16}$$

Ref. [129] suggests that the monopole density falls off quickly below the critical temperature.

The densities of electric particles are found using the Fermi-Dirac distribution and equation of state (we choose to use the pressure, but one can, in principle, use the entropy instead), following Ref. [37]. The parametrization of the Polyakov loop is

$$L(T) = \left(\frac{1}{2}\tanh(7.69(0.155T - 0.0726)) + \frac{1}{2}\right)^{10}\,, \tag{4.17}$$

and Using the ansatz that $\rho_E(T) \propto c_q L(T) + c_g L^2(T)$, we have that the densities of quarks and gluons, respectively, are given by,

$$\begin{aligned}\rho_q/T^3 =& \frac{1.71E{-}4\,((T(9.87T - 16.6) + 7.43)T^2 + 0.648)}{T^2((T - 1.26)T + 0.843) - 0.0475} \\ &\times (\tanh(3.87(T - 0.976)) + 1) \\ &\times (\tanh(7.69(T - 0.0726)) + 1)^{10}\,,\end{aligned} \tag{4.18}$$

$$\begin{aligned}\rho_g/T^3 =& \frac{(8.48E{-}8)\,((T(9.87T - 16.6) + 7.43)T^2 + 0.648)}{T^2((T - 1.26)T + 0.843) - 0.0475} \\ &\times (\tanh(3.87(T - 0.976)) + 1) \\ &\times (\tanh(7.69(T - 0.0726)) + 1)^{20}\,.\end{aligned} \tag{4.19}$$

For definiteness, in Fig. 4.1 we show the densities of gluons, quarks, and monopoles to be used in the calculations below. One should keep in mind that the plotted density is normalized to T^3. Such a normalization is appropriate at high T, dominated by quarks and gluons, but not necessarily at small T.

In this work, we will use two versions of the monopole density, both obtained from lattice data, but in different ways. The spread of the results is expected to represent the uncertainty existing at the moment. The (blue) solid curve, with a peak at T_c, in Fig. 4.1 shows the "directly observed" monopole density, from Eq. 4.16, which was measured on the lattice [65].

The (red) dashed curve for the density of monopoles, which peaks at about $T \approx 1.5T_c$ rather than at T_c, was derived thermodynamically. It is the monopole density needed to

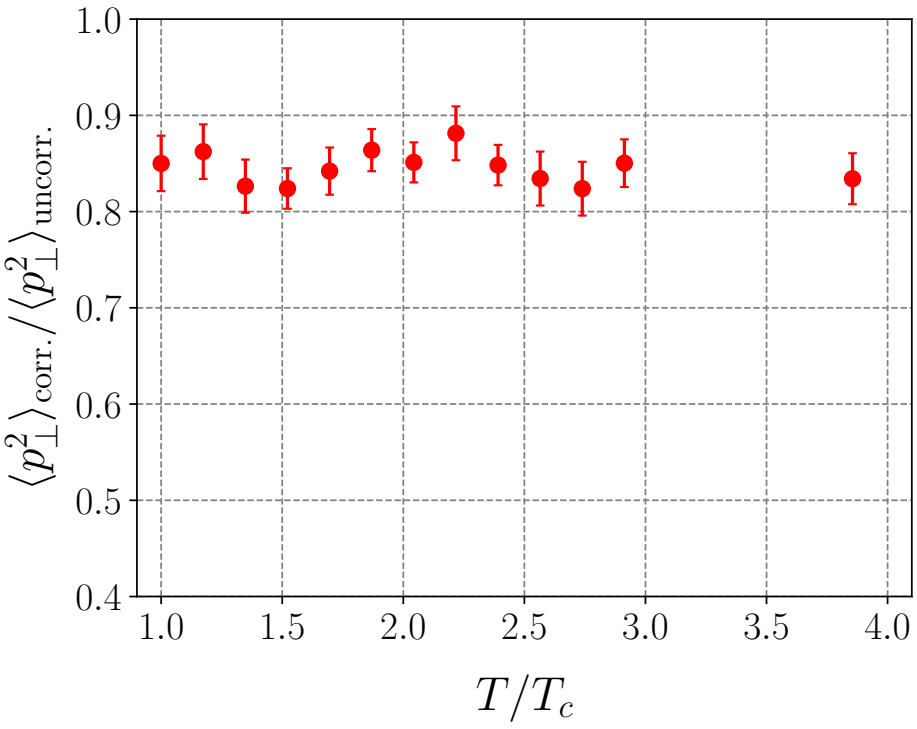

Figure 4.2: Ratio of correlated to uncorrelated average momentum transfer square per mean free path as a function of the temperature.

reproduce the correct pressure (entropy, energy) of QCD as measured on the lattice [31]; in the window of temperatures from $1 - 2T_{\rm c}$, the energy density, pressure, and entropy density produced by electric quasiparticle degrees of freedom is insufficient. As we will show below, a monopole density with a peak around $T_{\rm c}$ seems to be crucial for reproduction of the jet quenching data.

Since the magnetic and electric couplings are comparable, the ensemble of magnetic monopoles constitute a strongly coupled plasma in the region of temperatures above $T_{\rm c}$. In such plasmas, there exist strong correlations between positive and negative charges, which cancel out their fields in some parts of space, reducing their impact on jet quenching.

As expected by the renormalization group flow and Dirac condition, it was directly shown on the lattice (c.f. Refs. [115, 65]) that monopoles become more correlated as temperature is increased [69]. We have evaluated corrections to the monopole contribution to jet quenching using configurations from our previous path-integral Monte Carlo simulations from the previous chapter.

In order to determine the magnitude of this effect, we calculate the net force along a line going through an uncorrelated configuration (random distribution of monopoles and antimonopoles), and then through a random sample of the configurations of the effective model for monopoles.

The correlations in the plasma are not extremely strong (there is no crystal like structure, etc.) but are indeed present – the maximal deviation from 1 of the radial distribution function

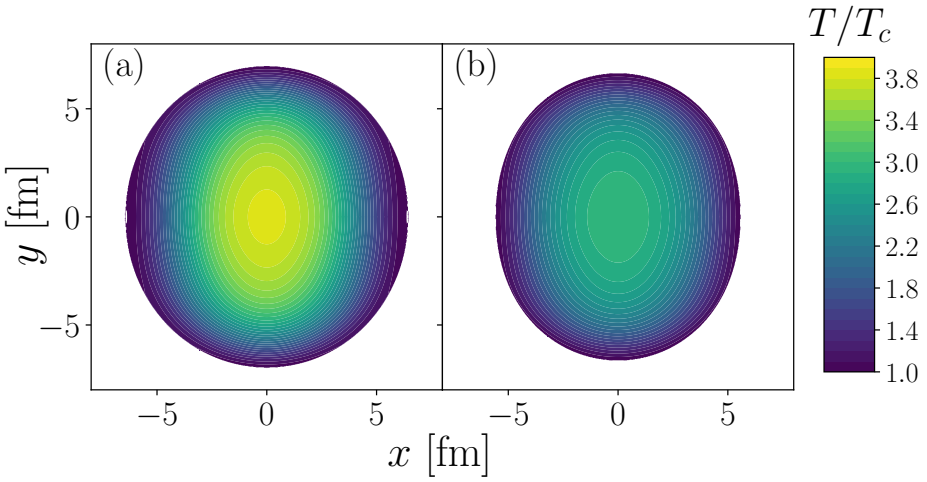

Figure 4.3: Temperature profile of 20-30% centrality (a) 2.76 TeV Pb-Pb and (b) 200 GeV Au-Au collisions calculated using the energy density profile at $\tau = 0.2$ fm/c from Ref. [130] and equation of state from Ref. [31].

is 0.2 at $1.1T_c$ and 0.4 at $3.8T_c$; see Refs. [115, 65] for detailed plots of the radial distribution functions.

Fig. 4.2 shows the ratio of the average momentum transfer squared per unit length for the correlated and uncorrelated cases. From T_c to $4T_c$, the ratio is approximately 0.85, meaning that the correlations reduce the $\hat{q}$ by 15%. Intuitively, the reduction of transferred momentum was expected, since the force on a jet from + and − charges will increasingly cancel the more correlated they are.

4.2 Background Matter Evolution

Before we embark on the evaluation of the jet quenching parameters, we need to define the fireball temperature, energy density, and entropy density profiles. For this study, we will focus on one specific bin, 20-30%, of centrality, both for LHC and RHIC collisions. Assuming very rapid equilibration, the relation between these profiles are given by equilibrium equation of state (EoS), which has been well studied on the lattice.

For definiteness, we use parameterization of the energy density from the lattice data of Ref. [31], given in Eq. 4.15. The initial energy density distribution corresponding to standard Glauber-type analysis, as in Ref. [130]. The (smooth) temperature profiles of the fireballs at $\tau = 0.2$ fm/c are shown in Fig. 4.3 for both RHIC and LHC energies. One can see that the absolute size and the ellipticity of the near-T_c peripheral regions (blue-purple) are in fact slightly different. We also calculated all quantities with IP-Glasma initial conditions, which include fluctuating color fields.

As a first step, we start with simple Bjorken (1+1)D expansion, with the temperature decreasing with time as $T(\tau, x, y) = T(\tau_0, x, y)(\tau/\tau_0)^{-1/3}$. In a Bjorken-expanding background, the temperature in all regions decrease with time in the same way, and the matter does not

expand in the transverse direction.

We then apply a more realistic (2+1)D hydrodynamic evolution, with both smooth and fluctuating initial conditions. An example of a realistic medium evolution we will use is shown in Fig. 1.6. One can see that, as time progresses, the (purple) near-T_c region rather quickly takes over the whole fireball, but that the overall size of the fireball region at and above T_c remains approximately the same, unlike what would happen in the (1+1)D Bjorken expansion scenario. Another observation, most clear from last two subplots, is that eventually the system splits into two "nut shells," making the azimuthal asymmetry stronger.

As we will see, the hydrodynamic background has an important influence on the results of our jet quenching calculations. As such, it is important that we also reproduce the soft physics of these heavy-ion collisions. The IP-Glasma with hydrodynamics given by MUSIC are studied in Refs. [131, 132], and in general give good agreement with hadronic observables.

For our hydrodynamics with optical Glauber initial conditions [133], the simulated and experimental hadronic observables are shown in Tables 4.1, 4.2, and 4.3, for 62.4 GeV Au-Au, 200 GeV Au-Au, and 2.76 TeV Pb-Pb collisions, respectively, for hydrodynamics with bulk viscosity; Table 4.4 shows the calculation for hydrodynamics without bulk viscosity [133]. In general, we have good agreement with data. The v_2 of our calculations is smaller than that of experiment, which is a well-known result of using optical Glauber initial conditions.

Table 4.1: Comparison of calculated and experimental hadronic observables in 62.4 GeV Au-Au collisions, for hydrodynamics with bulk viscosity. Data from Ref. [134].

	hydro. calc.	data
N_{pion}	97.75	98.9±6.9
$\langle p_T \rangle_{\text{pion}}$	0.412	0.403±0.013
$v_2(p_T = 0.2 - 1.0)$	0.054	0.0613
$v_2(p_T = 1.0 - 2.0)$	0.163	0.132

Table 4.2: Comparison of calculated and experimental hadronic observables in 200 GeV Au-Au collisions, for hydrodynamics with bulk viscosity. Experimental data is the same as used in Refs. [131, 132].

	hydro. calc.	data
N_{pion}	133.4	135±10
$\langle p_T \rangle_{\text{pion}}$	0.422	0.411±0.021
v_2	0.059	0.0642

4.3 Jet Quenching at RHIC and LHC energies

The probability distributions of quark and gluon jets in their transverse momenta and the location of production were generated by Monte Carlo algorithm in a standard perturbative way, based on Refs. [135, 136]. The essential point is that the probability of jet production at a particular location is proportional to the product of two nuclear thickness functions,

Table 4.3: Comparison of calculated and experimental hadronic observables in 2.76 TeV Pb-Pb collisions, for hydrodynamics with bulk viscosity. Experimental data is the same as used in Refs. [131, 132].

	hydro. calc.	data
N_{pion}	309.1	307±20
$\langle p_T \rangle_{\text{pion}}$	0.508	0.512±0.017
v_2	0.0746	0.0831±0.0034

Table 4.4: Comparison of calculated and experimental hadronic observables in 2.76 TeV Pb-Pb collisions, for hydrodynamics without bulk viscosity. Experimental data is the same as used in Refs. [131, 132].

	hydro. calc.	data
N_{pion}	299.079	307±20
$\langle p_T \rangle_{\text{pion}}$	0.616	0.512±0.017
v_2	0.075	0.0831±0.0034

and that the jet energy spectrum is given by a power law. The produced jets traverse the medium, from the origination point, with an isotropic distribution.

To calculate hadronic observables from jets, we must apply fragmentation functions to the outgoing quarks and gluons. In this work, we will use the fragmentation functions from Ref. [137] for light quark and gluon jets, going into unidentified charged hadrons and also to neutral pions.

Energy loss

The results for $\Delta E/E$ of the jet (prior to fragmentation), R_{AA}, and v_2 of fragmented jets are seen in Figs. 4.4, 4.5, and 4.6, respectively. The collider data are from Refs. [138, 139] for LHC 2.76 Pb-Pb TeV R_{AA} and Refs. [140, 141] for RHIC 200 GeV Au-Au R_{AA}; Refs. [142, 143] for the LHC 2.76 TeV Pb-Pb v_2 and Ref. [144] for RHIC 200 GeV Au-Au v_2.

All of the plots are laid out as follows: the first column, comprising subplots (a) and (b), is for LHC 2.76 TeV Pb-Pb collisions, and the second column – subplots (c) and (d) – is for RHIC 200 GeV Au-Au. The first row is for the monopole density measured on the lattice, and the second row is for monopole density derived from the equation of state.

All curves shown are for *correlated* monopoles; the effects of correlations on the results will follow shortly. The calculations shown are for IP-Glasma initial conditions and (2+1)D hydrodynamics with bulk viscosity, $\zeta \neq 0$ (red, solid curves); optical Glauber initial conditions and (2+1)D hydrodynamics with bulk viscosity, $\zeta \neq 0$ (blue, dash-dot curves); optical Glauber initial conditions and (2+1)D hydrodynamics without bulk viscosity, $\zeta = 0$ (green, dash-dot-dot curves); and optical Glauber initial conditions and (1+1)D Bjorken expansion (purple, dashed curves).

As shown in Fig. 4.4, the Bjorken-evolving background (purple, dashed curve) causes far less energy loss than the scenarios with realistic hydrodynamic backgrounds. This is due to the fact that this is a one-dimensional expansion, and the matter does not expand in the

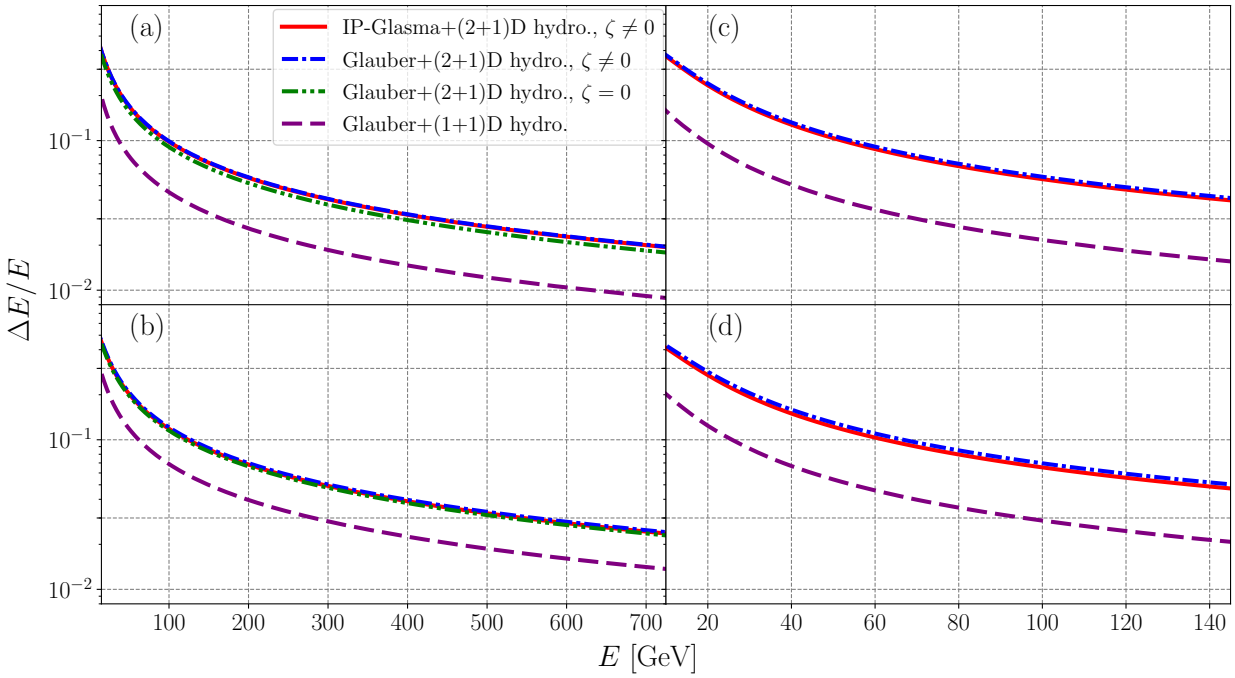

Figure 4.4: Ratio of energy loss to initial parton jet energy in 2.76 Pb-Pb collisions (a),(b), and 200 GeV Au-Au collisions (c),(d). The first row (a),(c) is the results for monopole density from the lattice, while the second row (b),(d) is results for monopole density from the equation of state. The (red) solid curve is for IP-Glasma initial conditions and (2+1)D hydrodynamics with bulk viscosity ($\zeta \neq 0$), the (blue) dash-dot curve is for Glauber initial conditions and (2+1)D hydrodynamics with bulk viscosity ($\zeta \neq 0$), the (green) dash-dot-dot curve is for Glauber initial conditions and (2+1)D hydrodynamics without bulk viscosity ($\zeta = 0$), and the (purple) dashed curve is for the smooth Glauber initial condition with (1+1)D Bjorken evolution.

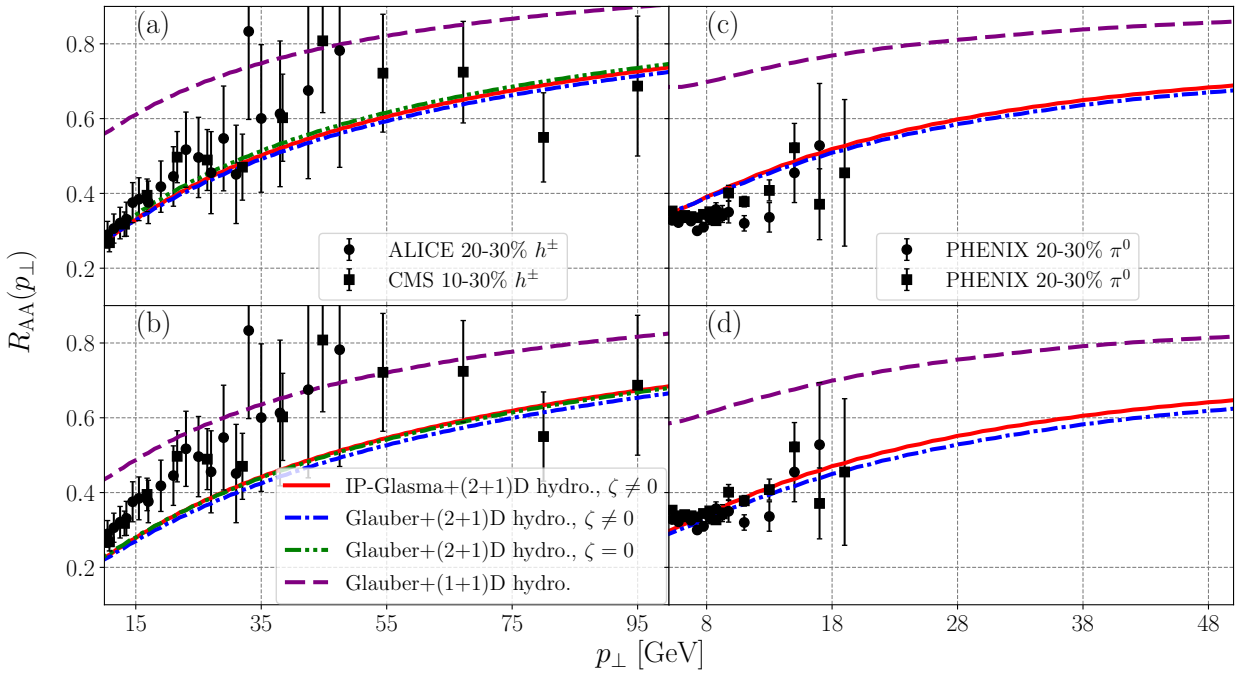

Figure 4.5: Nuclear modification factor of charged hadrons in 2.76 Pb-Pb collisions (a),(b), and neutral pions in 200 GeV Au-Au collisions (c),(d). The first row (a),(c) is the results for monopole density from the lattice, while the second row (b),(d) is results for monopole density from the equation of state. The (red) solid curve is for IP-Glasma initial conditions and (2+1)D hydrodynamics with bulk viscosity ($\zeta \neq 0$), the (blue) dash-dot curve is for Glauber initial conditions and (2+1)D hydrodynamics with bulk viscosity ($\zeta \neq 0$), the (green) dash-dot-dot curve is for Glauber initial conditions and (2+1)D hydrodynamics without bulk viscosity ($\zeta = 0$), and the (purple) dashed curve is for the smooth Glauber initial condition with (1+1)D Bjorken evolution. Collider data from Refs. [138, 139] for LHC and Refs. [140, 141] for RHIC.

transverse plane; the ellipse of above-T_c medium shrinks inwards to the center of the fireball with time. This is unlike the (2+1)D hydrodynamic case (c.f. Fig. **??**), where the size of the above-T_c medium remains approximately constant with time, and all of the medium cools to approximately T_c by $\tau \sim 6$ fm/c.

Therefore, in the Bjorken-evolving case, the parton jet "sees" far less medium during its traversal of the fireball, causing less energy loss. On the other hand, the Glauber and IP-Glasma initial condition models lead to a larger energy loss. This loss is very similar with all initial conditions, provided that the hydrodynamic evolution is realistic.

Nuclear modification factor

Since R_{AA} is another measure of medium-induced energy loss, the results are very similar to that of $\Delta E/E$. Shown in Fig. 4.5, the Glauber and IP-Glasma initial conditions coupled to realistic hydrodynamic models all agree with each other, while the Bjorken evolution gives

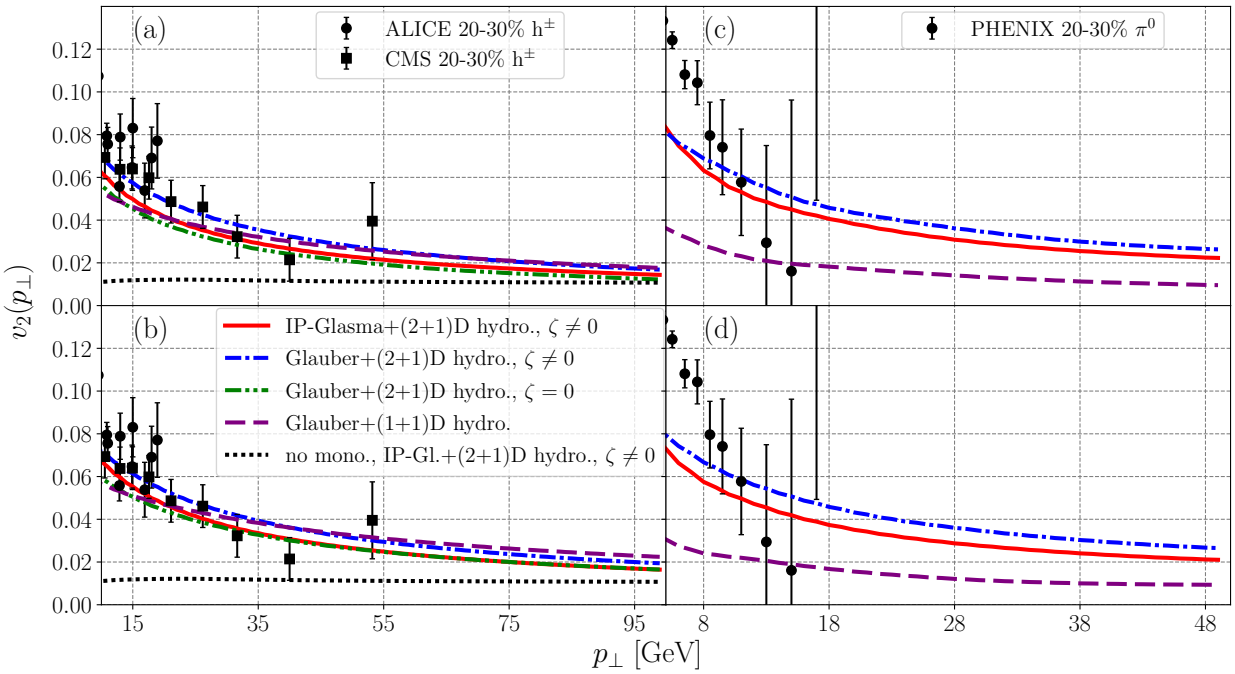

Figure 4.6: Azimuthal anisotropy of charged hadrons in 2.76 Pb-Pb collisions (a),(b), and neutral pions in 200 GeV Au-Au collisions (c),(d). The first row (a),(c) is the results for monopole density from the lattice, while the second row (b),(d) is results for monopole density from the equation of state. The (red) solid curve is for IP-Glasma initial conditions and (2+1)D hydrodynamics with bulk viscosity ($\zeta \neq 0$), the (blue) dash-dot curve is for Glauber initial conditions and (2+1)D hydrodynamics with bulk viscosity ($\zeta \neq 0$), the (green) dash-dot-dot curve is for Glauber initial conditions and (2+1)D hydrodynamics without bulk viscosity ($\zeta = 0$), and the (purple) dashed curve is for the smooth Glauber initial condition with (1+1)D Bjorken evolution. The (black) dotted curve is for for IP-Glasma initial conditions and (2+1)D hydrodynamics with bulk viscosity ($\zeta \neq 0$) with no monopoles. Collider data from Refs. [142, 143] for the LHC and Ref. [144] for RHIC.

a much larger result that is incompatible with the experimental data. The LHC 2.76 TeV Pb-Pb $R_{\rm AA}$ data is better fit by the monopole density measured on the lattice (upper left panel), compared to that given by the equation of state (lower left panel). On the other hand, the RHIC 200 GeV Au-Au $R_{\rm AA}$ is fit quite well by both monopole densities when using realistic hydrodynamic backgrounds.

Azimuthal anisotropy

The azimuthal anisotropy, is shown in Fig. 4.6. Without monopoles – the black dotted line on the left panels – the v_2 is roughly .015, much smaller than the experimental data. The v_2 results for both monopole densities roughly agree with LHC 2.76 TeV Pb-Pb v_2 data when using hydrodynamic backgrounds, including Bjorken evolution. The v_2 for RHIC 200 GeV Au-Au data is not in complete agreement for the (2+1)D hydrodynamic models

(Glauber and IP-Glasma initial conditions); the slope is less steep in the model than in the data, although the order of magnitude is correct. On the other hand, the model disagrees strongly with Bjorken expansion.

Effect of fluctuations

In all the preceding discussion, we see that, with minor variation, the $\Delta E/E$, $R_{\rm AA}$, and v_2 obtained with Glauber and IP-Glasma initial conditions and realistic hydrodynamics (blue dash-dot, green dash-dot-dot, and red solid curves) all agree with each other. This leads us to believe that initial-state fluctuations play only a small role in these quantities and that event-by-event analysis is not necessary, which is opposite to what is claimed in Ref. [38]; the inclusion of monopoles in our jet quenching framework allows for the simultaneous description of v_2 and $R_{\rm AA}$ even when using smooth initial conditions.

This most likely occurs because our model is most sensitive to near-$T_{\rm c}$ medium, which is on the periphery at early times; at later times, when the whole fireball is near-$T_{\rm c}$, most of the initial state fluctuations are more-or-less damped out. If a model for jet energy loss focuses on early times or is sensitive more to medium at higher temperatures, then the fluctuations would play a much larger role.

In addition, whether or not the hydrodynamic evolution has bulk viscosity does not make a large difference; the variation between the Glauber initial condition with and without bulk viscosity can be explained by the difficulty in tweaking parameters producing the correct hadron yield without bulk viscosity, giving a different background for the jet to traverse.

This discrepancy in $R_{\rm AA}$ between the two forms of monopole density – the EoS density not working for 2.76 TeV collisions and both the lattice and EoS densities working for 200 GeV collisions – can be explained by the difference in high-temperature behavior. While both have relatively similar peaks near $T_{\rm c}$, the pressure scheme density goes to zero by $T/T_{\rm c} = 4$, and is less than the lattice scheme by $T/T_{\rm c} = 2.5$; see Fig. 4.1.

On the other hand, the lattice measured density does not go to zero at high temperature, but rather falls off as $\rho/T^3 \sim \log(T/T_{\rm c})^{-3}$. As a result, at higher energy collisions (where the temperature is higher at initial time), the variant with directly observed lattice monopoles gives a different monopole contribution than the thermodynamical fit, while in the lower energy collisions, the contributions end up being similar.

At very low energies, where the initial temperature is just around $T_{\rm c}$, the sensitivity of the jet quenching parameters to the monopole density is the highest. This means, that if the future PHENIX experiment at RHIC will be able to study jet quenching in the low energy range, we will get better understanding of the location of the monopole density peak. Understanding of this quantity is key in determining the effects of monopoles on parton jets.

Dijet asymmetry

In our simulations, we also generated back-to-back partons of the same initial energy, and evaluated the energy lost by each of them. The difference is known as the *dijet asymmetry*, and is characterized by,

$$A_j = \frac{|E_1 - E_2|}{E_1 + E_2}\,. \tag{4.20}$$

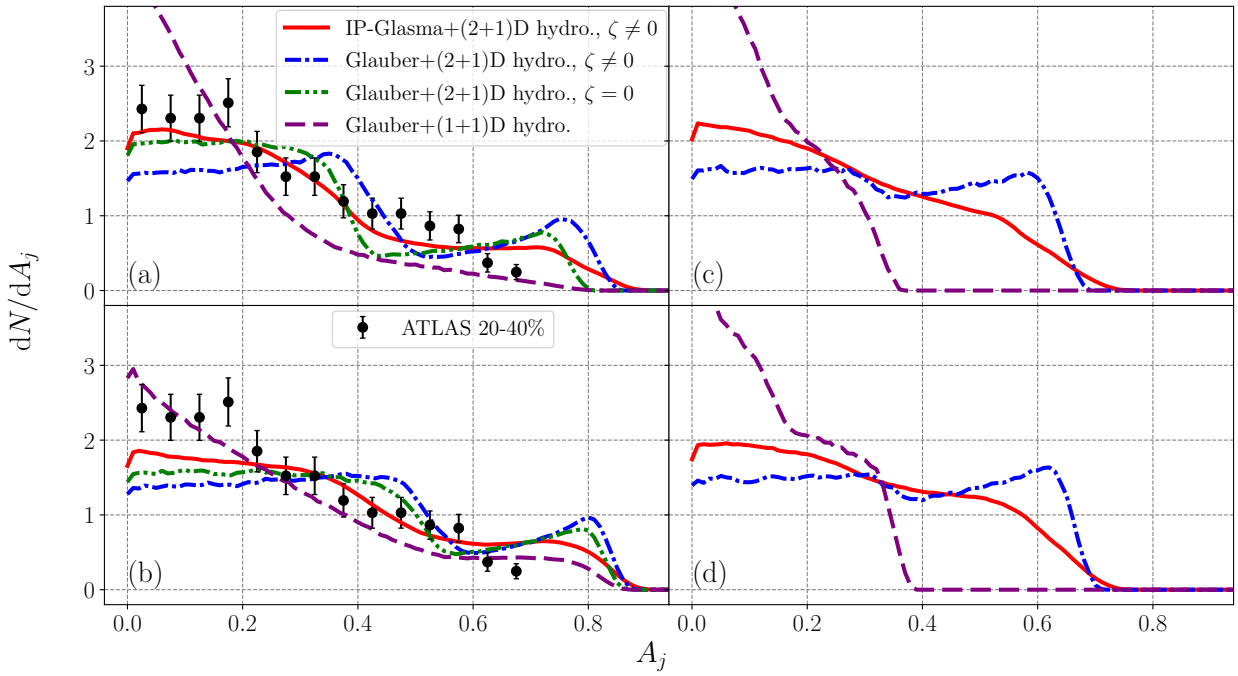

Figure 4.7: Dijet asymmetry of parton jets in 2.76 Pb-Pb collisions (a),(b), and 200 GeV Au-Au collisions (c),(d). The first row (a),(c) is the results for monopole density from the lattice, while the second row (b),(d) is results for monopole density from the equation of state. The (red) solid curve is for IP-Glasma initial conditions and (2+1)D hydrodynamics with bulk viscosity ($\zeta \neq 0$), the (blue) dash-dot curve is for Glauber initial conditions and (2+1)D hydrodynamics with bulk viscosity ($\zeta \neq 0$), the (green) dash-dot-dot curve is for Glauber initial conditions and (2+1)D hydrodynamics without bulk viscosity ($\zeta = 0$), and the (purple) dashed curve is for the smooth Glauber initial condition with (1+1)D Bjorken evolution. Collider data from Ref. [145].

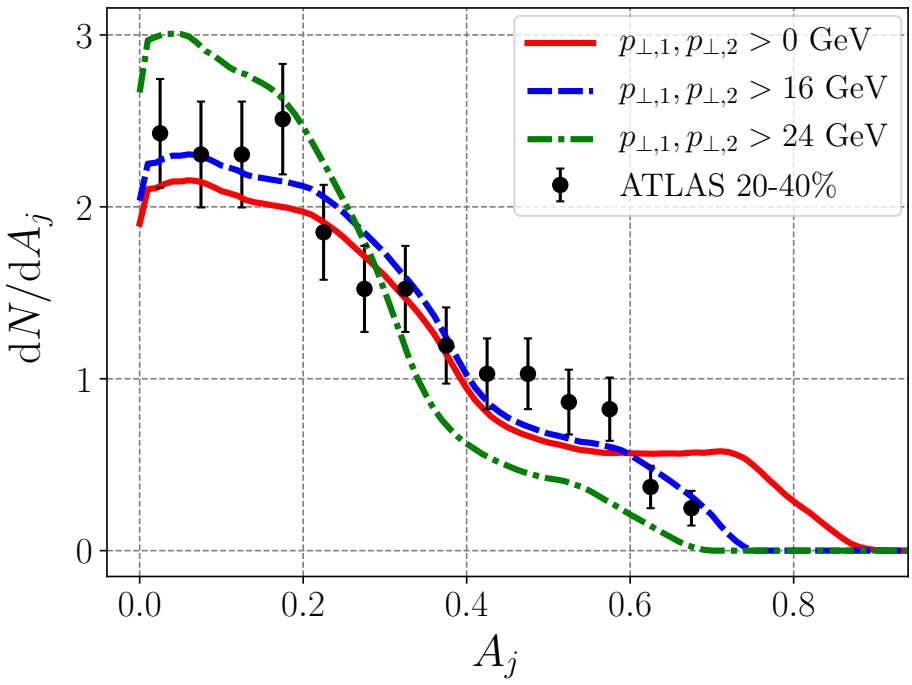

Figure 4.8: Dijet asymmetry of parton jets with no $p_\perp$ cut (red, solid curve), $p_\perp > 16$ GeV (blue, dashed curve), and $p_\perp > 24$ GeV (green, dot-dashed curve) in 2.76 Pb-Pb collisions for the IP-Glasma initial conditions with (2+1)D hydrodynamics with bulk viscosity and monopole density given by the lattice. Collider data from Ref. [145].

This quantity is plotted in Fig. 4.7. The data for LHC 2.76 TeV Pb-Pb are from Ref. [145].

We first note that the Glauber and IP-Glasma initial conditions with realistic hydrodynamics (blue dash-dot, green dash-dot-dot, and red solid curves) all roughly follow the experimental data. There is more distinction between the different initial conditions in this quantity, and the best agreement seems to be with the IP-Glasma initial condition and, as before with R_{AA}, with the monopole density as measured on the lattice. In the case of the dijet asymmetry, we find that initial-state fluctuations play a role in explaining the distribution of energy loss asymmetry between back-to-back parton jets.

Fig. 4.7 also shows a distinctive bump at $A_j \approx 0.8$ for LHC energies and $A_j \approx 0.6$ for RHIC energies. This bump is due to the fact that we have included jets with low initial energy in our calculations. An asymmetry of $A_j = 1$ would indicate that one jet was completely quenched by the medium. The bump comes from the fact that, for low energy back-to-back jets, there is a significant likelihood that the relative difference in final energies is larger, leading to a larger A_j. Since low energy jets are much more probabilistic than high energy jets, these events accumulate.

Therefore, the location of this bump and its size are dependent on the low-energy limit of the produced jets in simulations and any imposed cuts on final jet energies in both simulations and experiment. We also note that the IP-Glasma initial conditions give less pronounced of a bump than other initial conditions.

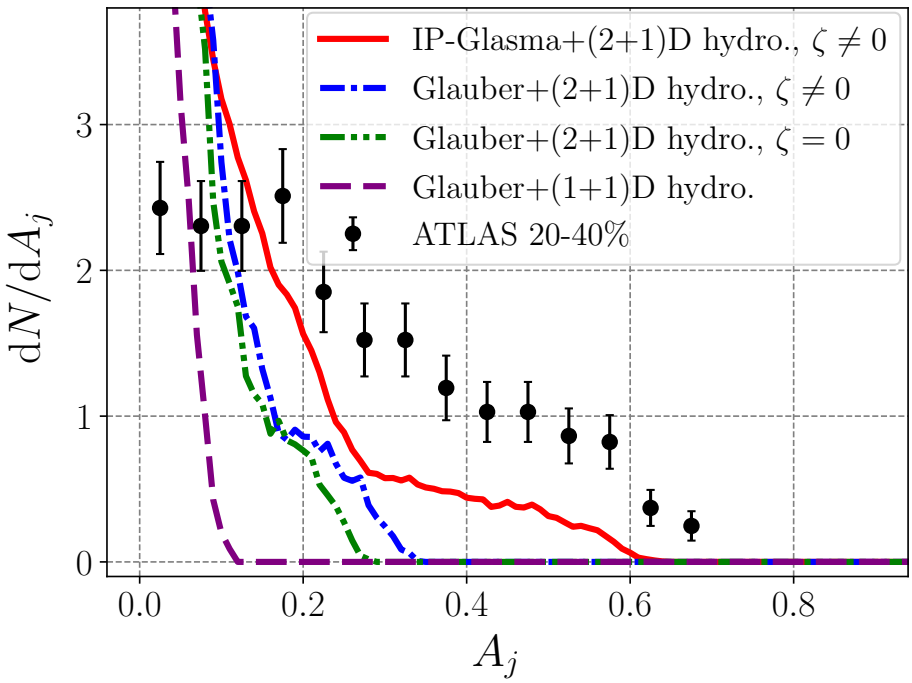

Figure 4.9: Dijet asymmetry of parton jets originating in the center of the fireball in 2.76 Pb-Pb collisions with the monopole density from the lattice. The (red) solid curve is for IP-Glasma initial conditions and (2+1)D hydrodynamics with bulk viscosity ($\zeta \neq 0$), the (blue) dash-dot curve is for Glauber initial conditions and (2+1)D hydrodynamics with bulk viscosity ($\zeta \neq 0$), the (green) dash-dot-dot curve is for Glauber initial conditions and (2+1)D hydrodynamics without bulk viscosity ($\zeta = 0$), and the (purple) dashed curve is for the smooth Glauber initial condition with (1+1)D Bjorken evolution. Collider data from Ref. [145].

This bump can, in principle, be (re)moved by a final parton energy $p_\perp$ cut, as is done in experimental analyses. Fig. 4.8 shows an example of this for the results of the IP-Glasma+(2+1)D hydrodynamic simulations of 2.76 TeV Pb-Pb collisions and monopole density given by the lattice, for cuts $p_\perp > 16$ GeV (blue dashed curve) and a $p_\perp > 24$ GeV (green dash-dot curve). The bump at large A_j disappears and the general shape of the curves are altered; this happens for all curves and at LHC and RHIC energies.

It is clear that the dijet asymmetry is very sensitive to the range of energies selected for the back-to-back jets. In particular, the $p_\perp > 16$ GeV cut shown in Fig. 4.8 (blue dashed curve) makes the calculation with the most realistic background, the IP-Glasma fluctuating initial conditions, roughly follow the experimental data.

We conclude that our model, with realistic initial conditions, can qualitatively produce the correct behavior of the dijet asymmetry. The response of our data to the adjustment the $p_\perp$ cuts shows the sensitivity of the observable to various parameters introduced in both theoretical and experimental analysis, and therefore requires much more study.

Shown in Fig. 4.9 is the result for the dijet asymmetry A_j selecting only jets that start in

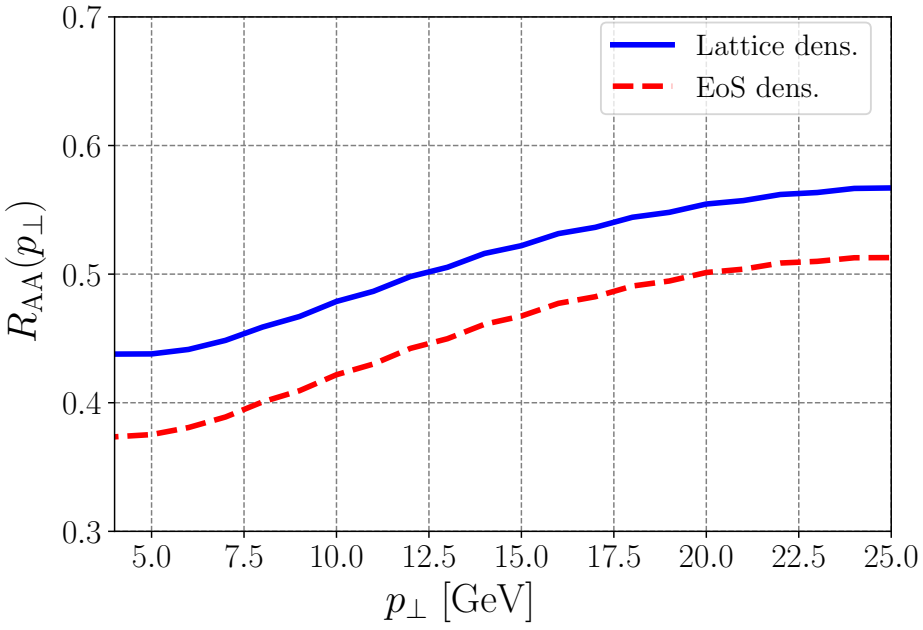

Figure 4.10: Nuclear modification factor of neutral pions for 62.4 GeV Au-Au collisions. The (blue) solid curve is the result for monopole density from the lattice, and the (red) dashed curve is the result for monopole density from thermodynamics.

the center of the fireball, for 2.76 TeV Pb-Pb collisions and the monopole density found on the lattice. The data is definitively *not* reproduced by any of the curves, which shows that the asymmetry, in this model, comes from the path-length difference between the trigger and secondary jets, rather than from the fluctuations in the matter or in the fragmentation processes.

We do not take into account relativistic effects of the fluid flow velocity on the jet. This was studied in Appendix A of Ref. [39]; the authors concluded that, for R_{AA} and v_2, this correction was negligible. This is expected since our model only takes into account the instantaneous impact parameter between the jet parton and the scatterer; the cross sections depend on momentum transfer t but not on the energy s.

Predictions for the Beam Energy Scan

With the sPHENIX detector, RHIC will be able to detect jets in lower energy collisions. As stated earlier, monopole effects are strongest near T_{c}, and if we are able to study jet quenching in this lower energy range where most of the matter has a temperature of approximately T_{c}, we will get a better understanding of monopole features, such as the location and shape of the density peak.

In preparation for these experiments, we seek to make predictions – with our jet quenching framework and Glauber initial conditions for a 62.4 GeV Au-Au collision – for how jet observables will be altered when probing lower energy collisions. For the most realistic results, we would need a better understanding of the initial conditions and hydrodynamic expansion

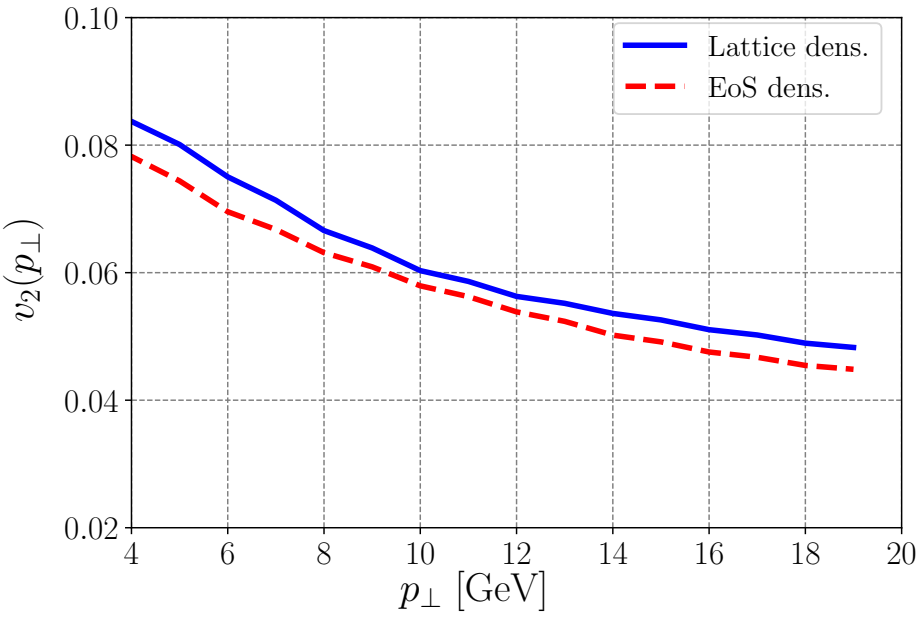

Figure 4.11: Azimuthal anisotropy of neutral pions for 62.4 GeV Au-Au collisions. The (blue) solid curve is the result for monopole density from the lattice, and the (red) dashed curve is the result for monopole density from thermodynamics.

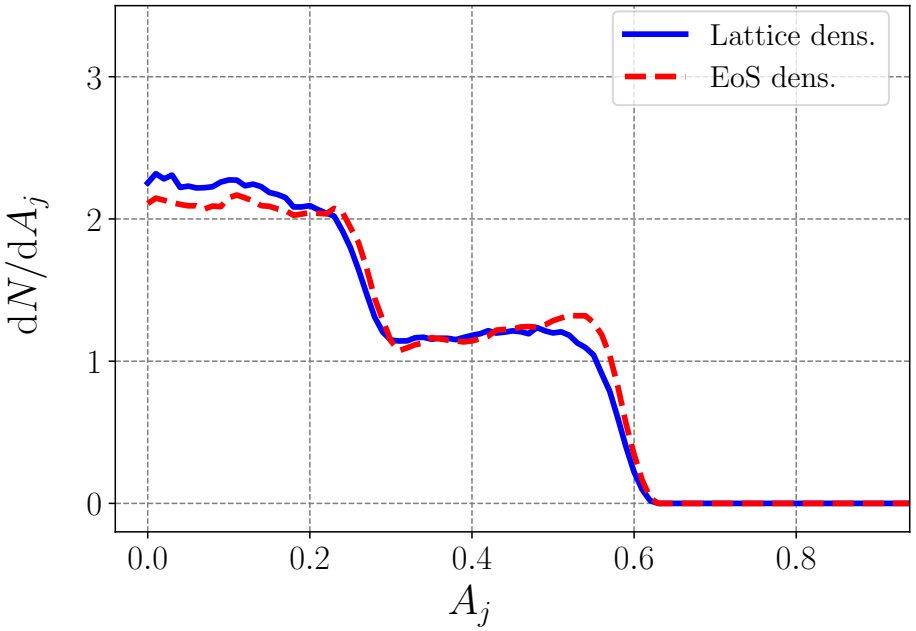

Figure 4.12: Dijet asymmetry of parton jets for 62.4 GeV Au-Au collisions. The (blue) solid curve is the result for monopole density from the lattice, and the (red) dashed curve is the result for monopole density from thermodynamics.

of the lower-energy fireball, and a better understanding of the initial energy spectrum of the produced parton jets.

Nevertheless, we can carry out the simulations to get relatively good predictions, the results of which are seen in Figs. 4.10 and 4.11 for $R_{\rm AA}$ and v_2, respectively. The results of jet quenching with monopoles at 62.4 GeV is very similar to that at 200 GeV; the $R_{\rm AA}$ is slightly smaller and the v_2 is approximately the same.

The deviation between the equation of state and directly-observed lattice monopole densities in the $R_{\rm AA}$ is present in the 62.4 GeV Au-Au collision, as it was in the higher energy collisions – particularly the 2.76 TeV Pb-Pb collision, where one of the densities did not agree with the data. On the other hand, the v_2 is not as sensitive to the monopole density scheme used, which was also the case for the higher energy collisions. The 62.4 GeV (and lower energy) runs at RHIC will help constrain the features of monopole density at temperatures near $T_{\rm c}$, while the 2.76 TeV (and higher energy) collisions at the LHC are helpful in exploring the higher energy limit of the monopole density.

Without monopoles (not shown in the figures), $R_{\rm AA}$ is unity and v_2 is approximately zero across all jet energies. This is due to the fact that at the temperatures produced in 62.4 GeV collisions – the initial matter is slightly above $T_{\rm c}$ –, the quark and gluon densities are small. If the number of quark and gluon degrees of freedom are proportional to the Polyakov loop, then, without monopoles, one would expect very little nuclear modification of the parton jets in 62.4 GeV (and lower energy) collisions.

However, the temperatures produced in these collisions are in the range where monopoles dominate. So, when including monopole contributions, we see a significant nuclear modification, comparable in magnitude to higher energy collisions. Therefore, if the data from the BES program show that there is significant medium-induced modification of parton jets, this will indicate that the near-$T_{\rm c}$ scatterings on matter are strong. This data will also help constrain the shape of the monopole density curve and its peak, which, as we have shown, has a significant influence on the results of our model.

Fig. 4.12 shows a predicted dijet asymmetry (with no cut) for the 62.4 GeV Au-Au collisions. As shown above, the Glauber initial conditions do not reproduce the LHC dijet asymmetry data well, while the fluctuating initial conditions have a decent agreement. Therefore, to accurately predict the 62.4 GeV Au-Au dijet asymmetry, we would need a more realistic, fluctuating hydrodynamic background with a $p_\perp$ cut to reflect the experimental cuts. Nevertheless, from comparison of Fig. 4.12 with the results for the Glauber initial conditions at higher energies, we predict that the asymmetry peak in 62.4 GeV Au-Au collisions will not be as wide as it is in 200 GeV and 2.76 TeV collisions.

Effects of monopole correlations

The preceding results were all computed using a monopole correlation factor of 0.85 to account for the change in $\hat{q}$ due to correlations of monopoles. In Figs. 4.13 and 4.14, we show the effects of this correlation factor on $R_{\rm AA}$ and v_2, respectively, for 2.76 TeV and 200 GeV collisions. We define,

$$\Delta(\text{Obs.}) = (\text{Obs.})_{\text{corr.}} - (\text{Obs.})_{\text{uncorr.}}\,, \tag{4.21}$$

where (Obs.) is an observable.

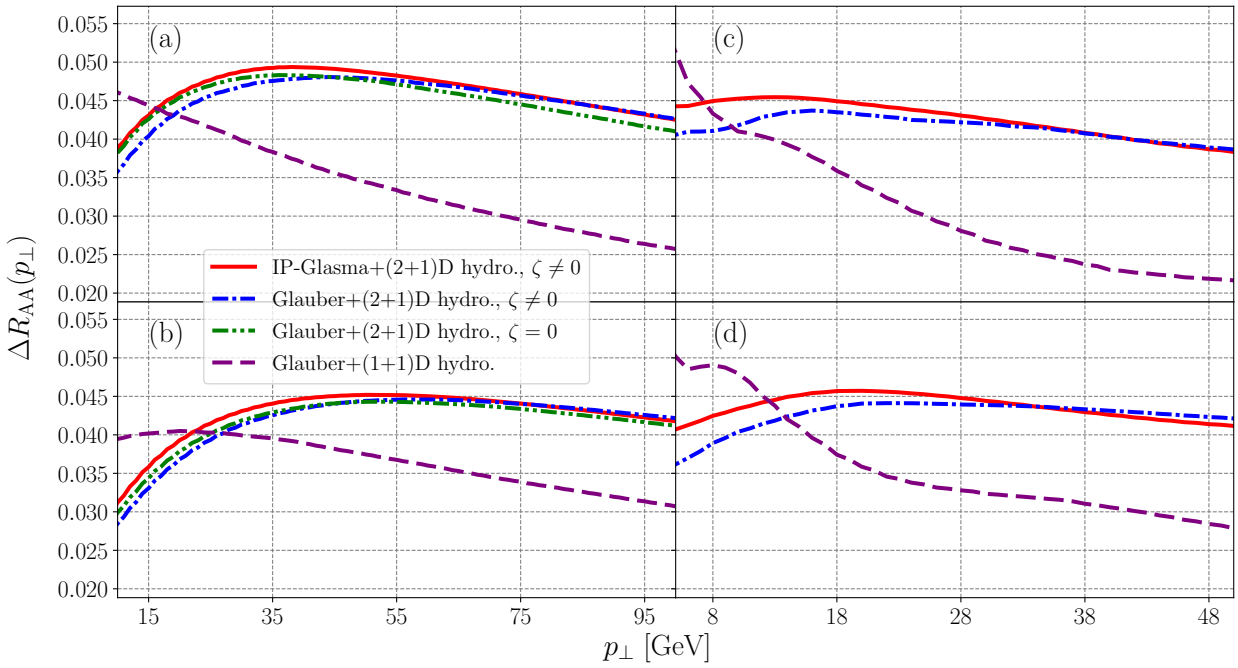

Figure 4.13: The effect of monopole correlations on the nuclear modification factor of charged hadrons in 2.76 Pb-Pb collisions (a),(b), and neutral pions in 200 GeV Au-Au collisions (c),(d). The first row (a),(c) is the results for monopole density from the lattice, while the second row (b),(d) is results for monopole density from the equation of state. The (red) solid curve is for IP-Glasma initial conditions and (2+1)D hydrodynamics with bulk viscosity ($\zeta \neq 0$), the (blue) dash-dot curve is for Glauber initial conditions and (2+1)D hydrodynamics with bulk viscosity ($\zeta \neq 0$), the (green) dash-dot-dot curve is for Glauber initial conditions and (2+1)D hydrodynamics without bulk viscosity ($\zeta = 0$), and the (purple) dashed curve is for the smooth Glauber initial condition with (1+1)D Bjorken evolution.

We see that, in general, correlations of monopoles cause the $R_{\rm AA}$ to increase and the v_2 to decrease. Also, we see that, for all realistic initial conditions and hydrodynamic evolutions, the monopole correlations have approximately the same effect, and that the magnitude of the effect is on the order of 10%.

4.4 Summary

We have described various aspects of jet quenching phenomena using the BDMPS formalism, including not only scattering on electric quasiparticles, quarks and gluons, but scattering on monopoles as well. Unlike previous works by others, we include densities of all quasiparticles from certain common fit to lattice thermodynamics, so there are no free parameters in the theory.

The calculated observables include the nuclear modification factor $R_{\rm AA}$, the azimuthal asymmetry v_2, and dijet asymmetry A_j; this is done both for RHIC and LHC energies. The

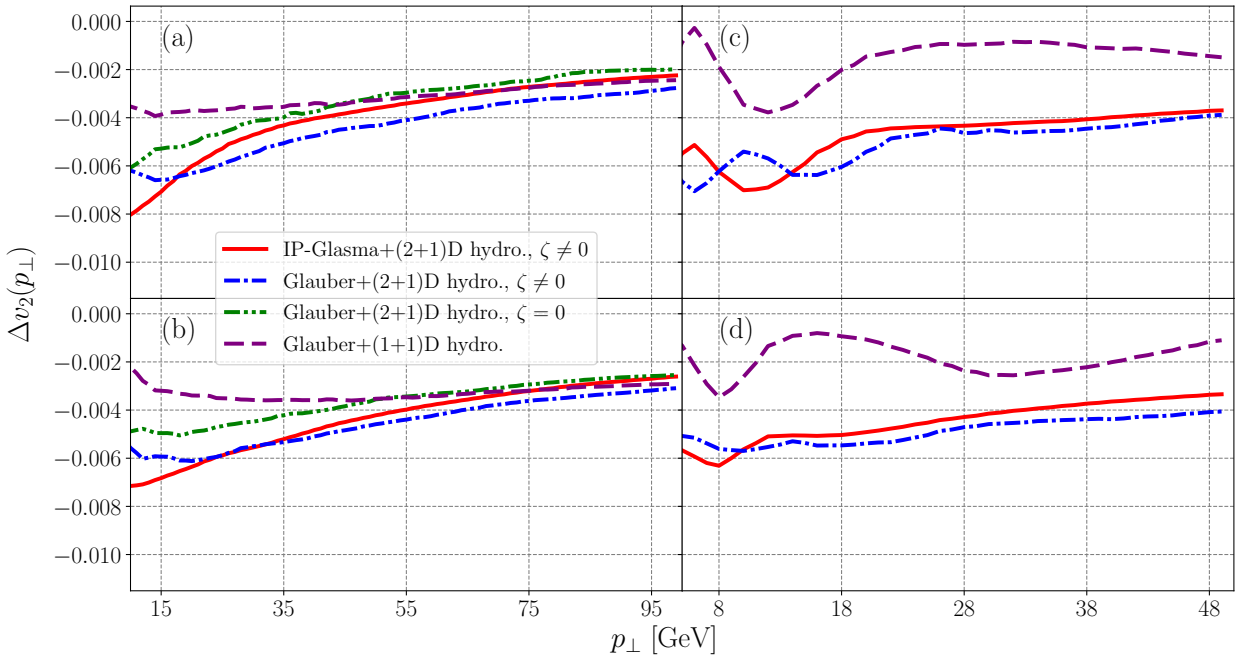

Figure 4.14: The effect of monopole correlations on the azimuthal anisotropy of charged hadrons in 2.76 Pb-Pb collisions (a),(b), and neutral pions in 200 GeV Au-Au collisions (c),(d). The first row (a),(c) is the results for monopole density from the lattice, while the second row (b),(d) is results for monopole density from the equation of state. The (red) solid curve is for IP-Glasma initial conditions and (2+1)D hydrodynamics with bulk viscosity ($\zeta \neq 0$), the (blue) dash-dot curve is for Glauber initial conditions and (2+1)D hydrodynamics with bulk viscosity ($\zeta \neq 0$), the (green) dash-dot-dot curve is for Glauber initial conditions and (2+1)D hydrodynamics without bulk viscosity ($\zeta = 0$), and the (purple) dashed curve is for the smooth Glauber initial condition with (1+1)D Bjorken evolution.

main conclusion of the work is that the current model provides rather reasonable description of all of them. We find that, while realistic hydrodynamics is necessary for good agreement with the observables seen in experiment, account for event-by-event fluctuations is not necessary for reproducing $R_{\rm AA}$ and v_2 data; fluctuations, however, seem to play a role in A_j. In all cases, the contribution of the monopoles is crucial for the success of the model.

In our model, monopoles give the dominant contributions to these observables at lower RHIC energies, e.g. 62.4 GeV, where quarks and gluons provide almost no quenching. Experimental observation of $R_{\rm AA}$, v_2, and A_j at lower energies that deviate from the pp results would bolster the proposition of the magnetic scenario above T_c.

Still, the model in its current form has certain limitations, which need to be addressed in further studies. The model itself is that of independent scattering on "scatterers," which is of course an approximation. While we tried to remedy this partly by including monopole correlation corrections, clearly the system is a strongly coupled plasma, and more work is needed to include scattering effects more accurately.

We realize that the model we are using is missing some physical processes, as it only

has radiative effects to lowest order, and neglects elastic and quasi-elastic scattering which believed to be necessary for quenching of jets with heavy c, b quarks. Note that the recoil energy by scatterers is neglected; this, however, is only true if scatterers are heavy. In fact, the efficiency of such processes depend on quasiparticle masses, and that in the near-T_c region the monopoles are believed to be the lightest ones, thus contributing more to the elastic energy loss. We hope to return to this issue in subsequent work.

Chapter 5

Chiral Symmetry Breaking

This chapter if based on:

- A. Ramamurti and E. Shuryak (2018). Chiral symmetry breaking and monopoles in gauge theories. Phys. Rev. **D**, under peer review. arXiv:1801.06922.

While the central role of monopoles in the confinement-deconfinement transition was recognized long ago, their relation to another important non-perturbative aspect of QCD-like theories, chiral symmetry breaking, has attracted much less attention. It has been found on the lattice that, by decomposing the gauge fields into Abelian-monopole, Abelian-plain, and non-Abelian components, the removal of the monopoles does indeed lead to removal of the quark condensate [146, 147].

In this chapter, we address how chiral symmetry breaking and the generation of the non-zero quark condensate at $T < T_c$ can be explained in terms of this monopole model. The mechanism is based on the formation of bound states between quarks and monopoles. Like in condensed matter systems, in which "doping" of a material by atoms with an extra state leads to new set of states and alters its conductivity, the presence of monopoles radically affects the Dirac eigenvalue spectrum.

One obvious difficulty of the problem is the fact that a detailed understanding of the "lattice monopoles" is lacking; they are treated as effective objects whose parameters and behavior we can observe on the lattice and parameterize, but their microscopic structure has yet to be understood. In particular, the 't Hooft-Polyakov monopole solution includes a chiral-symmetry-breaking scalar field, while we know that, in massless QCD-like theories, chiral symmetry is locally unbroken. We assume that the zero modes in question are chiral themselves, like they are in the instanton-dyon theory, and that chiral symmetry breaking can only be achieved by a spontaneous breaking of the symmetry.

The other difficulty of the problem is the important distinction between fermionic zero modes of (i) monopoles and (ii) instanton-dyons. The latter include the so called L-type or twisted dyons, which possess 4-dimensional zero modes for antisymmetric fermions. Therefore, their collectivization naturally leads to chiral symmetry breaking, studied recently in Ref. [91], in a natural mechanism originally proposed for the instantons; for a review, see Ref. [148]. As follows from Banks-Casher relation [149], the quark condensate is proportional to density of Dirac eigenstates at zero eigenvalue.

The monopoles also have fermionic zero modes [116], which are 3-dimensional. They are, therefore, simply a bound state of a fermion and a monopole. In theories with extended supersymmetries, such objects do exist, fulfilling an important general requirement that monopoles need to come in particular super-multiplets, with fermionic spin 1/2 for $\mathcal{N}=2$, or spins 1/2 and 1 for $\mathcal{N}=4$. The anti-periodic boundary conditions for fermions in Matsubara time implies certain time dependence of the quark fields, and (as we will discuss in detail below) the lowest 4-dimensional Dirac eigenvalues produced by quarks bound to monopoles are the values $\lambda=\pm\pi T$, not at zero.

This, however, is only true for a single monopole. In a monopole *ensemble* with non-zero density, the monopole-quark bound states are collectivized and Dirac eigenvalue spectrum is modified. The question is whether this effect can lead to a nonzero $\rho(\lambda=0)\propto\langle\bar{q}q\rangle$, and if so, whether it happens at the temperature at which chiral symmetry breaking is observed. As we will show below, we find affirmative answers to both these questions. The phenomenological monopole model parameters are such that a non-zero quark condensate is generated by monopoles at $T\approx T_c$.

As a final introductory comment, we note that our approach is to take as inputs the empirical monopole density $n(T)$ and ensemble of paths from our previous study. Using them, we calculate the corresponding Dirac eigenvalue spectrum. The back-reaction of the fermions on monopole density and their motion is neglected. In this respect, our calculation is ideological similar to *quenched* lattice calculations, which also ignore quark back-reaction on the gauge fields.

5.1 Georgi-Glashow Model with Fermions

In this section, we will overview the calculation of the fermion-monopole zero modes in the Georgi-Glashow model (see Sec. 1.1.2 for a review of monopoles in the Georgi-Glashow model). First, we will remind the reader of the result found by Jackiw and Rebbi [116] for the fermionic zero modes, and then go on to compute the matrix element between two monopoles in the basis of zero modes.

5.1.1 Fermionic Zero Modes of Monopoles

We will begin by summarizing known results from Refs. [116, 150].The Lagrangian of the Georgi-Glashow model (without fermions) is

$$\mathcal{L}=-\frac{1}{4}F_a^{\mu\nu}F_{a\mu\nu}+\frac{1}{2}(D_\mu\phi)_a(D^\mu\phi)_a-\frac{1}{4}\lambda(\phi_a\phi_a-v^2) \tag{5.1}$$

where

$$F_a^{\mu\nu}=\partial^\mu A_a^\nu-\partial^\nu A_a^\mu+g\epsilon_{abc}A_b^\mu A_c^\nu\,,$$

and

$$(D^\mu\phi)_a=\partial^\mu\phi_a+g\epsilon_{abc}A_b^\mu\phi_c\,.$$

The fermionic part considered by Jackiw and Rebbi is

$$\mathcal{L}_\mathcal{F}=i\bar{\psi}_n\gamma^\mu(D_\mu\psi)_n-Gg\bar{\psi}_n\tau^a_{nm}\psi_m\phi_a\,, \tag{5.2}$$

with G a constant, $\tau^a = \sigma^a/2$, and

$$(D_\mu \psi)_n = \partial^\mu \psi_n - ig\tau^a_{nm} A^\mu_a \psi_m \,.$$

The Dirac equation for the fermion field is written in the form

$$\Big[-i\vec{\alpha}\cdot\vec{\partial}\delta_{nm} + \frac{1}{2}A(r)\sigma^a_{nm}(\vec{\alpha}\times\vec{\hat{r}})_a + \frac{G\phi(r)}{2}\sigma^a_{nm}\hat{r}_a\beta\Big]\psi_m = E\psi_n \,, \tag{5.3}$$

where $n, m = 1, 2$ are the isospin indices, σ^a are the Pauli matrices, and

$$\alpha_i = \begin{pmatrix} 0 & \sigma_i \\ \sigma_i & 0 \end{pmatrix} , \qquad \beta = -i\begin{pmatrix} 0 & \mathbb{1} \\ -\mathbb{1} & 0 \end{pmatrix} . \tag{5.4}$$

For clarity, let us take a brief aside to discuss the basis of gamma matrices we use. The representation of the Dirac matrices used by Jackiw and Rebbi correspond to the definition

$$\gamma_4 = \beta \,, \qquad \gamma_4\vec{\gamma} = -i\vec{\alpha} \,, \tag{5.5}$$

with the representation of the gamma matrices

$$\gamma_4 = -i\begin{pmatrix} 0 & \mathbb{1} \\ -\mathbb{1} & 0 \end{pmatrix} , \quad \gamma_i = \begin{pmatrix} -\sigma_i & 0 \\ 0 & \sigma_i \end{pmatrix} , \quad \gamma_5 = i\begin{pmatrix} 0 & \mathbb{1} \\ \mathbb{1} & 0 \end{pmatrix} . \tag{5.6}$$

Note that this form is different both from the standard Dirac representation

$$\gamma_0 = \begin{pmatrix} \mathbb{1} & 0 \\ 0 & -\mathbb{1} \end{pmatrix} , \quad \gamma_i = \begin{pmatrix} 0 & \sigma_i \\ -\sigma_i & 0 \end{pmatrix} , \quad \gamma_5 = \begin{pmatrix} 0 & \mathbb{1} \\ \mathbb{1} & 0 \end{pmatrix} , \tag{5.7}$$

and the Weyl one, in which

$$\gamma_0 = \begin{pmatrix} 0 & \mathbb{1} \\ \mathbb{1} & 0 \end{pmatrix} , \quad \gamma_i = \begin{pmatrix} 0 & \sigma_i \\ -\sigma_i & 0 \end{pmatrix} , \quad \gamma_5 = \begin{pmatrix} -\mathbb{1} & 0 \\ 0 & \mathbb{1} \end{pmatrix} . \tag{5.8}$$

The standard definition of fermion chirality (left and right polarizations) is related to projectors $(1 \pm \gamma_5)/2$, and so only the last Weyl representation, in which γ_5 is diagonal, is really chiral. The zero modes of pure gauge solitons, such as instantons and instanton-dyons, are chiral in this standard sense.

The 2-component zero modes found by Jackiw and Rebbi are often called "chiral" in literature, but they are *not* chiral in the standard sense, as seen already from the fact that in their representation γ_5 is *not* diagonal. Furthermore, as seen directly from the Lagrangian of the Georgi-Glashow model, fermions interact with a scalar field, and this vertex mixes the left and right polarizations, explicitly breaking chiral symmetry.

In pure gauge theory with massless fermions (which we discuss), the SU(N_f) chiral symmetry is exact. So, when the lattice monopoles – whatever their microscopic structure may be – have fermionic bound states, those should belong to the representation of the standard chiral symmetry, rather than the one with the quotation marks. So, while we use the 't

Hooft-Polyakov monopole and its Jackiw-Rebbi zero modes as an example, we do not expect it correctly reproduce their chiral properties. We assume that the zero modes of monopoles in gauge theories without scalars (such as QCD) are truly chiral in the usual sense.

In this representation of the Dirac matrices, the α_i, β are non-diagonal, and the only diagonal term is the energy. For a zero mode $E = 0$, the problem is "chiral," in the sense that the 4-spinor ψ splits into separate upper and lower components,

$$\psi = \begin{pmatrix} \psi^+ \\ \psi^- \end{pmatrix} ,$$

where $\psi^\pm_{lm}$ has four components, with l corresponding to spin indices and m corresponding to isospin (The SU(2) color is called isospin in Georgi-Glashow model.) These upper and lower components can be further written as two scalar and vector fields,

$$\psi^\pm_{lm} = (g^\pm \delta_{lm} + \vec{g}^\pm \cdot \vec{\sigma}_{ln})\sigma^2_{nm} .$$

Carrying out the partial wave analysis (see Appendix of Ref. [116]) and finding the zero energy solution gives

$$\begin{aligned} &\vec{g}^\pm(r) = 0, \\ &g^-(r) = c^- \times \exp\left(\int_0^r \mathrm{d}r' \left[A(r') + \frac{1}{2}G\phi(r')\right]\right) , \\ &g^+(r) = c^+ \times \exp\left(\int_0^r \mathrm{d}r' \left[A(r') - \frac{1}{2}G\phi(r')\right]\right) , \end{aligned}$$

The g^- solution is un-normalizable, so it is set to zero ($c^- = 0$). This gives the spinors

$$\begin{aligned} \psi^-_{lm} &= 0 , \\ \psi^+_{lm} &= N \exp\left(\int_0^r \mathrm{d}r' \left[A(r') - \frac{1}{2}G\phi(r')\right]\right) \\ &\quad \times (s^+_l s^-_m - s^-_l s^+_m) , \end{aligned} \tag{5.9}$$

where $s^\pm$ are the eigenvectors of σ^3, and N is a normalization.

The extension of the SU(2) 't Hooft-Polyakov monopole solution to SU(3) – with the same Georgi-Glashow-like Lagrangian – is discussed by A. Sinha [60]. In QCD, the A_0 field plays the role of the scalar (Higgs) field in the Georgi-Glashow model. For the purposes of this work, and for simplicity, we will study only the SU(2) case.

5.1.2 Quark Hopping Matrix

Recognizing fermionic binding to monopoles, we now proceed to description of their dynamics in the presence of ensembles of monopoles. The basis of the description is assumed to be the set of zero modes described in the previous section. The Dirac operator is written as a matrix in this basis, so that $i - j$ element is related to "hopping" between them. Such an approach originated from the "instanton liquid" model [148].

The matrix elements of the "hopping matrix"

$$\mathbf{T} = \begin{pmatrix} 0 & iT_{ij} \\ iT_{ji} & 0 \end{pmatrix} \tag{5.10}$$

where the T_{ij}s are defined as the matrix element,

$$T_{ij} \equiv \langle i| - i\not{D} |j\rangle \,, \tag{5.11}$$

between the zero modes located on monopoles i and antimonopoles j. In the SU(2) case we are considering, this is equivalent to

$$\begin{aligned} T_{ij} &= \langle\psi_i|x\rangle \langle x| - i\not{D} |y\rangle \langle y|\psi_j\rangle \\ &= \int \mathrm{d}^3x \psi^\dagger_{kn}(x-x_i)(-i\not{D})\psi_{lm}(x-x_j) \\ &= \int \mathrm{d}^3x \psi^\dagger_{kn}(x-x_i)\Big[-i(\vec{\alpha}\cdot\vec{\partial} + \vec{\alpha}\cdot\vec{\partial} - \vec{\alpha}\cdot\vec{\partial})\delta_{nm} \\ &\quad + \frac{1}{2}(A(x-x_i) + A(x-x_j))\sigma^a_{nm}(\vec{\alpha}\times\vec{\hat{r}})_a \\ &\quad + \frac{G(\phi(x-x_i)+\phi(x-x_j))}{2}\sigma^a_{nm}\hat{r}_a\beta\Big]\psi_{lm}(x-x_j) \\ &= \int \sum_m \mathrm{d}^3x \psi^\dagger_{km}(x-x_i)[-i\vec{\alpha}\cdot\vec{\partial}]^{kl}\psi_{lm}(x-x_j) \end{aligned} \tag{5.12}$$

where ψs are zero modes with origin at $x_{i,j}$, the locations of the two monopoles, n, m are the isospin/color indices, and we have used the fact that applying the Dirac operator to these wavefunctions gives zero.

The operator between the wavefunctions is

$$\begin{aligned} i\vec{\alpha}\cdot\vec{\partial} = i\begin{pmatrix} 0&0&0&1\\0&0&1&0\\0&1&0&0\\1&0&0&0\end{pmatrix}\partial_x + i\begin{pmatrix} 0&0&0&-i\\0&0&i&0\\0&-i&0&0\\i&0&0&0\end{pmatrix}\partial_y \\ + i\begin{pmatrix} 0&0&1&0\\0&0&0&-1\\1&0&0&0\\0&-1&0&0\end{pmatrix}\partial_z \,. \end{aligned} \tag{5.13}$$

In the case where the original wavefunction only has an upper component, the resulting vector after applying this operator has only the lower component. Therefore, the matrix elements of the "hopping matrix" T_{ij} are zero unless the fermionic zero modes have *opposite* chirality. So, a left-handed fermion zero mode has non-zero overlap with a right-handed zero mode, and vice versa. To get the opposite chirality, we need to change the sign of the couplings. In the case of an SU(2) antimonopole, only the lower spinor survives, with the same wavefunction (the spin of the fermion flips). We will call these zero modes ξ.

This allows us to split the previous equation into two equations,

$$T_{ij} = \int \mathrm{d}^3x \xi^\dagger(x - x_i)[-i\vec{\sigma}\cdot\vec{\partial}]\psi(x - x_j)\,,$$
$$T_{ji} = \int \mathrm{d}^3x \psi^\dagger(x - x_i)[-i\vec{\sigma}\cdot\vec{\partial}]\xi(x - x_j)\,, \tag{5.14}$$

where we use the appropriate one depending on whether $i(j)$ is a location of a monopole(antimonopole).

For the matrix element between a right-handed monopole zero mode and a left-handed anti-monopole zero mode,

$$T_{ij} = \int \mathrm{d}^3\vec{x} \sum_m \xi^\dagger_{km}(\vec{x} - \vec{x}_i)[-i\vec{\sigma}\cdot\vec{\partial}]^{kl}\psi_{lm}(\vec{x} - \vec{x}_j)\,,$$

where m is the traced-over isospin/color index, and k, l are the spin indices (which are all convoluted). The operator is,

$$[-i\vec{\sigma}\cdot\vec{\partial}] = \begin{pmatrix} -i\partial_z & -i\partial_x - \partial_y \\ -i\partial_x + \partial_y & i\partial_z \end{pmatrix}. \tag{5.15}$$

For simplicity, we will treat each isospin/color case separately, so the only indices left are spin indices. We will denote the spatial-only part of the wavefunction (without spinors) with tildes.

$\underline{m = 1}$:

We will write ξ_{k1} as $\tilde{\xi}a_k$ and ψ_{l1} as $\tilde{\psi}a_l$. The wavefunction has spinors

$$a_i \equiv s_i^+ s_1^- - s_i^- s_1^+ = \begin{pmatrix} 0 \\ -1 \end{pmatrix},$$

$$a_i^\dagger \equiv s_1^+ s_i^- - s_1^- s_i^+ = \begin{pmatrix} 1 & 0 \end{pmatrix},$$

and so

$$\tilde{\xi}a_k^\dagger[-i\vec{\sigma}\cdot\vec{\partial}]^{kl}a_l\tilde{\psi} = \tilde{\xi}(i\partial_x + \partial_y)\tilde{\psi}\,. \tag{5.16}$$

$\underline{m = 2}$:

The wavefunction has spinors

$$b_i \equiv s_i^+ s_2^- - s_i^- s_2^+ = \begin{pmatrix} 1 \\ 0 \end{pmatrix},$$

$$b_i^\dagger \equiv s_2^+ s_i^- - s_2^- s_i^+ = \begin{pmatrix} 0 & -1 \end{pmatrix},$$

and so

$$\tilde{\xi}b_k[-i\vec{\sigma}\cdot\vec{\partial}]^{kl}b_l\tilde{\psi} = \tilde{\xi}(i\partial_x - \partial_y)\tilde{\psi}\,. \tag{5.17}$$

Combining the two cases,

$$\sum_m \xi^\dagger_{km}[-i\vec{\sigma}\cdot\vec{\partial}]^{kl}\psi_{lm} = 2i\tilde{\xi}\partial_x\tilde{\psi}\,, \tag{5.18}$$

which then yields that,

$$T_{ij} = 2i\int \mathrm{d}^3\vec{x}\tilde{\xi}(\vec{x}-\vec{x}_i)\partial_x\tilde{\psi}(\vec{x}-\vec{x}_j)\,. \tag{5.19}$$

For the matrix element between a left-handed anti-monopole zero mode and a right-handed monopole zero mode, we get, similarly,

$$T_{ji} = 2i\int \mathrm{d}^3\vec{x}\tilde{\psi}(\vec{x}-\vec{x}_i)\partial_x\tilde{\xi}(\vec{x}-\vec{x}_j)\,.$$

The full solutions to the equations of motion for $A(r)$ and $\phi(r)$ are well behaved at the origin, so we must use those in lieu of only considering asymptotics. The only analytic solution to the equations of motion is in the case where $\lambda = 0$; this solution is known as the Bogomolnyi-Prasad-Sommerfeld (BPS) monopole [58, 59]. In this case,

$$\begin{aligned} H(\zeta) &= \zeta\coth(\zeta) - 1\,, \\ K(\zeta) &= \frac{\zeta}{\sinh(\zeta)}\,, \end{aligned} \tag{5.20}$$

where $\zeta = gvr$. In terms of these functions, our gauge fields are,

$$\begin{aligned} A^0_a &= 0\,, \\ A^i_a &= \epsilon^{aij}\frac{r_j}{gr^2}(1-K(\zeta))\,, \\ \phi_a &= \frac{r_a}{gr^2}H(\zeta)\,. \end{aligned} \tag{5.21}$$

This leads to the identification with our earlier notation,

$$\begin{aligned} A(r) &= \frac{1-K(gvr)}{r}\,, \\ \phi(r) &= \frac{H(gvr)}{r}\,. \end{aligned} \tag{5.22}$$

For the monopole zero mode we get that, up to normalization,

$$\tilde{\psi} = \frac{1}{2}(gvr)^{\frac{G}{2}+1}\coth\left(\frac{gvr}{2}\right)\sinh^{-\frac{G}{2}}(gvr)\,. \tag{5.23}$$

Then,

$$\begin{aligned} \partial_x\tilde{\psi} = &-\left(\frac{x}{4r^2}\right)(gvr)^{\frac{G}{2}+1}\coth\left(\frac{1}{2}gvr\right)\sinh^{-\frac{G}{2}-1}(gvr) \\ &\times\left(-(G+2)\sinh(gvr) + gGvr\cosh(gvr) + 2gvr\right)\,, \end{aligned} \tag{5.24}$$

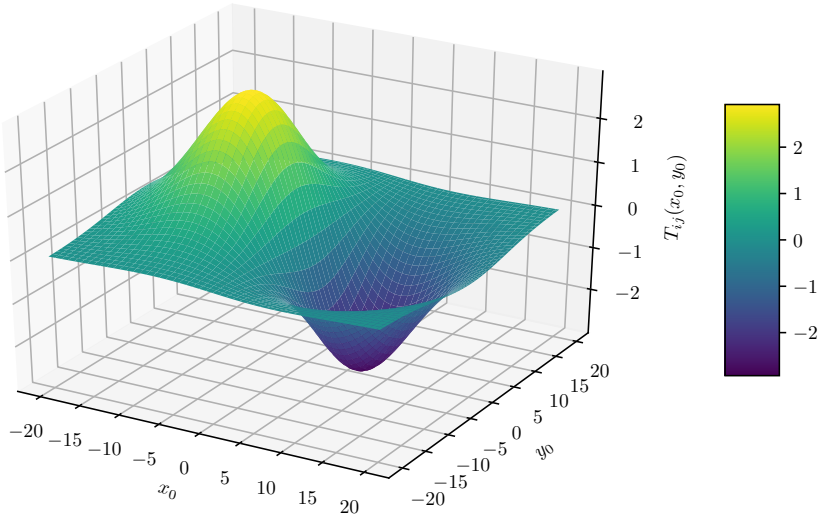

Figure 5.1: Evaluation of $\mathrm{Im}(T_{ij}(r_0))$ for r_0 in the xy plane for $G = g = v = 1$.

and similarly for the anti-monopole zero mode wave function. Putting these solutions into the hopping matrix element equation for monopole-to-antimonopole, we get

$$\begin{aligned} T_{ij}(r_0) =& 2i \int \mathrm{d}^3\vec{x}\tilde{\xi}(|r - r_0|)\partial_x\tilde{\psi}(r) \\ =& 2iN^2 \int \mathrm{d}^3\vec{x} \left(-\frac{x}{8r^2}\right) (gv)^{G+2} r^{\frac{G+2}{2}} |r - r_0|^{\frac{G+2}{2}} \\ & \times \coth\left(\frac{1}{2}gvr\right) \sinh^{-\frac{G}{2}-1}(gvr) \\ & \times \coth\left(\frac{1}{2}gv|r - r_0|\right) \sinh^{-\frac{G}{2}}(gv|r - r_0|) \\ & \times \left(-(G+2)\sinh(gvr) + gGvr\cosh(gvr) + 2gvr\right) . \end{aligned} \tag{5.25}$$

The combination gvr is dimensionless, as is x/r, so the integrand has dimension [energy] $(1/r)$. The parameter v, in the BPS limit, is determined by the mass of the monopole, and g is taken to be the same as in the strong coupling constant.

As an instructive exercise, taking $G, g, v = 1$, we can evaluate this integral. The result is seen in Fig. 5.1. The first thing to note is that the result of integral is symmetric around the x-axis, and therefore only dependent on the combination $(y_0^2 + z_0^2)$. So, for example, taking $r_0 = (x_0, 2, 3)$ yields the same result as $r_0 = (x_0, \sqrt{13}, 0)$, $r_0 = (x_0, 3, 2)$, etc. In addition, the function is odd under reflection from $x \to -x$. Therefore, we can evaluate the integral with $z_0 = 0$, $y_0 \geq 0$, and $x_0 \geq 0$, without loss of generality.

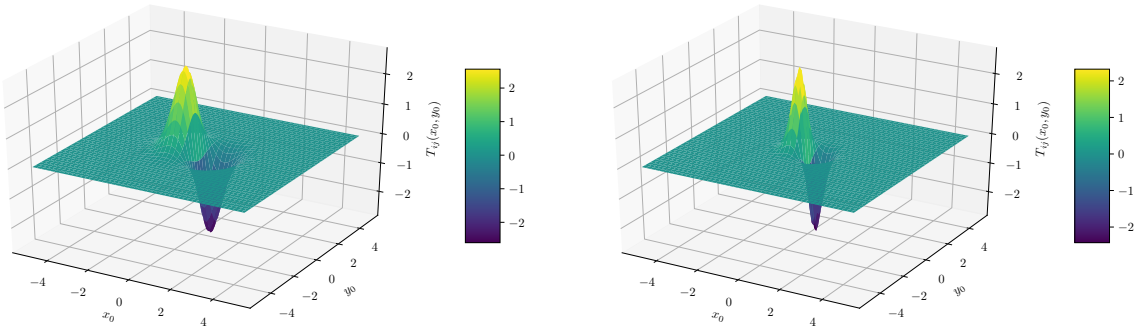

(a) $T = 1T_c$ (b) $T = 1.05T_c$

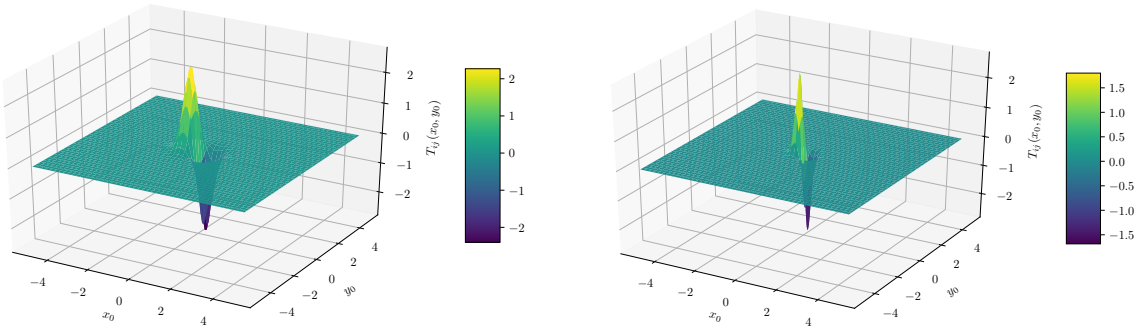

(c) $T = 1.1T_c$ (d) $T = 1.2T_c$

Figure 5.2: Evaluation of $\mathrm{Im}(T_{ij}(r_0))$ for r_0 in the xy plane for different temperatures.

5.2 Dirac Eigenvalue Distributions

We will use the monopole configurations found in our previous path-integral study of monopole Bose-Einstein condensation, and study the effects of density and temperature on the eigenvalue spectrum of the Dirac operator for BPS monopoles.

To constrain the values of g and v, we can use the mass of the monopole. In the BPS limit, the mass is given by

$$M = \frac{4\pi v}{g}\,. \tag{5.26}$$

The mass of the monopole was studied in Ref. [64] through lattice simulations of SU(2) pure-gauge theory, which shows a mass of around $2T_c$ at $T = T_c$, and then rapidly grows as temperature increases. The density of monopoles in SU(2) gauge theories was studied in Ref. [115], and was parameterized by

$$\frac{\rho}{T_c^3}\left(\frac{T}{T_c}\right) = \frac{0.557(T/T_c)^3}{\log(2.69(T/T_c))^2}\,. \tag{5.27}$$

We will evaluate the *evolution matrix* U, defined as time-ordered integral of the hopping matrix in the previous section over the Matsubara periodic time $\tau \in [0, \beta]$. This matrix will then be diagonalized to find the eigenvalues for the fermion states. Because each eigenstate

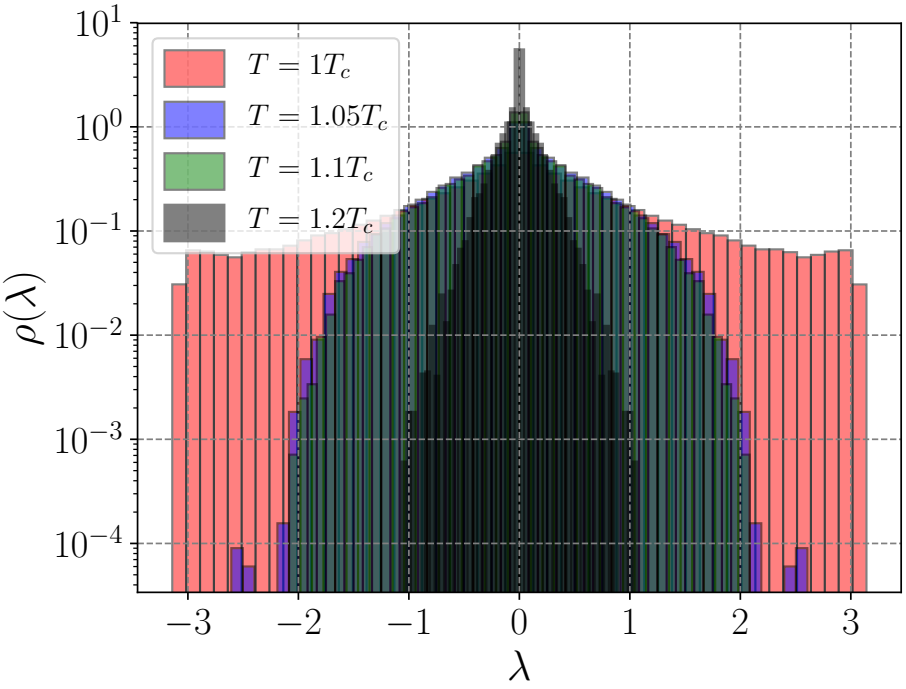

Figure 5.3: Eigenvalue distribution for $T/T_c = 1$ (red), 1.1 (blue), and 1.2 (green). Note the logarithmic scale.

is still fermionic, each is required to fulfill the fermionic boundary conditions, namely that the state must return to minus itself after one rotation around the Matsubara circle. This defines quantization of the Dirac eigenvalues by,

$$\lambda_i + \omega_{i,n} = \left(n + \frac{1}{2}\right) \frac{2\pi}{\beta}\,, \tag{5.28}$$

where λ_is are the eigenvalues of the hopping matrix $\mathbf{T}$.

For monopoles that move in Euclidean time, we must integrate over the Matsubara circle to find the fermion frequencies,

$$U = \oint_\beta d\tau e^{iH\tau} = -\mathbb{1}\,. \tag{5.29}$$

This can be approximated by

$$\begin{aligned} -\mathbb{1} &\approx e^{iH_m\Delta\tau} \dots e^{iH_2\Delta\tau} e^{iH_1\Delta\tau} \\ &\approx (1 + iH_m\Delta\tau - \dots) \dots (1 + iH_1\Delta\tau - \dots) \end{aligned}$$

for m time slices. We diagonalize the resulting matrix on the right-hand side and solve to find the quantity $\lambda + \omega$.

For simplicity, we will work in units of T_c (i.e. $T_c = 1$) when doing this calculation (for mass and temperature, for example), and units of length will be defined by the density of monopoles $r \sim \rho^{-1/3}$ in units of $1/T_c$.

Before we begin, to estimate what the effects of temperature will be on our results, we can evaluate the integral in Eq. (5.25) with different values of the parameters, corresponding to the range of temperatures we will simulate. We will take $G = g = \sqrt{4\pi/3}$ – as would be the case in QCD – and v from the monopole mass, taken from Ref. [64]. The results for $T/T_c = 1$, 1.05, 1.1, and 1.2 are seen in Fig. 5.2 (a), (b), (c), and (d), respectively.

Compared to the $g = G = v = 1$ case, the range of the zero-mode hopping is significantly smaller – ∼10 units of length in x_0 to a peak for the former case and 2.5 for $T = T_c$ – and decreases rapidly with temperature. In addition, the peaks of the function reduce in magnitude and very quickly become much sharper as temperature is increased. Therefore, the contribution to the T_{ij} matrix at temperatures above T_c will only come from "local" hopping (i.e. only when there is a monopole-antimonopole molecular bound state), while at T_c, the *ensemble* contributes and there can be a chain of hopping.

To make this explicit, we construct the hopping matrix, as described above, for SU(2) monopole configurations at $T/T_c = 1$, 1.05, 1.1, 1.2 and 1.5, and calculate the eigenvalue spectra of the Dirac operator at each of those temperatures. For each of the temperatures, we take 400 path configurations of 32 time slices, each with 32 particles in a box with periodic boundary conditions – the box is repeated to the extent necessary to study the whole range of x_0, y_0, z_0. At each time slice, the hopping matrix is calculated; the matrices are then path-exponentiated to get the hopping matrix for the ensemble configuration.

The spectral density of eigenvalues is given by

$$\rho(\lambda) = \frac{1}{V}\sum_i \delta(\lambda - \lambda_i)\,. \tag{5.30}$$

The eigenvalues of the configurations – before imposing the fermion boundary conditions – are seen in Fig. 5.3. We can then compute the eigenvalues of the Dirac operator with

$$\omega_{i,n} = \left(n + \frac{1}{2}\right)\frac{2\pi}{\beta} - \lambda_i\,. \tag{5.31}$$

Considering only the $n = \pm 1$ case, so that $\omega_i = \pm\pi T - \lambda_i$, we get the distributions shown in Fig. 5.4 (a), (b), (c), and (d) for $T/T_c = 1$, 1.05, 1.1, and 1.2, respectively.

The Banks-Casher relation [149] makes the connection between the density of eigenvalues at $\omega = 0$ and the magnitude of the chiral condensate. In studying the monopole contribution to the chiral condensate, it is important to note that we can only approach the critical temperature T_c from above, as we do not have any lattice data on monopole density, mass, or correlations below T_c. As a result, we will primarily focus on the gap in eigenvalue spectrum around $\omega = 0$ as a proxy for the chiral transition.

The first, and most important, thing to notice is that when $T = T_c$, the eigenvalue distribution has a finite density at $\omega = 0$ (see Fig. 5.4a), which indicates the nonzero value of the chiral condensate; there is no gap in the spectrum present at $T = T_c$. (A small dip seen around zero is a consequence of finite size of the system, well known and studied on the lattice and in topological models. It should be essentially ignored in extrapolation to zero.)

Furthermore, one can see the onset of non-zero density at zero eigenvalue by looking at the smallest eigenvalue in each configuration. Fig. 5.5 shows the mean smallest eigenvalue as a function of temperature. We fit the data with the function

$$\langle\omega_{\rm min}\rangle = A(T - T_c)^\nu\,, \tag{5.32}$$

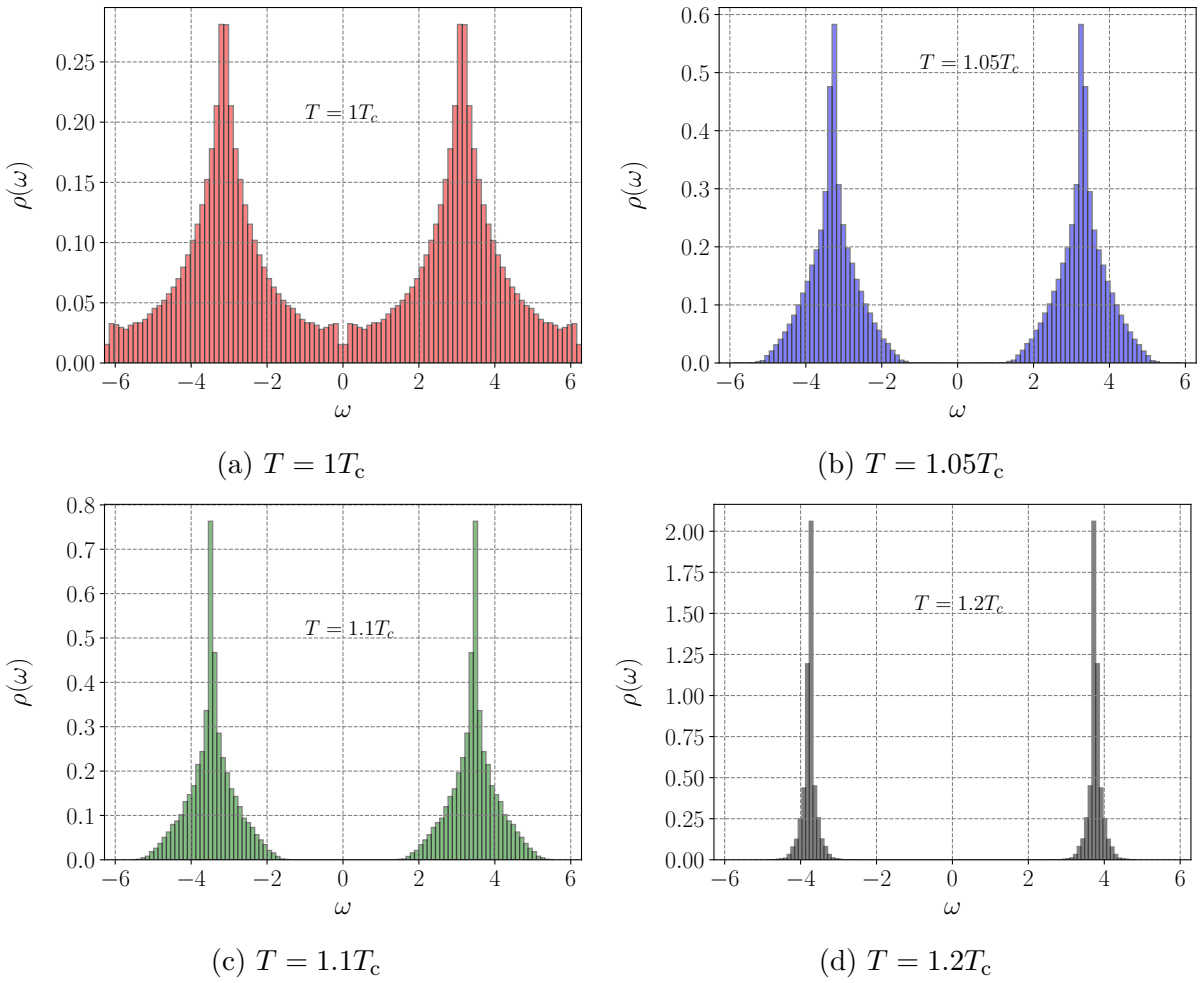

(a) $T = 1T_c$ (b) $T = 1.05T_c$

(c) $T = 1.1T_c$ (d) $T = 1.2T_c$

Figure 5.4: Distributions of Dirac eigenvalues for T/T_c = (a) 1 , (b) 1.05 , (c) 1.1, and (d) 1.2, respectively.

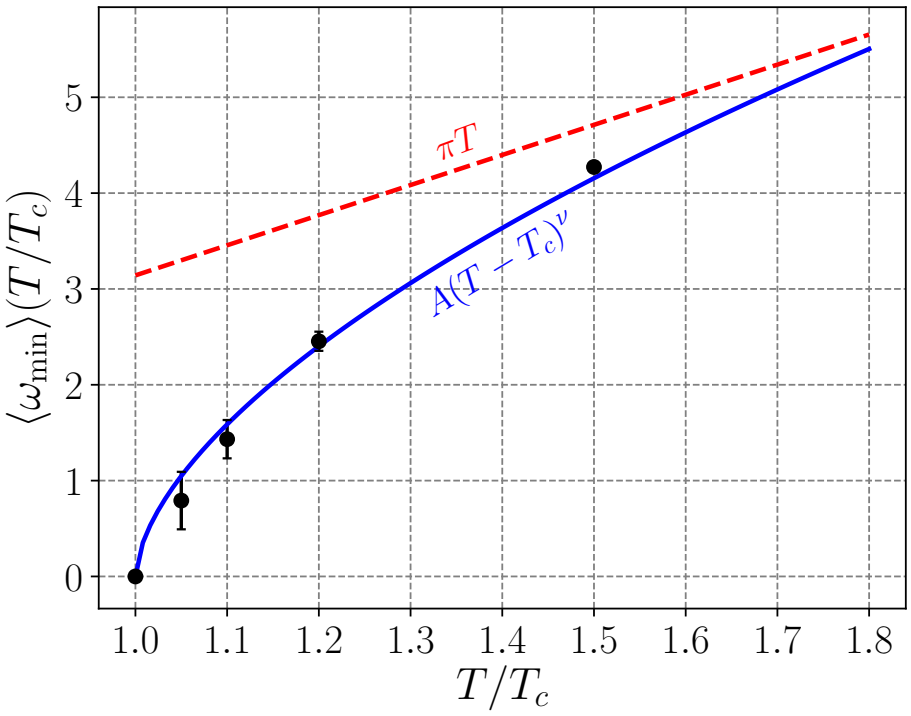

Figure 5.5: Minimum Dirac eigenvalue as a function of temperature. The black dots are values from our simulations, the blue line is the fit $A(T-T_c)^\nu$, and the red dashed line is πT.

where $\langle\ldots\rangle$ indicates an average over configurations. The fit parameters were found to be $A = 6.29$ and $\nu = .60$. We note that this exponent ν is compatible with the critical exponent found from the diverging correlation length at the deconfinement temperature, which for the 3d Ising model is $\nu \approx .63$, and is also consistent with the monopole BEC transition found in Ref. [64]. This agreement was in fact not expected, because of quenched nature of the calculation, but has been observed nevertheless.

5.3 Summary

In qualitative terms, the mechanism of chiral symmetry breaking based on monopoles is as follows. A single monopole (or anti-monopole) generates additional quark and antiquark bound states. At high temperatures, the monopoles have large mass and the probability of hopping is therefore low. The 4d Dirac operator eigenvalues are well localized near the fermionic Matsubara frequencies $2\pi T(n+1/2)$. Using the condensed matter analogy, one may say that a matter is an insulator.

However, as T decreases toward T_c, the amplitudes of quark "hopping" from one monopole to an antimonopole (and vice versa) grow. Eventually, at some critical density, quarks become "collectivized" and are able to travel very far from their original locations. The physics of the mechanism is similar to insulator-metal transition in condensed matter under

pressure.

Technically, the central point is the distinction between the evolution operator and quantization of the fermionic states on one hand, and the Dirac operator and its eigenvalues.

Quantitatively, we found that not only the mechanism works in principle, but that a noticeable quark condensate does appear at $T \approx T_c$, practically simultaneously with the deconfinement phase transition, seen by the BEC of monopoles. This observation is consistent with what what has been observed in quenched lattice calculations.

Finally, let us comment on the dependence of chiral symmetry breaking on the fermion periodicity phase. We have not studied it in this work, but note that for *periodic* quarks, the Matsubara frequencies shift to bosonic set $2\pi Tn$, including $n = 0$. Therefore the monopoles would produce a non-zero quark condensate at *any* density. This comment implies that the chiral transition is in general some function of the periodicity phase, and its coincidence with deconfinement only happens for the anti-periodic quarks we studied.

Chapter 6

Conclusions

In this dissertation, we have presented novel results that have furthered our understanding of the role that chromo-magnetic monopoles play in QCD. Monopoles have been suggested to have a major influence on phenomena ranging from purely non-perturbative, such as chiral symmetry breaking and confinement, to real-time, such as jet quenching.

In Chapter 2, we looked at the question of whether we can analytically understand monopoles in pure gauge theories. In supersymmetric theories, there exist analytic descriptions of both instanton-dyons as well as monopoles, and it was shown that the partition for the former was equivalent to that of the latter through a Poisson transformation. In our work, working up from a simple toy model of a rotator, we considered the partition function of instanton-dyons in pure gauge theory, which can be viewed as periodic winding paths in Euclidean time, and transformed it to its dual form. We argued that this dual form represents the partition function of moving and rotating monopoles.

In Chapter 3, we constructed an effective quantum model for the monopoles found in SU(2) lattice gauge theory simulations, based on a two-component Coulomb Bose gas. We implemented the path-integral Monte Carlo algorithm, and used this to simulate liquid ^{4}He, one-component, and two-component Coulomb gases. In doing so, we were able to test new methods for finding the critical temperature, based on studying the permutation cycle statistics, and found that they both gave good agreement with the classic technique of studying the superfluid fraction. After matching radial correlation functions to those found on the lattice, we were able to find a parameter set for our model that accurately reproduced the properties of lattice monopoles. Using these parameters, we were able to extract the monopoles' contribution to the QCD equation of state, and found that monopoles contribute nearly all of the energy density in the range $1 - 1.3T_c$.

Next, in Chapter 4, we investigated the influence of monopoles on jet quenching. Using the BDMPS model of jet quenching, we studied the effect of monopoles on the energy loss of jets traversing a heavy-ion collision. We found that, when using realistic hydrodynamic backgrounds, we were able to reproduce the experimental trends for the nuclear modification factor, azimuthal anisotropy, and dijet asymmetry observables for 2.76 TeV Pb-Pb and 200 GeV Au-Au collisions. Furthermore, we were able to make predictions for lower energy collisions to occur at RHIC in the future.

Finally, in Chapter 5, we studied the phenomena of chiral symmetry breaking, focused on whether the formation of a chiral condensate could be explained using fermionic zero modes

of monopoles. Using the configurations of monopoles from our effective model, we were able to study the zero modes of fermions and their "hopping" from monopole to anti-monopole. This hopping creates a spread in the Dirac eigenvalue spectrum from the standard Matsubara frequencies. We found that, at the critical temperature, the density of zero-eigenvalue is finite, indicating the existence of a chiral condensate.

Moving forward, lattice QCD studies (with light quarks) – similar to those done for pure-gauge theories in which monopoles and their paths were identified – are necessary to more accurately assess their contributions to properties of QCD and to fully understand phenomena that require fermions. Further investigations of real-time processes that are influenced by monopoles could yield an experimental observable that indicates their presence, and inclusion of monopoles in other more-developed jet quenching models could allow study of further jet observables and substructure. There is, of course, much more work to be done to understand monopoles in QCD, and hopefully, we are only scratching the surface.

Bibliography

[1] M. E. Peskin and D. V. Schroeder (1995). An Introduction to quantum field theory. Addison-Wesley, Reading, USA. ISBN 9780201503975, 0201503972. URL http://www.slac.stanford.edu/~mpeskin/QFT.html.

[2] C.-N. Yang and R. L. Mills (1954). Conservation of Isotopic Spin and Isotopic Gauge Invariance. Phys. Rev. **96**, 191. doi:10.1103/PhysRev.96.191 [,150(1954)].

[3] H. D. Politzer (1973). Reliable Perturbative Results for Strong Interactions? Phys. Rev. Lett. **30**, 1346. doi:10.1103/PhysRevLett.30.1346 [,274(1973)].

[4] D. J. Gross and F. Wilczek (1973). Ultraviolet Behavior of Nonabelian Gauge Theories. Phys. Rev. Lett. **30**, 1343. doi:10.1103/PhysRevLett.30.1343 [,271(1973)].

[5] K. G. Wilson (1974). Confinement of Quarks. Phys. Rev. **D10**, 2445. doi:10.1103/PhysRevD.10.2445 [,319(1974)].

[6] S. Mandelstam (1976). Vortices and Quark Confinement in Nonabelian Gauge Theories. Phys. Rept. **23**, 245. doi:10.1016/0370-1573(76)90043-0

[7] G. 't Hooft (1975). Gauge Fields with Unified Weak, Electromagnetic, and Strong Interactions. In High-Energy Physics: Proceedings, EPS International Conference, Palermo, Italy, 23-28 June 1975., p. 1225.

[8] S. Bethke (2009). The 2009 World Average of alpha(s). Eur. Phys. J. **C64**, 689. doi:10.1140/epjc/s10052-009-1173-1 [,111(2009)], arXiv:0908.1135.

[9] E. V. Shuryak (1978). Theory of Hadronic Plasma. Sov. Phys. JETP **47**, 212. [Zh. Eksp. Teor. Fiz.74,408(1978)].

[10] E. V. Shuryak (1980). Quantum Chromodynamics and the Theory of Superdense Matter. Phys. Rept. **61**, 71. doi:10.1016/0370-1573(80)90105-2

[11] N. Cabibbo and G. Parisi (1975). Exponential Hadronic Spectrum and Quark Liberation. Phys. Lett. **59B**, 67. doi:10.1016/0370-2693(75)90158-6

[12] J. C. Collins and M. J. Perry (1975). Superdense Matter: Neutrons Or Asymptotically Free Quarks? Phys. Rev. Lett. **34**, 1353. doi:10.1103/PhysRevLett.34.1353

[13] B. A. Freedman and L. D. McLerran (1977). Fermions and Gauge Vector Mesons at Finite Temperature and Density. 3. The Ground State Energy of a Relativistic Quark Gas. Phys. Rev. **D16**, 1169. doi:10.1103/PhysRevD.16.1169

[14] J. M. Lattimer (2012). The nuclear equation of state and neutron star masses. Ann. Rev. Nucl. Part. Sci. **62**, 485. doi:10.1146/annurev-nucl-102711-095018 arXiv:1305.3510.

[15] M. Gyulassy (2004). The QGP discovered at RHIC. In Structure and dynamics of elementary matter. Proceedings, NATO Advanced Study Institute, Camyuva-Kemer, Turkey, September 22-October 2, 2003, pp. 159–182. arXiv:nucl-th/0403032.

[16] W. Fischer and J. M. Jowett (2014). Ion Colliders. Rev. Accel. Sci. Tech. **7**, 49. doi:10.1142/S1793626814300047

[17] D. A. Teaney (2010). Viscous hydrodynamics and the quark gluon plasma pp. 207–266. doi:10.1142/9789814293297_0004 arXiv:0905.2433.

[18] B. Abelev et al. (ALICE) (2013). Centrality determination of Pb-Pb collisions at $\sqrt{s_{NN}} = 2.76$ TeV with ALICE. Phys. Rev. **C88**(4), 044909. doi:10.1103/PhysRevC.88.044909 arXiv:1301.4361.

[19] M. L. Miller, K. Reygers, S. J. Sanders, and P. Steinberg (2007). Glauber modeling in high energy nuclear collisions. Ann. Rev. Nucl. Part. Sci. **57**, 205. doi:10.1146/annurev.nucl.57.090506.123020 arXiv:nucl-ex/0701025.

[20] L. D. McLerran and R. Venugopalan (1994). Gluon distribution functions for very large nuclei at small transverse momentum. Phys. Rev. **D49**, 3352. doi:10.1103/PhysRevD.49.3352 arXiv:hep-ph/9311205.

[21] L. D. McLerran and R. Venugopalan (1994). Computing quark and gluon distribution functions for very large nuclei. Phys. Rev. **D49**, 2233. doi:10.1103/PhysRevD.49.2233 arXiv:hep-ph/9309289.

[22] L. D. McLerran and R. Venugopalan (1994). Green's functions in the color field of a large nucleus. Phys. Rev. **D50**, 2225. doi:10.1103/PhysRevD.50.2225 arXiv:hep-ph/9402335.

[23] B. Schenke, P. Tribedy, and R. Venugopalan (2012). Fluctuating Glasma initial conditions and flow in heavy ion collisions. Phys. Rev. Lett. **108**, 252301. doi:10.1103/PhysRevLett.108.252301 arXiv:1202.6646.

[24] K. H. Ackermann et al. (STAR) (2001). Elliptic flow in Au + Au collisions at (S(NN))**(1/2) = 130 GeV. Phys. Rev. Lett. **86**, 402. doi:10.1103/PhysRevLett.86.402 arXiv:nucl-ex/0009011.

[25] D. Teaney (2003). The Effects of viscosity on spectra, elliptic flow, and HBT radii. Phys. Rev. **C68**, 034913. doi:10.1103/PhysRevC.68.034913 arXiv:nucl-th/0301099.

[26] H.-J. Drescher, A. Dumitru, C. Gombeaud, and J.-Y. Ollitrault (2007). The Centrality dependence of elliptic flow, the hydrodynamic limit, and the viscosity of hot QCD. Phys. Rev. **C76**, 024905. doi:10.1103/PhysRevC.76.024905 arXiv:0704.3553.

[27] P. Romatschke and U. Romatschke (2007). Viscosity Information from Relativistic Nuclear Collisions: How Perfect is the Fluid Observed at RHIC? Phys. Rev. Lett. **99**, 172301. doi:10.1103/PhysRevLett.99.172301 arXiv:0706.1522.

[28] W. A. Hiscock and L. Lindblom (1985). Generic instabilities in first-order dissipative relativistic fluid theories. Phys. Rev. **D31**, 725. doi:10.1103/PhysRevD.31.725

[29] W. Israel (1976). Nonstationary irreversible thermodynamics: A Causal relativistic theory. Annals Phys. **100**, 310. doi:10.1016/0003-4916(76)90064-6

[30] W. Israel and J. M. Stewart (1979). Transient relativistic thermodynamics and kinetic theory. Annals Phys. **118**, 341. doi:10.1016/0003-4916(79)90130-1

[31] A. Bazavov et al. (HotQCD) (2014). Equation of state in (2+1)-flavor QCD. Phys. Rev. **D90**, 094503. doi:10.1103/PhysRevD.90.094503 arXiv:1407.6387.

[32] F. Cooper and G. Frye (1974). Comment on the Single Particle Distribution in the Hydrodynamic and Statistical Thermodynamic Models of Multiparticle Production. Phys. Rev. **D10**, 186. doi:10.1103/PhysRevD.10.186

[33] J. D. Bjorken (1982). Energy Loss of Energetic Partons in Quark - Gluon Plasma: Possible Extinction of High p(t) Jets in Hadron - Hadron Collisions .

[34] M. Gyulassy, I. Vitev, and X. N. Wang (2001). High p(T) azimuthal asymmetry in non-central A+A at RHIC. Phys. Rev. Lett. **86**, 2537. doi:10.1103/PhysRevLett.86.2537 arXiv:nucl-th/0012092.

[35] A. Angerami (2012). Jet Quenching in Relativistic Heavy Ion Collisions at the LHC. Ph.D. thesis, Columbia U. arXiv:1208.5043.

[36] B. Betz and M. Gyulassy (2014). Constraints on the Path-Length Dependence of Jet Quenching in Nuclear Collisions at RHIC and LHC. JHEP **08**, 090. doi:10.1007/JHEP10(2014)043, 10.1007/JHEP08(2014)090 [Erratum: JHEP10,043(2014)], arXiv:1404.6378.

[37] J. Xu, J. Liao, and M. Gyulassy (2015). Consistency of Perfect Fluidity and Jet Quenching in semi-Quark-Gluon Monopole Plasmas. Chin. Phys. Lett. **32**(9), 092501. doi:10.1088/0256-307X/32/9/092501 arXiv:1411.3673.

[38] J. Noronha-Hostler, B. Betz, J. Noronha, and M. Gyulassy (2016). Event-by-event hydrodynamics + jet energy loss: A solution to the $R_{AA} \otimes v_2$ puzzle. Phys. Rev. Lett. **116**(25), 252301. doi:10.1103/PhysRevLett.116.252301 arXiv:1602.03788.

[39] J. Xu, J. Liao, and M. Gyulassy (2016). Bridging Soft-Hard Transport Properties of Quark-Gluon Plasmas with CUJET3.0. JHEP **02**, 169. doi:10.1007/JHEP02(2016)169 arXiv:1508.00552.

[40] R. Baier, Y. L. Dokshitzer, A. H. Mueller, S. Peigne, and D. Schiff (1997). Radiative energy loss of high-energy quarks and gluons in a finite volume quark - gluon plasma. Nucl. Phys. **B483**, 291. doi:10.1016/S0550-3213(96)00553-6 arXiv:hep-ph/9607355.

[41] R. Baier, Y. L. Dokshitzer, A. H. Mueller, S. Peigne, and D. Schiff (1997). Radiative energy loss and p(T) broadening of high-energy partons in nuclei. Nucl. Phys. **B484**, 265. doi:10.1016/S0550-3213(96)00581-0 arXiv:hep-ph/9608322.

[42] R. Baier, Y. L. Dokshitzer, A. H. Mueller, and D. Schiff (1998). Medium induced radiative energy loss: Equivalence between the BDMPS and Zakharov formalisms. Nucl. Phys. **B531**, 403. doi:10.1016/S0550-3213(98)00546-X arXiv:hep-ph/9804212.

[43] R. Baier, Y. L. Dokshitzer, A. H. Mueller, and D. Schiff (1998). Radiative energy loss of high-energy partons traversing an expanding QCD plasma. Phys. Rev. **C58**, 1706. doi:10.1103/PhysRevC.58.1706 arXiv:hep-ph/9803473.

[44] R. Baier, Y. L. Dokshitzer, A. H. Mueller, and D. Schiff (1999). Angular dependence of the radiative gluon spectrum and the energy loss of hard jets in QCD media. Phys. Rev. **C60**, 064902. doi:10.1103/PhysRevC.60.064902 arXiv:hep-ph/9907267.

[45] M. Gyulassy, P. Levai, and I. Vitev (1999). Jet quenching in thin plasmas. Nucl. Phys. **A661**, 637. doi:10.1016/S0375-9474(99)85106-9 arXiv:hep-ph/9907343.

[46] M. Gyulassy, P. Levai, and I. Vitev (2000). Jet quenching in thin quark gluon plasmas. 1. Formalism. Nucl. Phys. **B571**, 197. doi:10.1016/S0550-3213(99)00713-0 arXiv:hep-ph/9907461.

[47] M. Gyulassy, P. Levai, and I. Vitev (2001). Reaction operator approach to nonAbelian energy loss. Nucl. Phys. **B594**, 371. doi:10.1016/S0550-3213(00)00652-0 arXiv:nucl-th/0006010.

[48] M. Gyulassy, P. Levai, and I. Vitev (2000). NonAbelian energy loss at finite opacity. Phys. Rev. Lett. **85**, 5535. doi:10.1103/PhysRevLett.85.5535 arXiv:nucl-th/0005032.

[49] P. B. Arnold, G. D. Moore, and L. G. Yaffe (2001). Photon emission from ultrarelativistic plasmas. JHEP **11**, 057. doi:10.1088/1126-6708/2001/11/057 arXiv:hep-ph/0109064.

[50] P. B. Arnold, G. D. Moore, and L. G. Yaffe (2002). Photon and gluon emission in relativistic plasmas. JHEP **06**, 030. doi:10.1088/1126-6708/2002/06/030 arXiv:hep-ph/0204343.

[51] J. Liao and E. Shuryak (2009). Angular Dependence of Jet Quenching Indicates Its Strong Enhancement Near the QCD Phase Transition. Phys. Rev. Lett. **102**, 202302. doi:10.1103/PhysRevLett.102.202302 arXiv:0810.4116.

[52] E. V. Shuryak (2002). The Azimuthal asymmetry at large p(t) seem to be too large for a 'jet quenching'. Phys. Rev. **C66**, 027902. doi:10.1103/PhysRevC.66.027902 arXiv:nucl-th/0112042.

[53] Ya. M. Shnir (2005). Magnetic monopoles. URL http://www.springer.com/book/3-540-25277-0.

[54] P. A. M. Dirac (1931). Quantized Singularities in the Electromagnetic Field. Proc. Roy. Soc. Lond. **A133**, 60. doi:10.1098/rspa.1931.0130 [,278(1931)].

[55] Y. Aharonov and D. Bohm (1959). Significance of electromagnetic potentials in the quantum theory. Phys. Rev. **115**, 485. doi:10.1103/PhysRev.115.485 [,95(1959)].

[56] G. 't Hooft (1974). Magnetic Monopoles in Unified Gauge Theories. Nucl. Phys. **B79**, 276. doi:10.1016/0550-3213(74)90486-6 [,291(1974)].

[57] A. M. Polyakov (1974). Particle Spectrum in the Quantum Field Theory. JETP Lett. **20**, 194. [,300(1974)].

[58] E. B. Bogomolny (1976). Stability of Classical Solutions. Sov. J. Nucl. Phys. **24**, 449. [Yad. Fiz.24,861(1976)].

[59] M. K. Prasad and C. M. Sommerfield (1975). An Exact Classical Solution for the 't Hooft Monopole and the Julia-Zee Dyon. Phys. Rev. Lett. **35**, 760. doi:10.1103/PhysRevLett.35.760

[60] A. Sinha (1976). SU(3) Magnetic Monopoles. Phys. Rev. **D14**, 2016. doi:10.1103/PhysRevD.14.2016

[61] Y. Nambu (1974). Strings, Monopoles and Gauge Fields. Phys. Rev. **D10**, 4262. doi:10.1103/PhysRevD.10.4262 [,310(1974)].

[62] G. 't Hooft (1981). Topology of the Gauge Condition and New Confinement Phases in Nonabelian Gauge Theories. Nucl. Phys. **B190**, 455. doi:10.1016/0550-3213(81)90442-9

[63] G. Ripka (2004). Dual superconductor models of color confinement. Lect. Notes Phys. **639**, pp.1. doi:10.1007/b94800 arXiv:hep-ph/0310102.

[64] A. D'Alessandro, M. D'Elia, and E. V. Shuryak (2010). Thermal Monopole Condensation and Confinement in finite temperature Yang-Mills Theories. Phys. Rev. **D81**, 094501. doi:10.1103/PhysRevD.81.094501 arXiv:1002.4161.

[65] C. Bonati and M. D'Elia (2013). The Maximal Abelian Gauge in SU(N) gauge theories and thermal monopoles for N = 3. Nucl. Phys. **B877**, 233. doi:10.1016/j.nuclphysb.2013.10.004 arXiv:1308.0302.

[66] Y. Hidaka and R. D. Pisarski (2008). Suppression of the shear viscosity in a "semi"-quark-gluon plasma. Physical Review D **78**(7), 071501.

[67] J. Liao and E. Shuryak (2007). Strongly coupled plasma with electric and magnetic charges. Phys. Rev. **C75**, 054907. doi:10.1103/PhysRevC.75.054907 arXiv:hep-ph/0611131.

[68] J. Liao and E. Shuryak (2008). Electric Flux Tube in Magnetic Plasma. Phys. Rev. **C77**, 064905. doi:10.1103/PhysRevC.77.064905 arXiv:0706.4465.

[69] J. Liao and E. Shuryak (2008). Magnetic Component of Quark-Gluon Plasma is also a Liquid! Phys. Rev. Lett. **101**, 162302. doi:10.1103/PhysRevLett.101.162302 arXiv:0804.0255.

[70] C. Ratti and E. Shuryak (2009). The Role of monopoles in a Gluon Plasma. Phys. Rev. **D80**, 034004. doi:10.1103/PhysRevD.80.034004 arXiv:0811.4174.

[71] R. P. Feynman (1948). Space-time approach to nonrelativistic quantum mechanics. Rev. Mod. Phys. **20**, 367. doi:10.1103/RevModPhys.20.367

[72] M. Creutz (1979). Confinement and the Critical Dimensionality of Space-Time. Phys. Rev. Lett. **43**, 553. doi:10.1103/PhysRevLett.43.553, 10.1103/PhysRevLett.43.890.2 [Erratum: Phys. Rev. Lett.43,890(1979)].

[73] M. Creutz and B. Freedman (1981). A STATISTICAL APPROACH TO QUANTUM MECHANICS. Annals Phys. **132**, 427. doi:10.1016/0003-4916(81)90074-9

[74] E. V. Shuryak and O. V. Zhirov (1984). TESTING MONTE CARLO METHODS FOR PATH INTEGRALS IN SOME QUANTUM MECHANICAL PROBLEMS. Nucl. Phys. **B242**, 393. doi:10.1016/0550-3213(84)90401-2

[75] N. Metropolis, A. W. Rosenbluth, M. N. Rosenbluth, A. H. Teller, and E. Teller (1953). Equation of state calculations by fast computing machines. J. Chem. Phys. **21**, 1087. doi:10.1063/1.1699114

[76] D. M. Ceperley (1995). Path integrals in the theory of condensed helium. Rev. Mod. Phys. **67**, 279. doi:10.1103/RevModPhys.67.279

[77] M. Graves (2014). Path integral quantum monte carlo study of coupling and proximity effects in superfluid helium-4 .

[78] M. Boninsegni, N. V. Prokof'ev, and B. V. Svistunov (2006). Worm algorithm and diagrammatic monte carlo: A new approach to continuous-space path integral monte carlo simulations. Phys. Rev. E **74**, 036701. doi:10.1103/PhysRevE.74.036701

[79] P. P. Ewald (1921). Die berechnung optischer und elektrostatischer gitterpotentiale. Annalen der Physik **369**(3), 253. ISSN 1521-3889. doi:10.1002/andp.19213690304

[80] A. Y. Toukmaji and J. A. Board Jr (1996). Ewald summation techniques in perspective: a survey. Computer physics communications **95**(2-3), 73.

[81] R. P. Feynman (1953). Atomic Theory of the lamda Transition in Helium. Phys. Rev. **91**, 1291. doi:10.1103/PhysRev.91.1291

[82] R. P. Feynman (1953). Atomic Theory of Liquid Helium Near Absolute Zero. Phys. Rev. **91**, 1301. doi:10.1103/PhysRev.91.1301

[83] S. N. Bose (1924). Plancks gesetz und lichtquantenhypothese. Zeitschrift für Physik. **26**, 178. doi:10.1007/BF01327326

[84] A. Einstein (1924). Quantentheorie des einatomigen idealen Gases, volume 20. Akademie der Wissenshaften, in Kommission bei W. de Gruyter.

[85] A. A. Belavin, A. M. Polyakov, A. S. Schwartz, and Yu. S. Tyupkin (1975). Pseudoparticle Solutions of the Yang-Mills Equations. Phys. Lett. **B59**, 85. doi:10.1016/0370-2693(75)90163-X [,350(1975)].

[86] T. C. Kraan and P. van Baal (1998). Exact T duality between calorons and Taub - NUT spaces. Phys. Lett. **B428**, 268. doi:10.1016/S0370-2693(98)00411-0 arXiv:hep-th/9802049.

[87] T. C. Kraan and P. van Baal (1998). Periodic instantons with nontrivial holonomy. Nucl. Phys. **B533**, 627. doi:10.1016/S0550-3213(98)00590-2 arXiv:hep-th/9805168.

[88] K.-M. Lee and C.-h. Lu (1998). SU(2) calorons and magnetic monopoles. Phys. Rev. **D58**, 025011. doi:10.1103/PhysRevD.58.025011 arXiv:hep-th/9802108.

[89] D. Diakonov (2009). Topology and confinement. Nucl. Phys. Proc. Suppl. **195**, 5. doi:10.1016/j.nuclphysbps.2009.10.010 arXiv:0906.2456.

[90] R. Larsen and E. Shuryak (2015). Interacting ensemble of the instanton-dyons and the deconfinement phase transition in the SU(2) gauge theory. Phys. Rev. **D92**(9), 094022. doi:10.1103/PhysRevD.92.094022 arXiv:1504.03341.

[91] R. Larsen and E. Shuryak (2016). Instanton-dyon Ensemble with two Dynamical Quarks: the Chiral Symmetry Breaking. Phys. Rev. **D93**(5), 054029. doi:10.1103/PhysRevD.93.054029 arXiv:1511.02237.

[92] Y. Liu, E. Shuryak, and I. Zahed (2015). Confining dyon-antidyon Coulomb liquid model. I. Phys. Rev. **D92**(8), 085006. doi:10.1103/PhysRevD.92.085006 arXiv:1503.03058.

[93] Y. Liu, E. Shuryak, and I. Zahed (2015). Light quarks in the screened dyon-antidyon Coulomb liquid model. II. Phys. Rev. **D92**(8), 085007. doi:10.1103/PhysRevD.92.085007 arXiv:1503.09148.

[94] E. Shuryak (2018). Instanton-dyon ensembles reproduce deconfinement and chiral restoration phase transitions. EPJ Web Conf. **175**, 12001. doi:10.1051/epjconf/201817512001 arXiv:1710.03611.

[95] N. Dorey and A. Parnachev (2001). Instantons, compactification and S duality in N=4 SUSY Yang-Mills theory. 2. JHEP **08**, 059. doi:10.1088/1126-6708/2001/08/059 arXiv:hep-th/0011202.

[96] E. Poppitz and M. Unsal (2011). Seiberg-Witten and 'Polyakov-like' magnetic bion confinements are continuously connected. JHEP **07**, 082. doi:10.1007/JHEP07(2011)082 arXiv:1105.3969.

[97] E. Poppitz, T. Schfer, and M. Unsal (2012). Continuity, Deconfinement, and (Super) Yang-Mills Theory. JHEP **10**, 115. doi:10.1007/JHEP10(2012)115 arXiv:1205.0290.

[98] N. Dorey (2001). Instantons, compactification and S-duality in N=4 SUSY Yang-Mills theory. 1. JHEP **04**, 008. doi:10.1088/1126-6708/2001/04/008 arXiv:hep-th/0010115.

[99] E. Alvarez, L. Alvarez-Gaume, and Y. Lozano (1995). An Introduction to T duality in string theory. Nucl. Phys. Proc. Suppl. **41**, 1. doi:10.1016/0920-5632(95)00429-D arXiv:hep-th/9410237.

[100] A. Zygmund and R. Fefferman (2003). Trigonometric Series. Cambridge Mathematical Library. Cambridge University Press, 3 edition. doi:10.1017/CBO9781316036587

[101] B. Julia and A. Zee (1975). Poles with Both Magnetic and Electric Charges in Non-abelian Gauge Theory. Phys. Rev. **D11**, 2227. doi:10.1103/PhysRevD.11.2227

[102] D. Diakonov, N. Gromov, V. Petrov, and S. Slizovskiy (2004). Quantum weights of dyons and of instantons with nontrivial holonomy. Phys. Rev. **D70**, 036003. doi:10.1103/PhysRevD.70.036003 arXiv:hep-th/0404042.

[103] D. Diakonov, C. Gattringer, and H.-P. Schadler (2012). Free energy for parameterized Polyakov loops in SU(2) and SU(3) lattice gauge theory. JHEP **08**, 128. doi:10.1007/JHEP08(2012)128 arXiv:1205.4768.

[104] D. Diakonov, V. Petrov, H.-P. Schadler, and C. Gattringer (2013). Effective Lagrangian for the Polyakov line on a lattice. JHEP **11**, 207. doi:10.1007/JHEP11(2013)207 arXiv:1308.2328.

[105] M. Ogilvie and P. Meisinger (2014). Exploring confinement in SU(N) gauge theories with double-trace Polyakov loop deformations. PoS **LATTICE2014**, 339. arXiv:1411.5344.

[106] E. L. Pollock and D. M. Ceperley (1987). Path-integral computation of superfluid densities. Phys. Rev. **B36**, 8343. doi:10.1103/PhysRevB.36.8343

[107] E. L. Pollock and K. J. Runge (1992). Finite-size-scaling analysis of a simulation of thehe4superfluid transition. Physical Review B **46**(6), 3535. ISSN 1095-3795. doi:10.1103/physrevb.46.3535 URL `http://dx.doi.org/10.1103/PhysRevB.46.3535`.

[108] M. Cristoforetti and E. Shuryak (2009). Bose-Einstein Condensation of strongly interacting bosons: From liquid He-4 to QCD monopoles. Phys. Rev. **D80**, 054013. doi:10.1103/PhysRevD.80.054013 arXiv:0906.2019.

[109] C. Gattringer and C. Lang (2009). Quantum chromodynamics on the lattice: an introductory presentation, volume 788. Springer Science & Business Media.

[110] R. A. Aziz, V. P. S. Nain, J. S. Carley, W. L. Taylor, and G. T. McConville (1979). An accurate intermolecular potential for helium. The Journal of Chemical Physics **70**(9), 4330. ISSN 1089-7690. doi:10.1063/1.438007 URL http://dx.doi.org/10.1063/1.438007.

[111] P. Gruter, D. Ceperley, and F. Laloe (1997). Critical Temperature of Bose-Einstein Condensation of Hard-Sphere Gases. Phys. Rev. Lett. **79**, 3549. doi:10.1103/PhysRevLett.79.3549

[112] M. Holzmann, G. Baym, J.-P. Blaizot, and F. Laloe (2001). Nonanalytic Dependence of the Transition Temperature of the Homogeneous Dilute Bose Gas on Scattering Length. Phys. Rev. Lett. **87**, 120403. doi:10.1103/PhysRevLett.87.120403

[113] R. Berwick (2003). An idiot's guide to support vector machines (svms). Retrieved on October **21**, 2011.

[114] J. Liao and E. Shuryak (2008). Magnetic Component of Quark-Gluon Plasma is also a Liquid! Phys. Rev. Lett. **101**, 162302. doi:10.1103/PhysRevLett.101.162302 arXiv:0804.0255.

[115] A. D'Alessandro and M. D'Elia (2008). Magnetic monopoles in the high temperature phase of Yang-Mills theories. Nucl. Phys. **B799**, 241. doi:10.1016/j.nuclphysb.2008.03.002 arXiv:0711.1266.

[116] R. Jackiw and C. Rebbi (1976). Solitons with Fermion Number 1/2. Phys. Rev. **D13**, 3398. doi:10.1103/PhysRevD.13.3398

[117] J. Liao and E. Shuryak (2012). Effect of Light Fermions on the Confinement Transition in QCD-like Theories. Phys. Rev. Lett. **109**, 152001. doi:10.1103/PhysRevLett.109.152001 arXiv:1206.3989.

[118] S. Borsanyi, Z. Fodor, C. Hoelbling, S. D. Katz, S. Krieg, C. Ratti, and K. K. Szabo (Wuppertal-Budapest) (2010). Is there still any T_c mystery in lattice QCD? Results with physical masses in the continuum limit III. JHEP **09**, 073. doi:10.1007/JHEP09(2010)073 arXiv:1005.3508.

[119] P. Petreczky and H. P. Schadler (2015). Renormalization of the Polyakov loop with gradient flow. Phys. Rev. **D92**(9), 094517. doi:10.1103/PhysRevD.92.094517 arXiv:1509.07874.

[120] P. N. Meisinger and M. C. Ogilvie (1996). Chiral symmetry restoration and Z(N) symmetry. Phys. Lett. **B379**, 163. doi:10.1016/0370-2693(96)00447-9 arXiv:hep-lat/9512011.

[121] K. Fukushima (2004). Chiral effective model with the Polyakov loop. Phys. Lett. **B591**, 277. doi:10.1016/j.physletb.2004.04.027 arXiv:hep-ph/0310121.

[122] A. Bazavov et al. (2013). Strangeness at high temperatures: from hadrons to quarks. Phys. Rev. Lett. **111**, 082301. doi:10.1103/PhysRevLett.111.082301 arXiv:1304.7220.

[123] E. V. Shuryak and I. Zahed (2004). Towards a theory of binary bound states in the quark gluon plasma. Phys. Rev. **D70**, 054507. doi:10.1103/PhysRevD.70.054507 arXiv:hep-ph/0403127.

[124] J. Engels, F. Karsch, and K. Redlich (1995). Scaling properties of the energy density in SU(2) lattice gauge theory. Nucl. Phys. **B435**, 295. doi:10.1016/0550-3213(94)00491-V arXiv:hep-lat/9408009.

[125] J. Engels, J. Fingberg, F. Karsch, D. Miller, and M. Weber (1990). Nonperturbative thermodynamics of SU(N) gauge theories. Phys. Lett. **B252**, 625. doi:10.1016/0370-2693(90)90496-S

[126] S. Borsanyi, G. Endrodi, Z. Fodor, S. D. Katz, and K. K. Szabo (2012). Precision SU(3) lattice thermodynamics for a large temperature range. JHEP **07**, 056. doi:10.1007/JHEP07(2012)056 arXiv:1204.6184.

[127] M. Gyulassy and X.-n. Wang (1994). Multiple collisions and induced gluon Bremsstrahlung in QCD. Nucl. Phys. **B420**, 583. doi:10.1016/0550-3213(94)90079-5 arXiv:nucl-th/9306003.

[128] S. Borsanyi, Z. Fodor, S. D. Katz, A. Psztor, K. K. Szab, and C. Trk (2015). Static $\overline{\mathrm{Q}}\mathrm{Q}$ pair free energy and screening masses from correlators of Polyakov loops: continuum extrapolated lattice results at the QCD physical point. JHEP **04**, 138. doi:10.1007/JHEP04(2015)138 arXiv:1501.02173.

[129] J. Liao and E. Shuryak (2010). Static $\bar{Q}Q$ Potentials and the Magnetic Component of QCD Plasma near T_c. Phys. Rev. **D82**, 094007. doi:10.1103/PhysRevD.82.094007 arXiv:0804.4890.

[130] H. Niemi, K. J. Eskola, and R. Paatelainen (2016). Event-by-event fluctuations in a perturbative QCD + saturation + hydrodynamics model: Determining QCD matter shear viscosity in ultrarelativistic heavy-ion collisions. Phys. Rev. **C93**(2), 024907. doi:10.1103/PhysRevC.93.024907 arXiv:1505.02677.

[131] S. Ryu, J. F. Paquet, C. Shen, G. S. Denicol, B. Schenke, S. Jeon, and C. Gale (2015). Importance of the Bulk Viscosity of QCD in Ultrarelativistic Heavy-Ion Collisions. Phys. Rev. Lett. **115**(13), 132301. doi:10.1103/PhysRevLett.115.132301 arXiv:1502.01675.

[132] S. Ryu, J.-F. Paquet, C. Shen, G. Denicol, B. Schenke, S. Jeon, and C. Gale (2018). Effects of bulk viscosity and hadronic rescattering in heavy ion collisions at energies available at the BNL Relativistic Heavy Ion Collider and at the CERN Large Hadron Collider. Phys. Rev. **C97**(3), 034910. doi:10.1103/PhysRevC.97.034910 arXiv:1704.04216.

[133] J.-F. Paquet. private communication.

[134] B. I. Abelev et al. (STAR) (2009). Systematic Measurements of Identified Particle Spectra in pp, d^+ Au and Au+Au Collisions from STAR. Phys. Rev. **C79**, 034909. doi:10.1103/PhysRevC.79.034909 arXiv:0808.2041.

[135] M. Spousta and B. Cole (2016). Interpreting single jet measurements in Pb + Pb collisions at the LHC. Eur. Phys. J. **C76**(2), 50. doi:10.1140/epjc/s10052-016-3896-0 arXiv:1504.05169.

[136] I. Vitev (2006). Testing the mechanism of QGP-induced energy loss. Phys. Lett. **B639**, 38. doi:10.1016/j.physletb.2006.05.083 arXiv:hep-ph/0603010.

[137] B. A. Kniehl, G. Kramer, and B. Potter (2000). Fragmentation functions for pions, kaons, and protons at next-to-leading order. Nucl. Phys. **B582**, 514. doi:10.1016/S0550-3213(00)00303-5 arXiv:hep-ph/0010289.

[138] B. Abelev et al. (ALICE) (2013). Centrality Dependence of Charged Particle Production at Large Transverse Momentum in Pb–Pb Collisions at $\sqrt{s_{\rm NN}} = 2.76$ TeV. Phys. Lett. **B720**, 52. doi:10.1016/j.physletb.2013.01.051 arXiv:1208.2711.

[139] S. Chatrchyan et al. (CMS) (2012). Study of high-pT charged particle suppression in PbPb compared to *pp* collisions at $\sqrt{s_{NN}} = 2.76$ TeV. Eur. Phys. J. **C72**, 1945. doi:10.1140/epjc/s10052-012-1945-x arXiv:1202.2554.

[140] A. Adare et al. (PHENIX) (2008). Suppression pattern of neutral pions at high transverse momentum in Au + Au collisions at s(NN)**(1/2) = 200-GeV and constraints on medium transport coefficients. Phys. Rev. Lett. **101**, 232301. doi:10.1103/PhysRevLett.101.232301 arXiv:0801.4020.

[141] A. Adare et al. (PHENIX) (2013). Neutral pion production with respect to centrality and reaction plane in Au+Au collisions at $\sqrt{s_{NN}}$=200 GeV. Phys. Rev. **C87**(3), 034911. doi:10.1103/PhysRevC.87.034911 arXiv:1208.2254.

[142] B. Abelev et al. (ALICE) (2013). Anisotropic flow of charged hadrons, pions and (anti-)protons measured at high transverse momentum in Pb-Pb collisions at $\sqrt{s_{NN}}$=2.76 TeV. Phys. Lett. **B719**, 18. doi:10.1016/j.physletb.2012.12.066 arXiv:1205.5761.

[143] S. Chatrchyan et al. (CMS) (2012). Azimuthal anisotropy of charged particles at high transverse momenta in PbPb collisions at $\sqrt{s_{NN}} = 2.76$ TeV. Phys. Rev. Lett. **109**, 022301. doi:10.1103/PhysRevLett.109.022301 arXiv:1204.1850.

[144] A. Adare et al. (PHENIX) (2010). Azimuthal anisotropy of neutral pion production in Au+Au collisions at $\sqrt{(s_N N)} = 200$ GeV: Path-length dependence of jet quenching and the role of initial geometry. Phys. Rev. Lett. **105**, 142301. doi:10.1103/PhysRevLett.105.142301 arXiv:1006.3740.

[145] G. Aad et al. (ATLAS) (2010). Observation of a Centrality-Dependent Dijet Asymmetry in Lead-Lead Collisions at $\sqrt{s_{NN}} = 2.77$ TeV with the ATLAS Detector at the LHC. Phys. Rev. Lett. **105**, 252303. doi:10.1103/PhysRevLett.105.252303 arXiv:1011.6182.

[146] T. Suzuki and I. Yotsuyanagi (1990). A possible evidence for Abelian dominance in quark confinement. Phys. Rev. **D42**, 4257. doi:10.1103/PhysRevD.42.4257

[147] O. Miyamura (1995). Chiral symmetry breaking in gauge fields dominated by monopoles on SU(2) lattices. Phys. Lett. **B353**, 91. doi:10.1016/0370-2693(95)00530-X

[148] T. Schäfer and E. V. Shuryak (1998). Instantons in QCD. Rev. Mod. Phys. **70**, 323. doi:10.1103/RevModPhys.70.323 arXiv:hep-ph/9610451.

[149] T. Banks and A. Casher (1980). Chiral Symmetry Breaking in Confining Theories. Nucl. Phys. **B169**, 103. doi:10.1016/0550-3213(80)90255-2

[150] C. J. Callias (1977). Spectra of Fermions in Monopole Fields: Exactly Soluble Models. Phys. Rev. **D16**, 3068. doi:10.1103/PhysRevD.16.3068